Genome concentration limits cell growth and modulates proteome composition in *Escherichia coli*

Jarno Mäkelä[1,2,3,†], Alexandros Papagiannakis[1,2,†], Wei-Hsiang Lin[1,2,&], Michael C. Lanz[4,5,&], Skye Glenn[2,4], Matthew Swaffer[4,¶], Georgi K. Marinov[6], Jan M. Skotheim[4,5], Christine Jacobs-Wagner[1,2,4,7*]

[1]Howard Hughes Medical Institute, Stanford University, Stanford, CA 94305, USA

[2]Sarafan Chemistry, Engineering, and Medicine for Human Health Institute, Stanford University, Stanford, CA 94305, USA

[3]Institute of Biotechnology, Helsinki Institute of Life Science, University of Helsinki, Helsinki, Finland

[4]Department of Biology, Stanford University, Stanford, CA 94305, USA

[5]Chan Zuckerberg Biohub, Stanford, CA 94305, USA

[6]Department of Genetics, Stanford University, Stanford, CA 94305, USA

[7]Department of Microbiology and Immunology, Stanford School of Medicine, Stanford, CA 94305, USA

[¶]Current address: Wellcome Centre for Cell Biology, University of Edinburgh, Edinburgh, EH9 3BF, UK

[†]These authors contributed equally to this work.

[&]These authors contributed equally to this work.

[*]For correspondence: jacobs-wagner@stanford.edu

KEYWORDS: DNA limitation, ribosome, RNA polymerase, proteome, cell growth, cell size, single-molecule tracking, single-cell dynamics, tandem-mass-tag mass spectrometry.

ABSTRACT

Defining the cellular factors that drive growth rate and proteome composition is essential for understanding and manipulating cellular systems. In bacteria, ribosome concentration is known to be a constraining factor of cell growth rate, while gene concentration is usually assumed not to be limiting. Here, using single-molecule tracking, quantitative single-cell microscopy, and modeling, we show that genome dilution in *Escherichia coli* cells arrested for DNA replication limits total RNA polymerase activity within physiological cell sizes across tested nutrient conditions. This rapid-onset limitation on bulk transcription results in sub-linear scaling of total active ribosomes with cell size and sub-exponential growth. Such downstream effects on bulk translation and cell growth are near-immediately detectable in a nutrient-rich medium, but delayed in nutrient-poor conditions, presumably due to cellular buffering activities. RNA sequencing and tandem-mass-tag mass spectrometry experiments further reveal that genome dilution remodels the relative abundance of mRNAs and proteins with cell size at a global level. Altogether, our findings indicate that chromosome concentration is a limiting factor of transcription and a global modulator of the transcriptome and proteome composition in *E. coli*. Experiments in *Caulobacter crescentus* and comparison with eukaryotic cell studies identify broadly conserved DNA concentration-dependent scaling principles of gene expression.

INTRODUCTION

Cells regulate the intracellular concentration of various proteins and macromolecules to modulate the rate of essential cellular processes, including growth. In bacteria, cell mass and volume typically double between division cycles. Proportionality between biosynthetic capacity and biomass

43 accumulation results in exponential or near-exponential cell growth during the cell cycle (Campos et
44 al., 2014; Schaechter et al., 1958; Siegal-Gaskins and Crosson, 2008; Taheri-Araghi et al., 2015; Wang
45 et al., 2010). What drives exponential growth has been a longstanding question in the microbiology
46 field (Belliveau et al., 2021; Churchward et al., 1982; Ecker and Schaechter, 1963; Zhurinsky et al.,
47 2010). Quantitative studies on model bacteria such as *Escherichia coli* place the concentration of
48 ribosomes and their kinetics as the principal rate-limiting factors (Belliveau et al., 2021; Bosdriesz et
49 al., 2015; Koch, 1988; Scott et al., 2014, 2010). Most other cellular components essential for growth
50 are estimated to be at least an order of magnitude above the level required for proper enzymatic
51 reactions (Belliveau et al., 2021), indicating that they are well in excess in terms of metabolic
52 concentrations. Thus, translation is generally seen as the rate-governing process for cellular growth.
53 While the translocation rate of ribosomes poses an inherent limit on the growth rate of the cell,
54 protein concentrations are predominantly set transcriptionally at the promoter level, with tight
55 coordination between transcription and translation (Balakrishnan et al., 2022).

56 Whereas the importance of ribosome concentration in growth rate determination has been
57 extensively studied, a potential role for genome concentration has received less attention. An early
58 population study on an *E. coli* thymine auxotroph proposed that global transcription is not limited by
59 the concentration of the genome but is instead constrained by the availability of RNA polymerases
60 (RNAPs) (Churchward et al., 1982). However, the potential impact of DNA concentration on
61 determining the growth rate of *E. coli* or other bacteria has, to our knowledge, not been formally
62 tested. Interestingly, *E. coli* and *Bacillus subtilis* have been shown to display small but reproducible
63 deviations from exponential growth during the division cycle (Kar et al., 2021; Nordholt et al., 2020),
64 with the growth rate increasing after the initiation of DNA replication under some conditions.

65 Furthermore, at the population level, these organisms initiate DNA replication at a fixed cell volume
66 (mass) per chromosomal origin of replication (*oriC*) across a wide range of nutrient and genetic
67 conditions (Donachie, 1968; Govers et al., 2024; Si et al., 2017; Zheng et al., 2016), suggesting that
68 DNA concentration is an important physiological parameter for these bacteria. In eukaryotes where
69 genome concentration is also tightly controlled (Ginzberg et al., 2015; Turner et al., 2012), a change
70 in DNA-to-cell-volume ratio has recently been demonstrated to remodel the proteome and promote
71 cellular senescence (Crozier et al., 2023; Foy et al., 2023; Lanz et al., 2023, 2022; Manohar et al., 2023;
72 Neurohr et al., 2019; Wilson et al., 2023).

73 In this study, we combined single-cell and single-molecule microscopy experiments with
74 tandem-mass-tag (TMT) mass spectrometry, RNA sequencing (RNA-seq), and modeling to investigate
75 the potential physiological role of genome concentration in cell growth and proteome composition in
76 *E. coli*.

77

78 **RESULTS**

79 **Growth rate correlates with the genome copy number.**

80 To examine the potential effect of DNA content on the growth rate of *E. coli*, we used two CRISPR
81 interference (CRISPRi) strains with arabinose-inducible control of expression of dCas9 (Li et al., 2016;
82 Si et al., 2017). One strain expressed a single guide RNA (sgRNA) against *oriC* where sequestration by
83 dCas9 binding prevents the initiation of DNA replication to produce cells with a single copy of the
84 chromosome (Si et al., 2017). These cells, referred to as "1N cells" below, grew into filaments as a
85 block in DNA replication prevents cell division, but not cell growth, from occurring (Figure 1A) (Carl,
86 1970; Si et al., 2017; Withers and Bernander, 1998). The second CRISPRi strain, which served as a

87 comparison, expressed a sgRNA against the cell division protein FtsZ. FtsZ depletion blocks cell division
88 while allowing DNA replication to proceed (Addinall et al., 1996; Li et al., 2016). Ongoing growth
89 resulted in filamenting cells with multiple replicating chromosomes, hereafter referred to as "multi-
90 N cells" (Figure 1A). For both strains, we used time-lapse microscopy to monitor growth at the single-
91 cell level at 37°C in M9 minimal medium supplemented with glycerol, casamino acids, and thiamine
92 (M9glyCAAT). Cell area (A) was automatically detected from phase-contrast images using a deep
93 convolutional network (Wiktor et al., 2021), and the absolute growth rate ($\frac{dA}{dt}$) was determined by
94 calculating the difference in cell area between frames. The relative growth rate ($\frac{1}{A}\frac{dA}{dt}$), which is
95 constant for exponential growth, was calculated by dividing the absolute growth rate by the cell area.
96 We used WT cells to verify that the transition from liquid cultures to agarose pads led to stable growth
97 from the start of image acquisition (Figure 1 – figure supplement 1).

98 As the induced CRISPRi *oriC* phenotype is not fully penetrant, we limited our analysis to 1N
99 cells that contained a single DNA object (nucleoid) labeled by a mCherry fusion to the nucleoid-binding
100 protein HupA (referred to as HU below). To confirm this 1N chromosome designation, we used a
101 CRISPRi *oriC* strain that expresses HU-CFP and carries an *oriC*-proximal *parS* site labeled with ParB-
102 mCherry (Figure 1 – figure supplement 2), used here to determine the number of nucleoids and
103 chromosomal origins per cell. We found that 96 ± 1% (mean ± standard deviation, SD, three biological
104 replicates) of cells (n = 3378) with a single HU-labeled nucleoid contained no more than one ParB-
105 mCherry focus, indicative of a single *oriC*.

106 Using this methodology, we observed a significant difference in growth rate between 1N and
107 multi-N cells as shown in representative single-cell growth trajectories (Figure 1B) and in aggregated
108 absolute growth rate measurements (Figure 1C). In multi-N cells, the absolute growth rate rapidly

109 increased with cell area. In 1N cells, the absolute growth rate only moderately increased with cell area,
110 approaching an apparent plateau at large cell sizes (Figure 1C). As an independent validation, we used
111 an orthogonal system to block DNA replication using the temperature-sensitive mutant *dnaC2*, which
112 encodes a deficient DNA helicase loader at the restrictive temperature of 37°C (Carl, 1970; Withers
113 and Bernander, 1998). We observed that the relationship between absolute growth rate and cell area
114 in *dnaC2* cells with a single nucleoid was similar to that of 1N cells produced by the CRISPRi *oriC* system
115 (Figure 1D). This sub-exponential growth in 1N and *dnaC2* cells resulted in a relative growth rate that
116 decreased with cell area (Figure 1E). For multi-N cells, the relative growth rate was not perfectly
117 constant but appeared to increase somewhat with cell area (Figure 1E). It is unclear whether this slight
118 increase is biologically meaningful, as simulations show that a small inaccuracy in cell size from cell
119 segmentation can produce the appearance of super-exponential growth at large cell sizes (Figure 1 –
120 figure supplement 3). Regardless, and most importantly, the multi-N cells grew identically to WT
121 within the same cell size range while 1N cells grew significantly slower (Figure 1 – figure supplement
122 4).

123 The striking divergence in growth between 1N and multi-N cells of the same size suggested
124 that DNA concentration can affect growth rate. The difference in growth rate between 1N and multi-
125 N cells was already apparent in the physiological range of cell sizes when compared to WT cells (Figure
126 1 – figure supplement 4), suggesting that growth rate reduction occurs soon after DNA replication
127 fails to initiate. We confirmed that the slower growth of 1N cells did not depend on the time that cells
128 spent on agarose pads (Figure 1 – figure supplement 5A). We also ruled out that the growth reduction
129 was due to an induction of the SOS response or to an increased level in the nucleotide alarmone

130 (p)ppGpp, as inactivation of either stress pathway (through deletion of *recA* or *spoT*/*relA*, respectively)
131 in 1N cells made little to no difference to their growth rate (Figure 1 – figure supplement 5B).

132 We noticed that, even at the restrictive temperature, the *dnaC2* strain produced a sizeable
133 fraction of cells with more than one HU-mCherry-labelled nucleoid (Figure 1 – figure supplement 6A-
134 B), indicating that the temperate-sensitive effect on DNA replication is not fully penetrant. We took
135 advantage of this phenotypic "leakiness" to measure the growth rate of cells with different numbers
136 of nucleoids (and thus chromosomes) within the *dnaC2* population. We observed a notable difference
137 in growth rate between cells of 1, 2, and >2 nucleoids in the population, with each additional nucleoid
138 contributing to higher cellular growth at a given cell size (Figure 1F-G). This finding is consistent with
139 DNA-limited growth in which cellular growth rate increases with genome concentration. We obtained
140 similar results when we calculated absolute and relative growth rates based on extracted cell volumes
141 instead of areas (Figure 1 – figure supplement 7A-F), as cell width remained largely constant during
142 cell filamentation (Figure 1 – figure supplement 7G).

143 A growth rate dependency on genome concentration is unlikely to be a particularity of *E. coli*,
144 as we also observed a divergence in absolute and relative growth rates with increasing cell area
145 between 1N and multi-N cells of *Caulobacter crescentus* (Figure 1 – figure supplement 8A-B). We
146 generated filamenting 1N and multi-N *C. crescentus* cells by depleting the DNA replication initiation
147 factor DnaA (Gorbatyuk and Marczynski, 2001) and the cell division protein FtsZ (Wang et al., 2001),
148 respectively. We confirmed the 1N versus multi-N designation by visualizing the number of
149 chromosomal origins of replication (one versus multiple) per cell using the *parS*/ParB-eCFP labeling
150 system (Figure 1 – figure supplement 8C).

151

152 **The concentration of ribosomal proteins remains relatively constant in genome-diluted *E. coli* cells.**
153 Ribosome content is often proposed to explain the exponential growth of biomass in bacteria, with
154 growth rate being directly proportional to ribosome concentration (Bremer and Dennis, 1996; Ecker
155 and Schaechter, 1963; Scott et al., 2014, 2010). Therefore, we first quantified the fluorescence
156 concentration of a monomeric superfolder green fluorescent protein (msfGFP) fusion to the ribosomal
157 protein RpsB (expressed from the native chromosomal locus) in 1N and multi-N cells in M9glyCAAT as
158 a function of cell area. We found it to be almost identical between the two CRISPRi strains and
159 relatively constant across cell areas, regardless of DNA content (Figure 2A).
160 To exclude the possibility that the msfGFP tag altered the synthesis of RpsB or that this protein
161 behaved differently from other ribosomal proteins, we adapted a TMT mass spectrometry (MS)
162 method recently developed to examine cell size-dependent proteome scaling in yeast and human
163 cells (Lanz et al., 2022). Note that, for the CRISPRi *oriC* strain, a minority (~10-15%) of cells have more
164 than one nucleoid. These cells were excluded from the analysis of our single-cell microscopy
165 experiments. However, this could not be done for the TMT-MS experiments, which provide
166 population-level measurements. Therefore, for this TMT-MS section, we will refer to the CRISPRi *oriC*
167 cell population as "1N-rich" cells, instead of only "1N" cells. Using the TMT-MS approach, we found
168 that the relative concentration of all (54) high-abundance ribosomal proteins (including untagged
169 RpsB) remained approximately constant across all sizes of 1N-rich cells, and was similar between 1N-
170 rich and multi-N cells (Figure 2B). Only the relative concentration of the ribosomal protein L31B, a
171 stationary phase paralog of the more prevalent exponential phase ribosomal protein L31A (Lilleorg et
172 al., 2019), significantly decreased in 1N cells (Dataset 1). Thus, the concentration of ribosomal
173 proteins does not explain the difference in growth rate between cells with different ploidy.

174

175 **The fraction of active ribosomes is reduced in genome-diluted cells.**

176 To more specifically probe the translational activity of ribosomes in 1N cells, we performed single-
177 molecule tracking in live cells growing in M9glyCAAT. Ribosomes are expected to exhibit at least two
178 different dynamic states: slow mobility when active (i.e., engaged in translation on the mRNA, often
179 in polyribosome form), and faster mobility when inactive ribosomes (or ribosomal subunits) are
180 diffusing in the cytoplasm (Mohapatra and Weisshaar, 2018; Sanamrad et al., 2014). To track
181 ribosomes, we introduced a HaloTag fusion to RpsB (through genetic modification at the endogenous
182 chromosomal locus) and labeled the HaloTag using the membrane-permeable Janelia Fluor 549 (JF549)
183 fluorescent dye (Grimm et al., 2015). We quantified the apparent diffusion coefficient (D_a) of single-
184 molecule tracks in WT cells, as well as in 1N and multi-N cells at multiple time points following CRISPRi
185 induction (Figure 2C). We found that the distribution of D_a in multi-N cells of all sizes (~2-10 μm^2) was
186 similar to that in WT cells despite the considerable differences in cell sizes. In contrast, 1N cells
187 displayed distributions clearly distinct from WT and multi-N cells, gradually shifting toward faster
188 mobilities (higher D_a) with increasing cell size. This shift suggests that ribosome activity is altered in
189 1N cells.

190 Gaussian fitting of the D_a logarithmic data in WT cells revealed two predominant dynamic
191 states of ribosomes: a slow-diffusing and a fast-diffusing state, representing 77 ± 1% (mean ± standard
192 error of the mean (SEM)) and 20 ± 1% of the ribosome population, respectively (Figure 2D). In addition,
193 we observed a small fraction (3.2 ± 0.5%) of faster-moving molecules with D_a expected for freely-
194 diffusing proteins (Banaz et al., 2019; Elowitz et al., 1999), likely indicative of a small pool of free RpsB-
195 HaloTag proteins (i.e., not assembled into ribosomes). To confirm that the slow-diffusing fraction

196 corresponded to translationally active ribosomes, we showed that this fraction nearly vanished (down
197 to 1.10 ± 0.02%) when cells were depleted of mRNAs following 30 min treatment with the
198 transcription inhibitor rifampicin (Figure 2 – figure supplement 1). The estimated fraction (~77%) of
199 active ribosomes in untreated cells was in good agreement with previous single-molecule and
200 biochemical studies under similar growth conditions (Forchhammer and Lindahl, 1971; Mohapatra
201 and Weisshaar, 2018; Sanamrad et al., 2014).

202 Upon fitting the D_a values of ribosomes in WT and 1N cells (Figure 2E), we observed a
203 significant reduction in the slow-diffusing ribosome population in 1N cells of increasing area (Figure 2
204 – figure supplement 2). Quantification of the active (slow-diffusing) ribosome fraction per cell
205 revealed that 1N cells have overall lower ribosome activity than WT cells, and that ribosome activity
206 decreases monotonically with increasing cell area (Figure 2F). In contrast, ribosome activity in multi-
207 N cells remained the same as in WT across different cell sizes (Figure 2G).

208 To estimate the total number of active ribosomes per cell, we multiplied the total amount of
209 ribosomes by the fraction of active ribosomes and plotted the result as a function of cell area (Figure
210 2H). We found that the difference in the total number of active ribosomes between 1N and multi-N
211 cells matches the observed difference in growth rate (Figure 2H), indicating that cell growth rate is
212 directly proportional to the increase in total active ribosomes. Altogether, the results are consistent
213 with the hypothesis that DNA limitation decreases total ribosome activity, which, in turn, reduces the
214 growth rate.

215

216 **Genome dilution reduces the activity of RNA polymerases.**

217 We reasoned that the observed changes in ribosome activity in 1N cells may reflect the available

218 pool of transcripts. If true, we would expect the total activity of RNAPs to be reduced in 1N cells. The
219 total activity of RNAPs in cells is determined by the concentration of RNAPs multiplied by the fraction
220 of active RNAPs. Therefore, we first determined whether RNAP concentration was lower in 1N cells
221 relative to multi-N cells by quantifying the fluorescence intensity of a functional fusion of YFP to the
222 RNAP β' subunit (encoded by *rpoC*) expressed from its native chromosomal locus. As expected, RNAP
223 concentration remained constant in multi-N cells (Figure 3A). In 1N cells, the RNAP concentration
224 increased with cell size (Figure 3A), the opposite of what would be expected to explain the growth
225 rate defect. We confirmed this increasing trend in concentration for other protein subunits of the
226 core RNAP and the primary sigma factor σ^{70} (encoded by *rpoD*) using TMT-MS (Figure 4B), clearly
227 demonstrating that the abundance of RNAPs was not the limiting factor.

228 To quantify RNAP activity in 1N and multi-N cells, we performed single-molecule tracking in
229 live cells using a functional fusion of HaloTag to the β' protein subunit RpoC labeled with the JF549
230 dye. As expected, the D_a values of RpoC-HaloTag in multi-N cells were distributed similarly to those in
231 WT cells (Figure 3C). In contrast, the distribution in 1N cells changed gradually toward higher D_a values
232 (faster mobility) with increasing cell size (Figure 3C). As with ribosomes, RNAPs primarily exhibited
233 two major states of diffusivity (Figure 3D): a slower-diffusing fraction (49 ± 4%; mean ± SEM) and a
234 faster-diffusing fraction (49 ± 4%), likely representing transcriptionally active RNAPs and inactive,
235 diffusing RNAPs, respectively. A small fraction of RpoC-HaloTag (2 ± 0.1%) diffused very fast, with D_a
236 values expected for free proteins, suggesting that it reflects the few β' proteins not assembled into
237 the RNAP core complex. Using rifampicin treatment, we confirmed that the slowest state corresponds
238 to RNAPs actively engaged in transcription (Figure 3 – figure supplement 1). In these rifampicin-
239 treated cells, the slow-diffusing fraction was reduced to 13 ± 4%. Rifampicin does not prevent

240 promoter binding or open complex formation and instead blocks transcription elongation following
241 the synthesis of 3-nucleotide-long RNAs (Campbell et al., 2001). Thus, the observation that slow-
242 moving RNAPs did not completely disappear after rifampicin treatment is consistent with the
243 mechanism of action of the drug, leaving a fraction of RNAPs bound at promoter sites.

244 Unlike in WT and multi-N cells, the fraction of active RNAPs in 1N cells decreased
245 monotonically with increasing cell area (Figure 3F-G). However, because the RNAP concentration
246 simultaneously increased in 1N cells, it remained possible that the total amount of active RNAP, which
247 is the relevant metric of transcription activity, remained equal to that of multi-N cells. By calculating
248 the total amount of active RNAPs, we showed that the decrease in the active fraction in 1N cells was
249 not the mere result of the increase in RNAP concentration. Indeed, the total amount of active RNAPs
250 hardly increased with cell size in 1N cells whereas it increased proportionally with cell size in both
251 multi-N and WT cells (Figure 3H).

252 A recent study has shown that the intracellular concentration of Rsd, the anti-sigma factor of
253 σ^{70}, increases in WT cells under slower growth conditions, causing a reduction in global mRNA
254 synthesis (Balakrishnan et al., 2022). Therefore, we verified that the concentration of Rsd remains
255 approximately constant in both 1N-rich and multi-N cells based on our TMT-MS data (Figure 3 – figure
256 supplement 2), eliminating Rsd as a possible source of reduced RNAP activity in 1N cells. Instead, our
257 data supports the notion that substrate (DNA) limitation leads to a reduced transcription rate, which
258 reduces the pool of transcripts available for ribosomes.

259

260

261

262 **Chromosome dilution reduces the concentration of transcripts.**

263 To test the idea that genome dilution affects growth rate through transcript limitation, we performed
264 live-cell staining with SYTO RNASelect, a fluorogenic RNA-specific dye (Wu et al., 2020). This dye has
265 been proposed to preferentially bind mRNAs based on the observed decay of intracellular RNASelect
266 signal in *E. coli* during rifampicin treatment (Bakshi et al., 2014), which causes mRNA depletion.
267 However, a recent study has shown that the levels of ribosomal RNAs (rRNAs) also decrease in
268 rifampicin-treated cells (Hamouche et al., 2021), though at a slower rate than mRNAs. Therefore, to
269 complement the RNASelect staining experiments and examine the potential effect of genome dilution
270 specifically on rRNAs, we also carried out fluorescence in situ hybridization (FISH) microscopy on fixed
271 cells using EUB338-Cy3, a DNA probe complementary to an exposed region in the 16S rRNA (Amann
272 et al., 1990). For both experiments, we mixed 1N cells with multi-N cells of similar size ranges prior to
273 incubation with RNASelect or EUB338-Cy3 to mitigate variability in staining. We next imaged the
274 mixed populations and distinguished 1N cells from multi-N cells by examining the difference in
275 nucleoid number (one vs. multiple) per cell using HU-mCherry or DAPI as a DNA marker (Figure 4A).
276 Single cells were sampled to ensure that the cell area distributions of the two populations matched
277 (Figure 4 – figure supplement 1).

278 Comparison between the two sampled populations revealed a reduced concentration of
279 RNASelect signal by ~50% in 1N cells relative to multi-N cells for a cell size range of 4 to 10 μm^2 (Figure
280 4B-C). For a similar cell area range, the EUB338 signal concentration was reduced by only ~5%.
281 Furthermore, the RNASelect concentration ratio between 1N and multi-N cells displayed a rapid
282 exponential decay with increasing cell area, whereas the decrease in EUB338 concentration ratio was
283 considerably slower (Figure 4D).

284 To verify that the decrease in RNASelect signal in 1N cells was not caused by a global change
285 in membrane permeability to small molecules, we performed similar live-cell staining experiments
286 with the HaloTag dye JF549 in CRISPRi strains expressing RpoC-HaloTag (Figure 4 – figure supplement
287 2A). We matched the cell distributions between 1N and multi-N cells for fair comparison (Figure 4 –
288 figure supplement 2B). Because RpoC concentration increases with cell size in 1N cells relative to
289 multi-N cells (Figure 3A-B), we expected a similar increase in the ratio of JF549 signal between these
290 two cell types if the membrane permeability to small molecules remained unchanged. This is indeed
291 what we observed (Figure 4 – figure supplement 2C-E). In parallel, to examine the ability of our rRNA
292 FISH method to detect a reduction in 16S rRNA concentrations, we compared the EUB338 staining of
293 wildtype cells (MG1655) growing in M9 glycerol with or without casamino acids and thiamine
294 (M9glyCAAT vs M9gly), which results in a difference in growth rate of ~40% (Govers et al., 2024) due
295 to the expected lower concentration of ribosomes and thus 16S rRNAs in nutrient-poor media.
296 Consistent with this expectation, we found that the EUB338 concentration signal was reduced by ~50%
297 in M9gly relative to M9glyCAAT (Figure 4 – figure supplement 3). Given these validations, our results
298 in Figure 4 suggest that the RNASelect signal primarily reflects the bulk of mRNAs, and that the
299 concentration of mRNAs decreases more rapidly than that of rRNAs upon genome dilution.
300
301 **DNA dilution can result in sub-exponential growth through mRNA limitation.**
302 In a previous theoretical study, Lin and Amir (2018) considered distinct scenarios for gene expression.
303 Their model predicted that if DNA and mRNAs are in excess, cells will display exponential growth. On
304 the other hand, cells will adopt linear growth if DNA and mRNAs become limiting. Our experiments
305 showed that 1N cells indeed converge toward linear growth (toward slope $= 0$ in Figure 1C), though

306 the complete transition to linear growth required a large decrease in DNA concentration. To
307 quantitatively examine this transition from exponential to linear growth through genome dilution, we
308 developed two deterministic ordinary differential equation (ODE) models of the flow of genetic
309 information that include parameters for the fractions of active RNAPs and ribosomes. In these models,
310 the dynamics of mRNA (X) and protein (Y) numbers in the cell are described by

311 $$\frac{dX}{dt} = r_1 \alpha_{RNAP}(X,Y)Y - \delta X \qquad \text{(Eq.1)}$$

312 $$\frac{dY}{dt} = r_2 \alpha_{ribo}(X,Y)Y \qquad \text{(Eq.2)}$$

313 where r_1 is the bulk transcription rate normalized by the total protein number, r_2 is the bulk
314 translation rate normalized by the total protein number, and δ is the mRNA degradation rate. The
315 quantities $\alpha_{RNAP}(X,Y)$ and $\alpha_{ribo}(X,Y)$ are the fractions of active RNAPs and ribosomes expressed
316 as a percentage of the total RNAPs and ribosomes. For simplicity, we assumed that protein
317 degradation is negligible and that the cell volume and the number of rRNAs grow proportional to
318 protein Y (Balakrishnan et al., 2022; Lin and Amir, 2018). As a result, the rate of protein increase $\frac{dY}{dt}$
319 corresponds to the absolute growth rate and the relative protein increase rate $\frac{1}{Y}\frac{dY}{dt}$ corresponds to
320 the relative growth rate. For detailed description and estimation of the model parameters, see Table
321 1 and Appendices 1 and 2.

322 Based on the function form of $\alpha_{RNAP}(X,Y)$, we consider two ODE model variants. In model A,
323 we assumed that DNA is a limiting factor while RNAPs are not. In model B, both DNA and RNAPs were
324 considered as growth-limiting factors. In both models, higher DNA concentration increases the
325 probability that an RNAP will encounter and bind to a promoter. In model terms, α_{RNAP} (as well as
326 the downstream transcription rate) increases with DNA concentration. In model A, we examined the

327 effect of DNA limitation with minimal mathematical complexity by assuming that the proteome does
328 not change (see Materials and Methods). In model B, we considered RNAP kinetics (with three
329 different RNAP states: free, promoter-bound, and transcribing) based on the law of mass action (see
330 Materials and Methods and Appendix 3) and took into consideration the experimentally observed
331 increase in RNAP concentration in 1N cells (Figure 3A-B). For both models, α_{RNAP} depended on DNA
332 concentration.

333 We used these models to perform simulations and compared the results to our measurements,
334 starting with parameter values extracted or estimated from the *E. coli* literature (Table 2). In 1N cells,
335 the DNA amount was fixed to one genome while it scaled with cell volume in multi-N cells. The
336 parameters were then optimized to fit six experimental datasets simultaneously: cell growth rate, the
337 fraction of active RNAPs, and the fraction of active ribosomes in both 1N and multi-N cells (see
338 Materials and Methods and Appendix 4).

339 As shown in Figure 5A-D (model A) and Figure 5 – figure supplement 1 (model B), both models
340 performed similarly after parameter optimization. While the model curves (solid lines) did not
341 perfectly match the average behavior of our experimental results (open squares), they displayed
342 similar trends and fell within the variance of the single-cell data (dots). The models showed that multi-
343 N cells (blue) display balanced exponential growth while the 1N cells (yellow) exhibit sub-exponential
344 growth (Figure 5A and Figure 5 – figure supplement 1A), consistent with experiments. At the same
345 time, both models recapitulated the observed experimental trends in active fractions of both
346 ribosomes and RNAPs, which remained constant in multi-N cells while decaying gradually with DNA
347 concentration in 1N cells (Figure 5B-D and Figure 5 – figure supplement 1B-D).

348 The simulation results of 1N cells suggest the following cascade of events when DNA is limiting.
349 Lower DNA concentration results in fewer substrates for RNAPs, which reduces the transcription rate.
350 This results in a decrease in mRNA concentration. As mRNAs become limiting, the fraction of
351 ribosomes engaged in translation decreases. This, in turn, decreases the rate of bulk protein synthesis,
352 which decreases the relative growth rate. The greater the DNA dilution (through cell growth), the
353 more severe the downstream effects become, explaining the decay in relative growth rate in 1N cells
354 (Figure 5E).
355
356 **Genome dilution rapidly limits RNAP activity under both nutrient-rich and -poor conditions, but the**
357 **extent of downstream effects on ribosome activity and cell growth can vary with the nutrient**
358 **condition.**
359 In the relatively nutrient-rich M9glyCAAT condition, WT cells at birth are expected to have higher DNA
360 content than 1N cells on average due to overlapping DNA replication (Fossum et al., 2007). To examine
361 whether cells are also subject to DNA-limited transcription when multi-fork DNA replication is rare or
362 nonexistent, we examined the total RNAP activity of 1N cells relative to WT cells in two different
363 nutrient-poor media, M9gly and M9 L-alanine (M9ala). Abundance and diffusivity measurements of
364 RpoC-YFP-labeled RNAPs (Figure 6 – figure supplement 1) showed that the scaling between the total
365 amount of active RNAPs (i.e., global transcriptional activity) and cell area was strongly reduced in 1N
366 cells, even within the range of WT cell sizes (Figure 6A-B). Thus, genome dilution rapidly limits global
367 transcription in nutrient-poor (slow growth) conditions, as in richer (faster growth) conditions (Figure
368 3H).

369 In contrast, abundance and diffusivity measurements of fluorescently labeled ribosomes in
370 cells growing in M9gly and M9ala (Figure 6 – figure supplement 2) revealed that the total amount of
371 active ribosomes (i.e., bulk translational activity) and the absolute growth rate of 1N cells started to
372 deviate from proportional scaling with cell areas mostly when cells reached large (non-physiological)
373 sizes (Figure 6C-D). As a result, the difference in absolute growth rate between 1N and multi-N cells
374 was not as pronounced as in cells growing in the richer M9glyCAAT medium (Figure 6E-F vs. Figure
375 1C). This suggests that one or more cellular buffering activities may help mitigate the limitation of
376 DNA concentration on transcription in nutrient-poor media (see Discussion).
377
378 **Genome dilution changes the composition of the transcriptome and proteome.**
379 The fact that the relative concentrations of ribosomal proteins and RNAP subunits scaled differently
380 with cell area in 1N cells (Figures 2A-B and 3A-B) indicated that all genes are not equally impacted by
381 DNA dilution. In yeast and mammalian cells, a decrease in the DNA-per-volume ratio has recently
382 been demonstrated to alter the composition of the proteome, with some proteins increasing in
383 relative concentration while others become comparatively more diluted (Lanz et al., 2023, 2022). To
384 examine whether this effect may be conserved across domains of life, we used our proteomic TMT-
385 MS data on the CRISPRi strains to quantify the relative concentration of each detected protein across
386 cell areas following DNA replication or cell division arrest in M9glyCAAT. For each protein, we
387 calculated the relative change in concentration against the relative change in cell size through
388 regression fitting, yielding a slope value. A slope of zero indicates that the concentration of a protein
389 remains constant relative to the proteome whereas a slope of -1 (or 1) means that the relative
390 concentration is decreasing (or increasing) by two-fold with each cell size doubling (Figure 7A).

391 We found that the slope distribution was highly reproducible between biological replicates
392 (Figure 7 – figure supplement 1A-B) but drastically different between 1N-rich cells and multi-N cells
393 (Figure 7B, Dataset 1). In the control multi-N cells where the genome concentration does not change
394 with cell growth, the relative concentration of ~94% of the detected proteins (2217/2360) remained
395 roughly constant, with their relative concentrations decreasing or increasing by less than 20% per cell
396 size doubling (i.e., slopes > -0.2 or < 0.2; Figure 7B and Dataset 1). This suggests that protein amounts
397 largely scale with cell size, as generally assumed. However, in 1N-rich cells where the genome dilutes
398 with cell growth, the proportion of detected proteins with slopes near zero (> -0.2 or < 0.2) dropped
399 to ~37% (859/2360) (Figure 7B and Dataset 1). A principal component analysis on the relative protein
400 concentration during cell growth confirmed that the relative proteome composition changed
401 proportionally with genome dilution (1N-rich cells), whereas it remained constant when the DNA-to-
402 cell volume ratio was maintained (multi-N cells) (Figure 7C).
403 To examine whether the proteome scaling behavior stems from differential changes in mRNA
404 levels, we performed transcriptomic (RNA-seq) analysis on two biological replicates of 1N-rich cells at
405 different time points after induction of DNA replication arrest. The two replicates were strongly
406 correlated at the transcript level (Spearman $\rho = 0.91$, p-value $< 10^{-10}$, Figure 7 – figure supplement 1C).
407 We also found a strong correlation (Spearman $\rho = 0.76$, p-value $< 10^{-10}$) in scaling behavior with cell
408 area between mRNAs and proteins across the genome of 1N-rich cells (Figure 7D and Dataset 2),
409 indicating that most of the changes in protein levels observed upon genome dilution take place at the
410 mRNA level.
411 To investigate whether central processes may contribute to the observed transcriptome
412 remodeling during DNA limitation, we examined whether the RNA slopes correlate with gene-specific

413 rates of transcription initiation or mRNA degradation obtained from a published dataset (Balakrishnan
414 et al., 2022). Note that the reference dataset was generated from experiments on *E. coli* growing in
415 M9 glucose (M9glu) and not M9glyCAAT. However, both media give similar growth rates (Govers et
416 al., 2024) and our transcriptome measurements agree well with the reference data in terms of mRNA
417 abundance (Spearman $\rho = 0.76$, p-value $< 10^{-10}$, Figure 7 – figure supplement 2A). We found no
418 significant correlation between the rates of transcription initiation from the reference dataset and
419 RNA or protein slopes across genes (Figure 7 – figure supplement 2B-C). Consistent with this finding,
420 mRNA abundance was not a predictor of RNA slopes (Figure 7E). This was somewhat surprising as one
421 might anticipate highly transcribed genes to saturate with RNAPs faster than other genes. However,
422 we found that the mRNA degradation rate partly explains the variance in RNA and protein slopes.
423 Specifically, for genes producing short-lived transcripts (decay rate $> 0.7\ \mathrm{min}^{-1}$), the RNA and protein
424 slopes slightly negatively correlated with the rate of mRNA decay (Spearman correlation coefficient ρ
425 $= -0.18$, p-value $< 10^{-10}$, Figure 7F and Figure 7 – figure supplement 2D, Dataset 3). These results
426 suggest that genes that generate short-lived mRNAs are more susceptible to DNA limitation,
427 presumably because their mRNAs are more rapidly diluted with cell growth due to their fast decay.

428 Next, we examined whether genes reported to be essential for viability in three independent
429 studies (Gerdes et al., 2003; Goodall et al., 2018; Yamazaki et al., 2008) displayed biases in RNA and
430 protein slopes given the importance of their products for cell growth. Remarkably, essential genes,
431 which share similar mRNA decay rates as other genes (Figure 7 – figure supplement 2E, Mann-
432 Whittney p-value > 0.01), tended to exhibit superscaling behavior in 1N cells as shown by their
433 enrichment in positive RNA slopes regardless of the selected dataset (Figure 7G, Mann-Whittney p-

434 value < 10^{-10}). This suggests that cells have evolved regulatory mechanisms to minimize dilution of
435 mRNAs encoded by essential genes.
436
437 **DISCUSSION**
438 Our data suggest that DNA limitation in *E. coli* cells affects cell growth rate through modulation of
439 downstream transcription and translation activities (Figures 1-7 and associated figure supplements).
440 The fact that DNA limitation for cellular growth was also observed in *C. crescentus* (Figure 1 – Figure
441 supplement 8) is significant not only because this bacterium is distantly related to *E. coli*, but also
442 because it has a different pattern of cell wall growth and distinct control mechanisms of DNA
443 replication (Aaron et al., 2007; Banerjee et al., 2017; Frandi and Collier, 2019; Lasker et al., 2016;
444 Terrana and Newton, 1975). This suggests that DNA concentration may be a prevalent growth
445 constraint across bacterial species. It also helps explain why the timing of DNA replication in bacteria
446 is so robustly linked to cell volume across environmental and genetic conditions that affect cell size
447 (Donachie, 1968; Govers et al., 2024; Sauls et al., 2019; Si et al., 2017; Zheng et al., 2016).
448 Comparison with studies on eukaryotic cells suggests conservation of gene expression
449 principles across domains of life. For instance, in yeast, it has been shown that the global transcription
450 rate in G1-arrested cells is higher in diploids than haploids of similar sizes (Swaffer et al., 2023),
451 consistent with DNA concentration being a limiting factor for transcription. Furthermore, in both yeast
452 and mammalian cells, small G1-arrested cells display higher growth rate (or global RNA or protein
453 synthesis rate) per cell volume than large ones that have exceeded a certain volume (Cadart et al.,
454 2018; Liu et al., 2022; Neurohr et al., 2019; Zatulovskiy et al., 2022). This is likely due to a change in

455 genome concentration rather than a change in cell volume, as the relative growth rate is unaffected
456 in very large cells as long as they undergo a proportional increase in ploidy (Mu et al., 2020).

457 We found that even a relatively small dilution in DNA concentration—as expected in DNA
458 replication-arrested *E. coli* cells that are still within or close to physiological sizes—results in a
459 reduction of total RNAP activity in both rich and poor media (Figures 3H and 6A-B). Crude estimations
460 suggest that ≤ 40% DNA dilution is sufficient to negatively affect transcription (total RNAP activity) in
461 M9glyCAAT, whereas the same effect was observed after less than ~10% dilution in poor media
462 (M9gly or M9ala) (see Materials and Methods). Thus, cells appear to live at the cusp of DNA limitation
463 for transcription, especially under slow growth (nutrient-poor) conditions. This suggests that cells
464 make enough—but not too much—DNA, presumably because DNA replication is a costly process that
465 represents a significant fraction (~6% in minimal media) of the cellular energy budget (Neidhardt et
466 al., 1990).

467 What may be the implications of living close to DNA limitation? While *E. coli* carefully controls
468 its genome concentration across various conditions and growth rates at the population level
469 (Donachie, 1968; Govers et al., 2024; Si et al., 2017; Zheng et al., 2016), there remains variability in
470 DNA concentration at the single-cell level, with some cells initiating DNA replication at smaller or
471 larger cell volumes than others (Si et al., 2019; Witz et al., 2019). In future studies, it will be interesting
472 to explore whether this variability contributes to the known growth rate heterogeneity across isogenic
473 cells (Lin and Jacobs-Wagner, 2022; Wang et al., 2010). It is also tempting to speculate that changes
474 in genome concentration may, at least in part, contribute to the deviations from exponential growth
475 that have been reported during the division cycle of *B. subtilis*, *E. coli,* and stalked *C. crescentus*
476 progeny (Banerjee et al., 2017; Kar et al., 2021; Nordholt et al., 2020; Reshes et al., 2008). More

477 substantial forms of DNA dilution may occur under other circumstances. *C. crescentus* cells in
478 freshwater lakes often form long filaments during algal blooms in the summer months (Heinrich et al.,
479 2019). These filament cells are thought to be the result of a DNA replication arrest in response to the
480 combination of an alkaline pH, a depletion in phosphate, and an excess of ammonium (Heinrich et al.,
481 2019). Another example is illustrated by the Lyme disease agent *Borrelia burgdorferi*. This pathogen,
482 which forms long polyploid cells during exponential growth, experiences a progressive decrease in
483 genome concentration (up to eightfold) in stationary phase laboratory cultures through the gradual
484 loss of genome copies (Takacs et al., 2022).

485 In yeast cells, decreased mRNA turnover combined with increased RNAP II gene occupancy
486 helps mitigate DNA dilution on global transcriptional activities up to a certain (non-physiological) cell
487 volume, beyond which the compensation breaks down (Swaffer et al., 2023; Zhurinsky et al., 2010).
488 Such buffering activities, which are consistent with model predictions (Figure 4 – figure supplement
489 5) (Swaffer et al., 2023), may also be at play in *E. coli* in a growth medium-dependent manner. While
490 genome dilution rapidly impacted transcription in all tested media based on total RNAP activity
491 measurements (Figures 3H and 6A-B), we found that the negative impact on downstream processes—
492 total ribosome activity and cell growth—occurred later (i.e., mostly beyond physiological cell sizes) in
493 M9gly and M9ala (Figure 6C-F), in contrast to M9glyCAAT (Figures 1B-C and 2H). This suggests the
494 existence of mechanisms that compensate for DNA-limited transcription under slow growth such as
495 a decrease in mRNA decay, an increase in ribosome loading, and/or an increase in translation
496 elongation rate. Perhaps such buffering activities are not as effective under nutrient-rich conditions
497 due to the rapid mRNA dilution during fast growth. Testing these hypotheses will require future
498 experimentation.

499 Another remarkable similarity between bacteria and eukaryotes is the effect of genome
500 concentration on proteome composition. While protein abundance is typically assumed to scale with
501 cell size in bacteria, we found that this is true at the proteome level only when ploidy also scales
502 (Figure 7B). This requirement was also recently shown in yeast and mammalian cells (Lanz et al., 2023,
503 2022). This conservation of scaling principle further highlights the importance of genome
504 concentration in controlling protein expression.

505 What determines the scaling behavior of proteins in *E. coli* is not clear. We found that it largely
506 occurs at the mRNA level (Figure 7D), and that short-lived mRNAs are slightly more susceptible to
507 subscaling behavior (Figure 7F and Figure 7 – figure supplement 2D). Conversely, the majority of
508 essential genes (Gerdes et al., 2003; Goodall et al., 2018; Yamazaki et al., 2008) tended to display
509 superscaling behavior relative to the rest of the genome (Figure 7G, Dataset 3). This suggests the
510 existence of regulatory mechanisms that prioritize the expression of essential genes over less
511 important ones when genome concentration becomes limiting for cell growth.

512 While the scaling of proteins in 1N cells is largely driven by that of mRNAs (Figure 7D), we
513 found that protein slopes, but not RNA slopes, displayed a slight yet significant positive correlation
514 (Spearman $\rho = 0.23$, p-value $< 10^{-10}$) with *oriC* proximity for genes within 1.35 Mb from *oriC* (Figure 7
515 – Figure supplement 3A-B). Why and how this occurs is unclear, but it suggests that mRNA-
516 independent mechanisms (i.e., independent of mRNA synthesis or decay) also contribute to protein
517 scaling behavior. At the GO term level, we did not identify any specific trends in proteome changes
518 (Dataset 1). In eukaryotic cells, histones are known to scale in proportion with DNA rather than cell
519 size (Claude et al., 2021; Swaffer et al., 2021; Wiśniewski et al., 2014). As a result, their concentration
520 proportionally decreases (i.e., slope = -1) with growth in G1 phase. In *E. coli*, the relative abundance

521 of some nucleoid-associated proteins (H-NS, HU and Dps) decreased with genome dilution, while
522 others (IHF and Fis) displayed superscaling (protein slopes > 0) behavior (Figure 7 – figure supplement
523 4).

524 Given the prevalent use of *E. coli* in the biotechnological world, we hope that our findings will
525 be helpful to future bioengineering studies and growth rate optimization efforts. We show that
526 protein content and cellular growth depend on the ploidy-to-cell volume ratio (Figures 1 and 7). As
527 such, models of protein expression that take into consideration the DNA concentration and the active
528 number of RNAPs and ribosomes could provide a starting point to identify the parameter space that
529 leads to growth rate improvement. Experimentally, it will be important to determine which specific
530 genes exert the largest growth rate-limiting effect. In this context, the few essential genes with strong
531 subscaling behavior (large negative values of RNA and protein slopes) in 1N cells (Figure 7G, Dataset
532 3) suggest potential candidates for future studies given the rapid dilution of their mRNAs and proteins
533 relative to other genes.

534

535 **MATERIALS AND METHODS**

536 **Bacterial strains and growth conditions**

537 Bacterial strains and their construction can be found in Table 3. Oligomers used for polymerase chain
538 reaction (PCR) are listed in Table 4. Transductions and Gibson assemblies were performed as
539 described previously (Ely, 1991; Thomason et al., 2007).

540 *E. coli* strains were grown at 37°C in M9 minimal media with different supplements: 0.2%
541 glycerol, 0.1% casamino acids, and 1 µg/ml thiamine (M9glyCAAT); 0.2% glycerol (M9gly); or 0.2% L-
542 alanine (M9ala). For microscopy, cells were grown in culture tubes to stationary phase, diluted

543 10,000-fold, and grown until they reached an optical density (OD_{600}) between 0.05 and 0.2. For
544 imaging, cells were then spotted onto a 1% agarose pad on a glass slide prepared with the appropriate
545 M9 medium and covered by a #1.5 thickness coverslip.

546 For time-lapse microscopy experiments with the CRISPRi strains (Li et al., 2016), the cells were
547 induced by adding L-arabinose (0.2%) to liquid cultures after which a sample (~1 µl) was immediately
548 collected and spotted on an agarose pad containing the appropriate growth medium supplemented
549 with 0.2% L-arabinose. This was promptly followed by imaging of individual cells. To determine the
550 1N status of CRISPRi *oriC* cells, we monitored the last division and number of nucleoids based on HU-
551 mCherry fluorescence. In Figure 1B, the time point "0 min" refers to the time when cells have reached
552 the 1N status.

553 For population microscopy experiments with the CRISPRi strains, the cells were induced with
554 0.2% L-arabinose and allowed to grow in normal conditions until a specific time point (depending on
555 the growth medium and strain) was reached, after which the cells were spotted on an agarose pad
556 containing the appropriate growth medium and 0.2% L-arabinose, and imaged (see information for
557 each experiment in the corresponding Figure). Note that the CRISPRi strains do not metabolize
558 arabinose due to the *araBAD* deletion.

559 For the TMT-MS experiments, CRISPRi *oriC* (SJ_XTL676) cells were supplemented with 0.2% L-
560 arabinose and allowed to grow in liquid M9glyCAAT cultures at 37°C for 0, 120, 180, 240, and 300 min
561 before harvesting, while CRISPRi *ftsZ* (SJ_XTL229) cells were collected after 0, 60, and 120 min after
562 arabinose addition. For RNA-seq experiments, CRISPRi *oriC* (SJ_XTL676) cells were supplemented with
563 0.2% L-arabinose and allowed to grow in liquid M9glyCAAT cultures 37°C for 60, 120 200, and 240 min
564 before harvesting.

565 Strains carrying the *dnaC2* mutation were grown at a permissive temperature of 30°C and then
566 shifted to 37°C to block replication initiation. Transcription inhibition and mRNA depletion were
567 achieved by exposing cells to 200 µg/ml rifampicin for 30 min before spotting cells on a 1% agarose
568 pad containing the appropriate M9 medium and rifampicin concentration. The HaloTag was labeled
569 with Janelia Fluor 549 (JF549) ligand (Grimm et al., 2015) as described previously (Banaz et al., 2019).
570 Briefly, cells were incubated with 2.5 µM of the JF549 ligand for 30 min while shaking, washed 5 times
571 with growth medium, and allowed to recover for several generations (while remaining in exponential
572 phase) prior to imaging.

573 *C. crescentus* strains were grown at 22˚C in PYE (2 g/L bacto-peptone, 1 g/L yeast extract, 1
574 mM $MgSO_4$, 0.5 mM $CaCl_2$) supplemented with 0.03% xylose to induce production of the essential
575 protein FtsZ (Wang et al., 2001) or DnaA (Gorbatyuk and Marczynski, 2001). For microscopy, cells
576 were grown in overnight cultures, then diluted at least 1:10,000 in fresh medium and grown to
577 exponential phase (OD_{660} nm < 0.3). To induce cell filamentation by depleting FtsZ or DnaA, xylose
578 was removed from the medium by pelleting cells, washing twice with PYE, and resuspending in fresh
579 PYE. Cultures were then allowed to grow for an additional 30 min to allow ongoing cell division cycles
580 to complete before spotting on 1% agarose pads containing PYE but lacking xylose to deplete FtsZ or
581 DnaA. To estimate the concentration of fluorescently-labeled ribosomes and RNAPs by fluorescence
582 microscopy, cultures were sampled at 0, 4, 8, and sometimes 12 h following xylose depletion with 30
583 min outgrowth to allow late predivisional cells time to divide before spotting. For timelapse
584 microscopy, new pads were spotted with cells from the original culture at 0, 4, 8, and sometimes 12
585 h following xylose removal with 30 min outgrowth in a liquid PYE medium.

586

587 **Epifluorescence microscopy**

588 For *E. coli*, phase contrast and fluorescence imaging (except for the RpoC-HaloTag-JF549
589 epifluorescence experiment), were performed on a Nikon Ti2 microscope equipped with a Perfect
590 Focus System, a 100x Plan Apo λ 1.45 NA oil immersion objective, a motorized stage, a Prime BSI
591 sCMOS camera (Photometrics), and a temperature chamber (Okolabs). Fluorescence emission was
592 collected during a 100 or 200 ms exposure time provided by a Spectra III Light Engine LED excitation
593 source (Lumencor): mCherry – 594 nm excitation, DAPI/FITC/TxRed filter cube (polychroic FF-
594 409/493/596-Di02, triple-pass emitter FF-1-432/523/702-25); GFP and SYTO RNASelect – 488 nm
595 excitation, DAPI/FITC/TxRed polychroic filter cube, and an ET525/50M emission filter; YFP – 514 nm
596 excitation, CFP/YFP/mCherry filter cube (polychroic FF-459/526/596-Di01, triple-pass emitter FF-1-
597 475/543/702-25), and a FF02-525/40-25 emission filter. The microscope was controlled using NIS-
598 Elements AR. For time-lapse imaging, phase images were collected every 5 min.

599 Epifluorescence snapshots of RpoC-HaloTag-JF549 were taken using a Nikon Ti microscope,
600 equipped with a Perfect Focus System, a 100x Plan Apo λ 1.45 NA oil immersion objective, a motorized
601 stage and an ORCA Flash 4.0 camera (Hamamatsu). Fluorescence emission was collected during a 200
602 ms exposure time provided by a Sola solid state white light source (Lumencor) and a Cy3 filter cube
603 (excitation AT545/25x, dichroic T565lpxr, emission ET605/70m). The microscope was controlled using
604 NIS-Elements AR. The same microscope and filters were used to capture the EUB338-Cy3 fluorescence,
605 but using a 100-ms exposure time. The same microscope, with a DAPI filter cube (excitation ET395/25x,
606 dichroic T425lpxr, emission ET460/50m) and 500-ms exposure time, was used to capture the DAPI
607 fluorescence in fixed 1N and multi-N cells.

608 For *C. crescentus*, phase contrast and fluorescence imaging were performed on a Nikon Ti-E
609 microscope equipped with a Perfect Focus System, a 100x Plan Apo λ 1.45 NA oil immersion objective,
610 a motorized stage, an Orca-Flash4.0 V2 142 CMOS camera (Hamamatsu) at room temperature.
611 Chroma filter sets were used to acquire fluorescence images: CFP (excitation ET436/20x, dichroic
612 T455lp, emission ET480/40m) and mCherry (excitation ET560/40x, dichroic T585lpxr, emission
613 ET630/75m). The microscope was controlled using NIS-Elements AR. For time-lapse imaging, phase
614 images were collected every 2.5 min.
615
616 **Photoactivated localization microscopy**
617 For single-molecule photoactivated localization (PALM) microscopy, coverslips were plasma-cleaned
618 of background fluorescent particles using a plasma cleaner (PDC-32G, Harrick Plasma). Live cell PALM
619 microscopy was performed on a Nikon N-STORM microscope equipped with a Perfect Focus System
620 and a motorized stage. JF549 fluorescence was measured using an iXon3 DU 897 EMCCD camera
621 (Andor) and excited from a 50 mW 561 nm laser (MLC400B laser unit, Agilent) with 50% transmission.
622 The laser was focused through a 100x Apo TIRF 1.49 NA oil immersion objective (Nikon) onto the
623 sample using an angle for highly inclined thin illumination to reduce background fluorescence
624 (Tokunaga et al., 2008). Fluorescence emission was filtered by a C-N Storm 405/488/561/647 laser
625 quad set. Transmission illumination was used to gather brightfield images. PALM movies of 20,000
626 frames were acquired with continuous laser illumination and a camera frame rate of 10.7 ms.
627
628
629

630 **SYTO RNASelect staining experiments**

631 In order to compare the mRNA concentration between 1N and multi-N cells, exponentially growing
632 CJW7576 (CRISPRi *ftsZ*) and CJW7457 (CRISPRi *oriC*) cells were stained with the fluorogenic SYTO
633 RNASelect dye (Invitrogen™, S7576) after CRISPRi induction with 0.2% L-arabinose. To ensure
634 overlapping cell area distributions in the absence of cell division, considering the measured growth
635 rate differences between the 1N and multi-N cells, CRISPRi *oriC* was induced for 3.5 to 4 h whereas
636 CRISPRi *ftsZ* was induced for 1.5 to 2 h. Then, the two populations were mixed at equal optical
637 densities (OD_{600}) and stained with 0.5 µM SYTO RNASelect for 15 min at 37°C with shaking. For each
638 staining, a fresh 5µM SYTO RNASelect stock was prepared in L-arabinose-containing medium. Stained
639 cells (~0.5 µL) were spotted on a 1% agarose pad prepared with the same growth medium with L-
640 arabinose for imaging. Five biological replicates were performed.

641

642 **RpoC-HaloTag-JF549 staining experiments for epifluorescence snapshots**

643 For Figure 4 – supplement 5, CRISPRi *oriC* in CJW7520 cells was induced for 3.5 h whereas CRISPRi *ftsZ*
644 (CJW7527) was induced for 1.5 h with 0.2% L-arabinose to obtain a similar range of cell sizes for
645 imaging. Then the two populations were mixed at equal optical densities (OD_{600}) and stained with 2.5
646 µM JF549 at 37°C for 30 min with shaking. The mixed cells were then washed three times with L-
647 arabinose-containing (0.2%) medium. All washes were performed at 4°C, using ice-cold medium to
648 block cell growth and avoid dilution of the dye. Then, the cells (~0.5 µL) were spotted on a 1% agarose
649 pad prepared with the same L-arabinose-containing growth medium for imaging. Two biological
650 replicates were performed.

651

652 **Fluorescence *in situ* hybridization experiments**

653 FISH with the EUB338 DNA probe (Amann et al., 1990) was used to compare the concentration of 16S
654 rRNAs in fixed *E. coli* 1N (SJ_XTL676) versus multi-N (SJ_XTL229) cells, or between fast (M9glyCAAT)
655 and slow (M9gly) growing wildtype MG1655 populations. Similar to the SYTO RNASelect experiments,
656 CRISPRi *oriC* was induced for 3.5 to 4 h whereas CRISPRi *ftsZ* was induced for 1.5 to 2 h to ensure
657 overlapping cell area distributions between 1N and multi-N cells considering the measured growth
658 rate differences between the two strains. Then, the two populations were mixed at equal optical
659 densities (OD_{600}) and fixed prior to staining using previously described protocols (Kim et al., 2019; Kim
660 and Jacobs-Wagner, 2018; Kim and Vaidya, 2020). Note that wildtype cells growing exponentially in
661 different media (M9gly or M9glyCAAT) were fixed and stained separately (separate tubes and
662 coverslips but using the exact same washing, pre-hybridization and hybridization buffers).

663 Pre-hybridization was performed for 2 h at 37°C using a solution that contained 40%
664 formamide, 2x saline-sodium citrate (SSC), 1x vanadyl ribonucleoside complex (VRC) and 0.4% (w/v)
665 bovine serum albumin (BSA). Staining was performed for 13 h at 37°C using a solution that contained
666 500nM EUB338-Cy3 Eubacterial probe (Millipore Sigma, MBD0033), 40% formamide, 2x SSC, 1x VRC,
667 0.4% (w/v) BSA, 0.4mg/mL *E. coli* tRNA, and 10% dextran sulfate. The high probe concentration
668 allowed for the saturation of the 16S rRNA as previously shown (Hoshino et al., 2008), which made it
669 possible to compare rRNA concentrations between different strains and media. After staining, the
670 fixed cells were washed five times with a wash solution (50% formamide, 2X SSC) and ten times with
671 1X phosphate-buffered saline (PBS). Right before mounting the coverslip on the glass slide for imaging,
672 the 1N/multi-N cells were further stained with 1 µg/mL DAPI.

673

674 **Image processing and data analysis**

675 Data analysis was done in MATLAB (Mathworks) (MAIN_pop_analysis.m script for epifluorescence
676 snapshots, MAIN_timelapse.m script for timelapse movies, and MAIN_mol_tracking.m script for
677 single-molecule tracking experiments), except for segmentation of phase contrast images, which was
678 done in Python (segmentationRun.py) using a convolutional neural network, the Nested-Unet (Wiktor
679 et al., 2021; Zhou et al., 2020), and the analysis of the SYTO RNASelect and RpoC-HaloTag-JF549
680 epifluorescence (snapshots_analysis_UNET_version_ND2.py class) that was also performed in Python
681 3.9 (DNA_limitation_python_environment.yml). The Nested-Unet network was trained for our
682 microscopy setup using PyTorch 1.7.0 and NumPY 1.19.2 (trainerWrapper.py) (Harris et al., 2020;
683 Paszke et al., 2019).

684 Cell area masks from segmentation were linked between time-lapse frames based on
685 maximum overlap (trackCells.m). Two masks linked to the same cell area were considered a cell
686 division event. To estimate the absolute growth rate, the cell area over time was smoothed by a
687 sliding-average window of five data points (time interval 5 min) and the difference in the cell area
688 between consecutive frames was calculated. The relative growth rate was calculated by dividing the
689 absolute growth rate by the cell area. Cell areas were converted into volumes using Oufti's scripts
690 (Paintdakhi et al., 2016). To avoid bias from cells reaching sizes too large to support growth, the time-
691 lapse data for filamenting cells was truncated based on their maximum absolute growth rate.

692 Fluorescent ParB-mCherry spots were detected by fitting a 2D Gaussian function to raw image
693 data (detectSpots.m). First, the fluorescent image was filtered using a bandpass filter to identify the
694 local maxima. Next, the local maxima were fitted by a Gaussian function and a spot quality score was
695 calculated based on spot intensity and quality of a Gaussian fit ($Intensity \cdot quality_{fit} = \sigma_{fit}$). The

696 spot score threshold was determined by visual inspection of the training data and was set to remove
697 poor-quality spots from analysis.

698 The number of HU-mCherry-labeled nucleoid areas was determined using Otsu's thresholding
699 (multithresh.m) (Otsu, 1979). Minimum and maximum area thresholds for an individual nucleoid were
700 determined by measuring the number of fluorescent spots of ParB protein fusion in HU-labeled
701 nucleoid areas of a strain (CJW7517) carrying a *parS* site from plasmid pMT1 at *ori1* (Figure 1 –
702 supplement 3A). Only cells containing a single nucleoid were considered 1N cells. To measure the
703 total fluorescence intensity of a cell, the median intensity of the area outside the cell areas was
704 subtracted from the fluorescence intensity of each pixel of a cell, and the intensity of all pixels was
705 summed together.

706 For the SYTO RNASelect, RpoC-HaloTag-JF549, and EUB338 epifluorescence snapshot
707 experiments (Figure 4 and Figure 4 – supplements 1 and 2), the nucleoid objects were segmented
708 using the *segment_nucleoids* function in the *snapshots_analysis_UNET_version_ND2.py* class. This
709 function combines a Laplacian of Gaussian (LoG) filter, an adaptive filter, and a hard threshold to
710 detect the nucleoid boundaries and distinguish between 1N and multi-N cells in the mixed populations.
711 The image filters were applied using the scikit-image (Van Der Walt et al., 2014) and NumPy Python
712 libraries. For the SYTO RNASelect-stained cells, the HU-mCherry fluorescence was used to segment
713 the nucleoid objects. In the EUB338 FISH experiments, the nucleoids were stained with DAPI. For the
714 RpoC-HaloTag-JF549-stained cells, the fluorescence of RpoC-HaloTag-JF549 bound to nucleoids was
715 used to segment the nucleoid objects. The number of segmented nucleoid objects was used to
716 distinguish between 1N (one nucleoid object) and multi-N (two or more nucleoid objects) cells. The
717 classification results were curated manually by visual inspection.

718 The SYTO RNASelect concentration corresponds to the total fluorescence of the fluorogenic
719 dye within the cell boundaries of the cell mask, divided by the area of the cell mask. Similarly, the
720 RpoC-HaloTag-JF549 and EUB338 concentrations were calculated in arbitrary units.

721 To ensure that the SYTO RNASelect, the RpoC-HaloTag-JF549, or the EUB338-Cy3 fluorescence
722 was compared for the same distributions of cell areas between the 1N and multi-N cells in the mixed
723 populations, random sampling was performed in each cell area bin using a sample size equal to the
724 smaller cell number between the 1N and multi-N cells (Figure 4 – supplements 1 and 2B). For example,
725 if in each cell area bin, there were 100 1N cells and 500 multi-N cells, 100 cells were randomly sampled
726 from the multi-N population to match the sample size of the 1N population. Bins with less than 25
727 (for the EUB338 experiments) or 50 (for the RNASelect or the RpoC-HaloTag-JF549 experiments) cells
728 per population across biological replicates were removed from the analysis. This sampling was
729 performed one time to compare the distributions of the SYTO RNASelect, EUB338, and RpoC-HaloTag-
730 JF549 (Figure 4B-C and Figure 4 – supplement 2C-D) concentrations between the 1N and multi-N cells.
731 However, to estimate the average 1N/multi-N SYTO RNASelect, EUB338 or RpoC-HaloTag-JF549 ratio
732 during cell growth (Figure 4D and Figure 4 – supplement 2E) multiple samplings (with substitution)
733 were performed for each biological replicate and cell area bin. This allowed us to use all the data while
734 still comparing equal numbers of 1N and multi-N cells per biological replicate and cell area bin. Cell
735 area bins with less than 5 (for the EUB338 experiments) or 10 (for the RNASelect or the RpoC-HaloTag-
736 JF549 experiments) cells per biological replicate were removed from the analysis. Also here, the
737 sample size was set by the smallest population size (1N or multi-N population) and the number of
738 iterations was equal to the difference between the populations multiplied by 10.

739

740 **Single-molecule tracking analysis**

741 Single-molecule tracking data was analyzed as previously described (Mäkelä and Sherratt, 2020).
742 Candidate fluorescent spots were detected using band-pass filtering and an intensity threshold for
743 each frame of the time-lapse sequence. These initial localizations were used as starting positions in
744 phasor spot detection for high-precision localization (Martens et al., 2018). Individual molecules were
745 then tracked in each cell area by linking positions to a trajectory if they appeared in consecutive
746 frames within a distance of 0.8 µm. Cell areas were detected from bright-field images using
747 MicrobeTracker (Sliusarenko et al., 2011). In the case of multiple localizations within the tracking
748 radius, these localizations were omitted from the analysis. Tracking allowed for a single frame
749 disappearance of the molecule within a trajectory due to blinking or missed localization. The mobility
750 of each molecule was determined by calculating an apparent diffusion coefficient, D_a, from the
751 stepwise mean-squared displacement (MSD) of the trajectory using:

752 $$D_a = \frac{1}{4n\Delta t}\sum_{i=1}^{n}[x(i\Delta t) - x(i\Delta t + \Delta t)]^2 + [y(i\Delta t) - y(i\Delta t + \Delta t)]^2$$

753 where x(t) and y(t) indicate the coordinates of the molecule at time t, Δt is the frame rate of the
754 camera, and n is the total number of the steps in the trajectory. Trajectories with less than 9
755 displacements were omitted due to the higher uncertainty in D_a.

756 The calculated D_a values are expected to reflect different dynamic states of molecules. To
757 determine the fraction of molecules in each state, $\log_{10}$ transformed D_a data (Figure 2D) was fitted to
758 a Gaussian mixture model (GMM) using the expectation-maximization algorithm (Bishop, Christopher,
759 2006). A mixture of 3 Gaussian distributions with free parameters for mean, SD, and weight of each
760 state were fitted for different conditions (Figure 2D). Additionally, for 1N cells, single-molecule

761 tracking data were binned and fitted as a function of cell area (Figure 2D – supplement 3). To
762 determine the active RNAP or ribosome fraction of a single cell, the GMM was used to determine the
763 state of each molecule from the measured D_a, and the fraction of molecules in the slowest ("active")
764 state was calculated. Only cells with at least 50 trajectories were considered in the analysis for more
765 accurate quantification. The total quantity of active molecules was estimated by multiplying the
766 measured total fluorescence intensity with the measured active fraction as a function of the cell area.
767

768 **Sample preparation for liquid chromatography coupled to tandem mass spectrometry (LC-MS/MS)**

769 CRISPRi *oriC* (SJ_XTL676) cells were collected 0, 120, 180, 240, and 300 min after addition of 0.2%
770 arabinose, while CRISPRi *ftsZ* (SJ_XTL229) cells were collected after 0, 60, and 120 min of induction,
771 and pelleted. Cell pellets were lysed in 1% SDS at 95°C for 10 min (with vigorous intermittent vortexing
772 and in the presence of 5 mM β-mercaptoethanol as a reducing agent). Cell lysates were cleared by
773 centrifugation at 15000 x g for 30 min at 4°C. The lysates were alkylated with 10 mM iodoacetamide
774 for 15 min at room temperature, and then precipitated with three volumes of a solution containing
775 50% acetone and 50% ethanol. Precipitated proteins were re-solubilized in 2 M urea, 50 mM Tris-HCl,
776 pH 8.0, and 150 mM NaCl, and then digested with TPCK-treated trypsin (50:1) overnight at 37°C.
777 Trifluoroacetic acid was added to the digested peptides at a final concentration of 0.2%. Peptides
778 were desalted with a Sep-Pak 50 mg C18 column (Waters). The C18 column was conditioned with five
779 column volumes of 80% acetonitrile and 0.1% acetic acid, and then washed with five column volumes
780 of 0.1% trifluoroacetic acid. After samples were loaded, the column was washed with five column
781 volumes of 0.1% acetic acid followed by elution with four column volumes of 80% acetonitrile and
782 0.1% acetic acid. The elution was dried in a Concentrator at 45°C. Peptides (20 µg) resuspended in a

783 100-mM triethylammonium bicarbonate solution were labeled using 100 µg of Thermo TMT10plex™
784 in a reaction volume of 25 µl for 1 h. The labeling reaction was quenched with 8 µL of 5%
785 hydroxylamine for 15 min. Labeled peptides were pooled, acidified to a pH of ~2 using drops of 10%
786 trifluoroacetic acid, and desalted again with a Sep-Pak 50 mg C18 column as described above. TMT-
787 labeled peptides were pre-fractionated using a Pierce™ High pH Reversed-Phase Peptide
788 Fractionation Kit. Pre-fractionated peptides were dried using a concentrator and re-suspended in 0.1%
789 formic acid.
790
791 **LC-MS/MS data acquisition**
792 Pre-fractionated TMT-labeled peptides were analyzed on a Fusion Lumos mass spectrometer (Thermo
793 Fisher Scientific) equipped with a Thermo EASY-nLC 1200 LC system (Thermo Fisher Scientific).
794 Peptides were separated by capillary reverse phase chromatography on a 25 cm column (75 µm inner
795 diameter, packed with 1.6 µm C18 resin, AUR2-25075C18A, Ionopticks). Electrospray ionization
796 voltage was set to 1550 V. Peptides were introduced into the Fusion Lumos mass spectrometer using
797 a 180 min stepped linear gradient at a flow rate of 300 nL/min. The steps of the gradient were as
798 follows: 6–33% buffer B (0.1% (v/v) formic acid in 80% acetonitrile) for 145 min, 33-45% buffer B for
799 15 min, 40-95% buffer B for 5 min, and 90% buffer B for 5 min. Column temperature was maintained
800 at 50°C throughout the procedure. Xcalibur software (Thermo Fisher Scientific) was used for the data
801 acquisition and the instrument was operated in data-dependent mode. Advanced peak detection was
802 disabled. Survey scans were acquired in the Orbitrap mass analyzer (centroid mode) over the range
803 of 380 to 1400 m/z with a mass resolution of 120,000 (at m/z 200). For MS1 (the survey scan), the
804 normalized AGC target (%) was set at 250 and the maximum injection time was set to 100 ms. Selected

805 ions were fragmented by the Collision Induced Dissociation (CID) method with normalized collision
806 energies of 34 and the tandem mass spectra were acquired in the ion trap mass analyzer with the
807 scan rate set to “Rapid”. The isolation window was set to 0.7 m/z. For MS2 (the peptide fragmentation
808 scan), the normalized AGC target (%) and the maximum injection time were set to “standard” and 35
809 ms, respectively. Repeated sequencing of peptides was kept to a minimum by dynamic exclusion of
810 the sequenced peptides for 30 s. The maximum duty cycle length was set to 3 s. Relative changes in
811 peptide concentration were determined at the level of the MS3 (reporter ion fragmentation scan) by
812 isolating and fragmenting the five most dominant MS2 ion peaks.
813
814 **Spectral searches**
815 All raw files were searched using the Andromeda engine (Thomason, Costantino, and Court 2007)
816 embedded in MaxQuant (v2.3.1.0) (Cox and Mann, 2008). A Reporter ion MS3 search was conducted
817 using 10plex TMT isobaric labels. Variable modifications included oxidation (M) and protein N-
818 terminal acetylation. Carbamidomethylation of cysteines was a fixed modification. The number of
819 modifications per peptide was capped at five. Digestion was set to tryptic (proline-blocked). Database
820 search was conducted using the UniProt proteome Ecoli_UP000000625_83333. The minimum
821 peptide length was seven amino acids. The false discovery rate was determined using a reverse decoy
822 proteome (Elias and Gygi, 2007).
823
824 **Proteomics data analysis**
825 Normalization and protein slope calculations were performed as described previously (Lanz et al.,
826 2022). In brief, the relative signal difference between the TMT channels for each peptide was plotted

827 against the normalized cell area for each of the bins of *E. coli* cells. For protein detection, we used a
828 minimum of three unique peptide measurements per protein as a threshold. To derive the protein
829 slope values shown in Figure 5, individual peptide measurements were consolidated into a protein
830 level measurement using Python's groupby.median. Peptides with the same amino acid sequence that
831 were identified as different charge states or in different fractions were considered independent
832 measurements. We summarized the size scaling behavior of individual proteins as a slope value
833 derived from a regression. Each protein slope value was based on the behavior of all detected
834 peptides.
835

836 For a given protein, we calculated the cell size-dependent slope as follows:

837 y_i = relative signal in the ith TMT channel (median of all corresponding peptides in this channel)

838 x_i = normalized cell size in the ith TMT channel (cell area for a given timepoint / mean cell area for the
839 experiment)

840 The protein slope value was determined from a linear fit to the log-transformed data using the
841 equation:

842 $$Log_2(y) = Slope \cdot Log_2(x)$$

843 Variables were log-transformed so that a slope of 1 corresponds to an increase in protein
844 concentration that is proportional to the increase in cell volume, and a slope of -1 corresponds to
845 1/volume dilution. Pearson correlation coefficients and p values were calculated using SciPy's

846 pearsonr module in Python (Virtanen et al., 2020). The results were reproducible across the two
847 replicates (Figure 5 – figure supplement 1).

848

849 **Estimation of protein abundance using summed ion intensity**

850 MS1-level peptide ion intensities from experiment #1 were used to estimate the relative protein
851 abundance. For each protein, all peptide intensities were summed together using the "Intensity"
852 column of MaxQuant's evidence.txt file. To adjust for the fact that larger proteins produce more
853 tryptic peptides, the summed ion intensity for each protein was divided by its amino acid sequence
854 length.

855

856 **Calculation of distance from *oriC***

857 Gene coordinates were downloaded from EcoCyc database. The midpoint of each coding sequence
858 was used to determine the circular distance (in base pairs) from *oriC* (base pair 3925859 of the total
859 length of 4641652). A script was written to make three distance calculations. First, the direct distance
860 (the midpoint of each gene minus 3,925,859 bp (*oriC*)) was determined. Next, the midpoint coordinate
861 of each gene was subtracted by the total genome length (4,641,652 bp) and then subtracted again by
862 the coordinate of *oriC* (3,925,859 bp). Finally, the midpoint coordinate of each gene was added to the
863 total genome length (4,641,652 bp) and then subtracted by the coordinate of *oriC* (3,925,859 bp). The
864 absolute values of these three calculations were then taken and the minimal values represent the
865 circular distances between *oriC* and each gene.

866

867 **Sample preparation for RNA-seq experiments**

868 CRISPRi *oriC* strain (SJ_XTL676) was grown in M9glyCAAT at 37°C and cells were collected 60, 120, 200,
869 and 240 min after addition of 0.2% L-arabinose. Images of cells were acquired at each timepoint to
870 determine cell area, as described above. For each timepoint, the aliquot was spun down, the
871 supernatant was removed, and the pellet was flash-frozen. *E. coli* pellets were resuspended in ice cold
872 PBS and mixed with *C. crescentus* cells in approximately a 1-to-1 ratio based on OD_{600}. *C. crescentus*
873 cells were originally included with the intent of using them as a spike-in reference. However, the
874 fraction of final reads obtained from *C. crescentus* transcripts was inconsistent with the initial mixing
875 ratios. In addition, without knowing the exact DNA concentration in each 1N-rich cell sample, this
876 spike-in became purposeless and thus was ignored for analysis. Cells (50 µL) in PBS were mixed with
877 250 µl TRI Reagent (Zymo Research) and lysed by bead beating on a Fastprep 24 (MPbio). Cell debris
878 were pelleted (14k rpm, 2 min) and the supernatant was recovered. RNA was then extracted using
879 the direct-zol RNA microprep kit (Zymo Research). Ribosomal RNA (rRNA) was then depleted using
880 the NEBNext rRNA Depletion Kit for Bacteria (NEB, #E7850) and NEBNext Ultra II Directional RNA
881 Library Prep Kit for Illumina (NEB, #E7760) was then used to prepare libraries for paired-end (2x150bp)
882 Illumina sequencing (Novogene).

883

884 **RNA-seq data analysis**

885 A combined genome file of *E. coli* K-12 MG1655 and *C. crescentus* NA1000 with gene annotations was
886 generated using a previously described approach (Swaffer et al., 2023). Read mapping statistics and
887 genome browser tracks were generated using custom Python scripts. For quantification purposes,
888 reads were aligned as 2x50mers in transcriptome space against an index generated from the

889 combined gene annotation model using Bowtie (version 1.0.1 ; settings: -e 200 -a -X 1000) (Langmead
890 et al., 2009). Alignments were then quantified using eXpress (version 1.5.1) (Roberts and Pachter,
891 2013) as transcripts per million (TPM). TPM values were then recalculated after filtering for only *E.*
892 *coli* genes. with TPM values below 1 were then removed from analysis.

893 The RNA slope (i.e., relative transcript concentration vs. cell area) was calculated for each gene
894 as follows. TPM values were normalized to the mean of all values for that gene and then log2
895 transformed. The same normalization was applied to the cell area measurements for each condition.
896 A linear model was fitted to the normalized log2 data and the slope of the linear regression was taken
897 as the RNA slope.

898

899 **Estimation of the minimum genome dilution that limits transcription per nutrient condition**

900 The cell area at which the total active RNAPs deviates from the wildtype scaling behavior was
901 estimated to approximate the minimal genome dilution required to limit bulk transcription in cells
902 growing in different media. Deviation in scaling behavior was found to occur at ~2 μm^2 during fast
903 growth (M9glyCAAT, Figure 3H) or at ~1 μm^2 during slow growth (M9gly or M9ala, Figure 6A-B). Given
904 such deviations in scaling behavior were observed in cells with a single chromosome copy (i.e., in 1N
905 cells), the minimal limiting concentration is estimated to be, on average, 0.5 chromosome copies per
906 μm^2 in M9glyCAAT or 1 chromosome copy per μm^2 in M9gly or M9ala. Based on estimates described
907 in Appendix 1 (Appendix 1 – Table 1), the average chromosome concentration in wildtype cells is 0.85
908 chromosome copies per μm^2 for M9glyCAAT, 1.09 chromosome copies per μm^2 for M9gly, and 1.01
909 chromosome copies per μm^2 for M9ala. This suggests that the genome is already limiting or close to

910 be limiting (within a few percents) in cells growing in M9gly and M9ala while its concentration is ~40%

911 above the limiting concentration in cells growing M9glyCAAT.

912

913 **Mathematical model and simulations**

914 Phenomenological model: We developed a phenomenological model to illustrate cell growth

915 dynamics. In our models, the number of mRNAs (X) and the number of proteins (Y) in the cell are

916 described by the differential equations:

917 $$\frac{dX}{dt} = r_1 \alpha_{RNAP}(X,Y)Y - \delta X \qquad \text{(Eq.1)}$$

918 $$\frac{dY}{dt} = r_2 \alpha_{ribo}(X,Y)Y \qquad \text{(Eq. 2)}$$

919 In this model, the parameters r_1 and r_2 are coefficients defined as

920 $$r_1 = \#\text{ of mRNAs synthesized per minute} \times \frac{\#\text{ of RNAPs on mRNA synthesis}}{\#\text{ of RNAPs on total RNA synthesis}} \frac{\#\text{ of RNAPs in cell}}{\#\text{ of proteins in cell}}$$

921 $$r_2 = \#\text{ of protein synthesized per minute} \times \frac{\#\text{ of ribosomes in cell}}{\#\text{ of proteins in cell}}$$

922

923 Here, $\alpha_{RNAP}(X,Y)$ is the fraction of active RNA polymerases, $\alpha_{ribo}(X,Y)$ is the fraction of active

924 ribosomes, and δ is the mRNA degradation rate. We assumed that the protein degradation is

925 negligible because most bacterial proteins are stable (Balakrishnan et al., 2022; Lin and Amir, 2018).

926 For the fraction of active RNAPs, we considered two different models (models A and B). In model A,

927 the fraction of active RNAPs was modeled by $\alpha_{RNAP} = \frac{[Z]}{K_1+[Z]}$. In model B, where we included different

928 states of RNAP and promoter, the expression of α_{RNAP} is more complicated and is described in

929 Appendix 3. Instead of considering a type of Michaelis-Menten (MM) reaction (Klumpp and Hwa,

930 2008), model B is based on the mass action law. For both models A and B, the ribosomes were

931 modeled by $\alpha_{ribo} = \frac{[X]}{K_2+[X]}$. We used $[Z]$ and $[X]$ to represent the genome and mRNA concentrations,

932 respectively. We assumed that the cell volume (*V*) and cell area (*A*) are proportional to the protein

933 number Y, which is a good approximation (Basan et al., 2015; Kubitschek et al., 1984). While this

934 assumption has not been verified in 1N cells, the concentration of ribosomes, which constitute most

935 of the protein mass, were found to remain constant in these cells (Figure 2A). Namely, in our model,

936 $V = cY$ and $A = c'Y$ with constants c, c'. Under balanced growth conditions, $[Z]$ was assumed to be

937 constant. For the DNA-limited growth condition (as in 1N cells), we assumed that the genome does

938 not duplicate and is kept at a single copy per cell ($Z(t) = 1$) while the cell volume continue to increase.

939 The details for parameters used in this model are described in Table 1.

940 Numerical simulations: To simulate the model for balanced and DNA-limited growths, we first

941 fixed a parameter set based on the literature (see Tables 1 and 2) and simulated Eq. 1 and Eq. 2 to

942 reach the regime of balanced growth. Under balanced growth, we obtained the balanced growth

943 vector (X^*, Y^*) where Y^* matches the initial protein number reported in the literature (see Table 2).

944 Then, using the balanced growth vector as the initial condition, we simulated the balanced growth

945 and DNA-limited growth using different assumptions of genome content $Z(t)$ (described in the

946 previous paragraph). The simulation was performed using the MATLAB built-in function *ode23* with

947 relative and absolute errors of the numerical values to be 10^{-4} and 10^{-5}, respectively. For each growth

948 condition, we obtained growth trajectories $\big(X(t), Y(t)\big)$, and from $Y(t)$, we calculated the cell

949 volume $V(t)$ and area $A(t)$ as described above. For model A, the fraction of active RNAPs was

950 calculated by $\alpha_{RNAP} = \frac{[Z]}{K_1+[Z]}$, while for model B, it is calculated using a more complicated formula

951 that takes into account RNAP kinetics (see Appendix 3). For both models, the fraction of active
952 ribosomes was calculated as $\alpha_{ribo} = \frac{[X]}{K_2+[X]}$.

953 Parameter fitting: For either model A or B, we fitted our simulation results to all the
954 experimental data including growth curves, the fraction of active RNAPs, and the fraction of active
955 ribosomes for 1N and WT or multi-N cells (six datasets in total); see Appendix 2 for the initial
956 parameter estimation and Appendix 4 for the optimization procedure details. The optimized
957 parameter sets (see Table 2) were used for the numerical simulations shown in Figure 5. Note that
958 the optimized parameter set remained within the realistic range for cellular physiology (see Appendix
959 4 — figure 1 for comparison between original and optimized parameters).

960

961 **DATA AVAILABILITY**

962 Microscopy image analysis code is available on the Jacobs-Wagner lab github repository
963 (https://github.com/JacobsWagnerLab/published/tree/master/Makela_Papagiannakis_2024-Elife).
964 The TMT-MS and RNA-seq data analysis and processing code is available at
965 https://github.com/mikechucklanz/Proteome_size_scaling_Ecoli and
966 https://github.com/georgimarinov/GeorgiScripts.

967 For this study, the following TMT-MS and RNA-seq data were generated. Dataset 1 includes
968 the calculated protein slopes from 1N-rich and multi-N cells, the normalized protein proportions, the
969 summed ion intensities for each protein as well as the distance of its gene from the origin of
970 replication (*oriC*) and the GO-term analysis. Dataset 2 includes the calculated mRNA slopes, in
971 comparison with the average protein slopes from 1N-rich cells. Dataset 3 is an ensemble of the TMT-
972 MS data, the RNA-seq data, and published datasets of essential genes (Gerdes et al., 2003; Goodall et

973 al., 2018; Hashimoto et al., 2005) and gene expression-related data (Balakrishnan et al., 2022). All
974 sequencing data associated with this study have been deposited to the GEO repository with the
975 GSE261497 accession number. The mass spectrometry proteomics data have been deposited to the
976 ProteomeXchange Consortium via the PRIDE partner repository with the dataset identifier
977 PXD050093.
978

979 **ACKNOWLEDGMENTS**

980 We thank Drs. Brun, Jun, Marczynski, Shapiro and Weisshaar for sharing published strains. We are
981 grateful to Dr. Lavis for the gift of JF549 and Dr. Badrinarayanan for valuable discussion. We would
982 also like to thank the Jacobs-Wagner laboratory for support, discussion, and critical reading of the
983 manuscript. C.J.-W. is an investigator of the Howard Hughes Medical Institute.
984

985 **REFERENCES**

986 Aaron M, Charbon G, Lam H, Schwarz H, Vollmer W, Jacobs-Wagner C. 2007. The tubulin homologue
987 FtsZ contributes to cell elongation by guiding cell wall precursor synthesis in Caulobacter
988 crescentus. *Mol Microbiol* **64**:938–952. doi:10.1111/j.1365-2958.2007.05720.x
989 Addinall SG, Bi E, Lutkenhaus J. 1996. FtsZ ring formation in fts mutants. *J Bacteriol* **178**:3877–3884.
990 Amann RI, Binder BJ, Olson RJ, Chisholm SW, Devereux R, Stahl DA. 1990. Combination of 16S rRNA-
991 targeted oligonucleotide probes with flow cytometry for analyzing mixed microbial
992 populations. *Appl Environ Microbiol* **56**:1919–1925. doi:10.1128/aem.56.6.1919-1925.1990
993 Bakshi S, Choi H, Mondal J, Weisshaar JC. 2014. Time-dependent effects of transcription- and
994 translation-halting drugs on the spatial distributions of the *E scherichia coli* chromosome and
995 ribosomes: Time-dependent drug effects on *E. coli* chromosome spatial distribution. *Mol*
996 *Microbiol* **94**:871–887. doi:10.1111/mmi.12805
997 Bakshi S, Siryaporn A, Goulian M, Weisshaar JC. 2012. Superresolution imaging of ribosomes and
998 RNA polymerase in live Escherichia coli cells. *Mol Microbiol* **85**:21–38. doi:10.1111/j.1365-
999 2958.2012.08081.x
1000 Balakrishnan R, Mori M, Segota I, Zhang Z, Aebersold R, Ludwig C, Hwa T. 2022. Principles of gene
1001 regulation quantitatively connect DNA to RNA and proteins in bacteria. *Science*
1002 **378**:eabk2066. doi:10.1126/science.abk2066

1003 Banaz N, Mäkelä J, Uphoff S. 2019. Choosing the right label for single-molecule tracking in live
1004 bacteria: side-by-side comparison of photoactivatable fluorescent protein and Halo tag dyes.
1005 *J Phys Appl Phys* **52**:064002. doi:10.1088/1361-6463/aaf255
1006 Banerjee S, Lo K, Daddysman MK, Selewa A, Kuntz T, Dinner AR, Scherer NF. 2017. Biphasic growth
1007 dynamics control cell division in Caulobacter crescentus. *Nat Microbiol* **2**:6–11.
1008 doi:10.1038/nmicrobiol.2017.116
1009 Basan M, Zhu M, Dai X, Warren M, Sévin D, Wang Y-P, Hwa T. 2015. Inflating bacterial cells by
1010 increased protein synthesis. *Mol Syst Biol* **11**:836. doi:10.15252/msb.20156178
1011 Belliveau NM, Chure G, Hueschen CL, Garcia HG, Kondev J, Fisher DS, Theriot JA, Phillips R. 2021.
1012 Fundamental limits on the rate of bacterial growth and their influence on proteomic
1013 composition. *Cell Syst* **12**:924-944.e2. doi:10.1016/j.cels.2021.06.002
1014 Bishop, Christopher. 2006. Pattern Recognition and Machine Learning. New York, NY: Springer.
1015 Bosdriesz E, Molenaar D, Teusink B, Bruggeman FJ. 2015. How fast-growing bacteria robustly tune
1016 their ribosome concentration to approximate growth-rate maximization. *FEBS J* **282**:2029–
1017 2044. doi:10.1111/febs.13258
1018 Bremer H, Dennis P. 1996. Modulation of chemical composition and other parameters of the cell by
1019 growth rate. *Neidhardt F Ed Wash DC Am Soc Microbiol Press* 1553.
1020 Campbell EA, Korzheva N, Mustaev A, Murakami K, Nair S, Goldfarb A, Darst SA. 2001. Structural
1021 mechanism for rifampicin inhibition of bacterial rna polymerase. *Cell* **104**:901–912.
1022 doi:10.1016/s0092-8674(01)00286-0
1023 Campos M, Surovtsev IV, Kato S, Paintdakhi A, Beltran B, Ebmeier SE, Jacobs-Wagner C. 2014. A
1024 constant size extension drives bacterial cell size homeostasis. *Cell* **159**:1433–1446.
1025 doi:10.1016/j.cell.2014.11.022
1026 Carl PL. 1970. Escherichia coli mutants with temperature-sensitive synthesis of DNA. *MGG Mol Gen*
1027 *Genet* **109**:107–122. doi:10.1007/BF00269647
1028 Cherepanov PP, Wackernagel W. 1995. Gene disruption in Escherichia coli: TcR and KmR cassettes
1029 with the option of Flp-catalyzed excision of the antibiotic-resistance determinant. *Gene*
1030 **158**:9–14. doi:10.1016/0378-1119(95)00193-A
1031 Churchward G, Bremer H, Young R. 1982. Transcription in bacteria at different DNA concentrations. *J*
1032 *Bacteriol* **150**:572–581. doi:10.1128/jb.150.2.572-581.1982
1033 Crozier L, Foy R, Adib R, Kar A, Holt JA, Pareri AU, Valverde JM, Rivera R, Weston WA, Wilson R,
1034 Regnault C, Whitfield P, Badonyi M, Bennett LG, Vernon EG, Gamble A, Marsh JA, Staples CJ,
1035 Saurin AT, Barr AR, Ly T. 2023. CDK4/6 inhibitor-mediated cell overgrowth triggers osmotic
1036 and replication stress to promote senescence. *Mol Cell* **83**:4062-4077.e5.
1037 doi:10.1016/j.molcel.2023.10.016
1038 Datsenko KA, Wanner BL. 2000. One-step inactivation of chromosomal genes in Escherichia coli K-12
1039 using PCR products. *Proc Natl Acad Sci* **97**:6640–6645. doi:10.1073/pnas.120163297
1040 Donachie W. 1968. Relationship between cell size and time of initiation of DNA replication. *Nature*
1041 **219**:1077–1079. doi:10.1038/2191077a0
1042 Ecker RE, Schaechter M. 1963. Ribosome content and the rate of growth of Salmonella
1043 typhimurium. *BBA - Biochim Biophys Acta* **76**:275–279. doi:10.1016/0006-3002(63)90040-4
1044 Elias JE, Gygi SP. 2007. Target-decoy search strategy for increased confidence in large-scale protein
1045 identifications by mass spectrometry. *Nat Methods* **4**:207–214. doi:10.1038/nmeth1019

1046 Elowitz MB, Surette MG, Wolf P-E, Stock JB, Leibler S. 1999. Protein Mobility in the Cytoplasm of
1047 Escherichia coli. *J Bacteriol* **181**:197–203. doi:10.1128/JB.181.1.197-203.1999
1048 Ely B. 1991. [17] Genetics of Caulobacter crescentus. *Methods Enzymol* **204**:372–384.
1049 doi:10.1016/0076-6879(91)04019-K
1050 Forchhammer J, Lindahl L. 1971. Growth rate of polypeptide chains as a function of the cell growth
1051 rate in a mutant of Escherichia coli 15. *J Mol Biol* **55**:563–568. doi:10.1016/0022-
1052 2836(71)90337-8
1053 Fossum S, Crooke E, Skarstad K. 2007. Organization of sister origins and replisomes during multifork
1054 DNA replication in Escherichia coli. *EMBO J* **26**:4514–4522. doi:10.1038/sj.emboj.7601871
1055 Foy R, Crozier L, Pareri AU, Valverde JM, Park BH, Ly T, Saurin AT. 2023. Oncogenic signals prime
1056 cancer cells for toxic cell overgrowth during a G1 cell cycle arrest. *Mol Cell* **83**:4047-4061.e6.
1057 doi:10.1016/j.molcel.2023.10.020
1058 Frandi A, Collier J. 2019. Multilayered control of chromosome replication in Caulobacter crescentus.
1059 *Biochem Soc Trans* **47**:187–196. doi:10.1042/BST20180460
1060 Gerdes SY, Scholle MD, Campbell JW, Balázsi G, Ravasz E, Daugherty MD, Somera AL, Kyrpides NC,
1061 Anderson I, Gelfand MS, Bhattacharya A, Kapatral V, D'Souza M, Baev MV, Grechkin Y,
1062 Mseeh F, Fonstein MY, Overbeek R, Barabási A-L, Oltvai ZN, Osterman AL. 2003.
1063 Experimental Determination and System Level Analysis of Essential Genes in *Escherichia coli*
1064 MG1655. *J Bacteriol* **185**:5673–5684. doi:10.1128/JB.185.19.5673-5684.2003
1065 Ginzberg MB, Kafri R, Kirschner M. 2015. On being the right (cell) size. *Science* **348**:1245075.
1066 doi:10.1126/science.1245075
1067 Goodall ECA, Robinson A, Johnston IG, Jabbari S, Turner KA, Cunningham AF, Lund PA, Cole JA,
1068 Henderson IR. 2018. The Essential Genome of *Escherichia coli* K-12. *mBio* **9**:e02096-17.
1069 doi:10.1128/mBio.02096-17
1070 Gorbatyuk B, Marczynski GT. 2001. Physiological consequences of blocked Caulobacter crescentus
1071 dnaA expression, an essential DNA replication gene. *Mol Microbiol* **40**:485–497.
1072 doi:10.1046/j.1365-2958.2001.02404.x
1073 Govers SK, Campos M, Tyagi B, Laloux G, Jacobs-Wagner C. 2024. Apparent simplicity and emergent
1074 robustness in the control of the *Escherichia coli* cell cycle. *Cell Syst* **15**:19-36.e5.
1075 doi:10.1016/j.cels.2023.12.001
1076 Gray WT, Govers SK, Xiang Y, Parry BR, Campos M, Kim S, Jacobs-Wagner C. 2019. Nucleoid Size
1077 Scaling and Intracellular Organization of Translation across Bacteria. *Cell* **177**:1632-1648.e20.
1078 doi:10.1016/J.CELL.2019.05.017
1079 Grimm JB, English BP, Chen J, Slaughter JP, Zhang Z, Revyakin A, Patel R, Macklin JJ, Normanno D,
1080 Singer RH, Lionnet T, Lavis LD. 2015. A general method to improve fluorophores for live-cell
1081 and single-molecule microscopy. *Nat Methods* **12**:244–250. doi:10.1038/nmeth.3256
1082 Guyer MS, Reed RR, Steitz JA, Low KB. 1981. Identification of a Sex-factor-affinity Site in E. coli as γδ.
1083 *Cold Spring Harb Symp Quant Biol* **45**:135–140. doi:10.1101/SQB.1981.045.01.022
1084 Hamouche L, Poljak L, Carpousis AJ. 2021. Ribosomal RNA degradation induced by the bacterial RNA
1085 polymerase inhibitor rifampicin. *RNA* **27**:946–958. doi:10.1261/rna.078776.121
1086 Harris CR, Millman KJ, van der Walt SJ, Gommers R, Virtanen P, Cournapeau D, Wieser E, Taylor J,
1087 Berg S, Smith NJ, Kern R, Picus M, Hoyer S, van Kerkwijk MH, Brett M, Haldane A, Del Río JF,
1088 Wiebe M, Peterson P, Gérard-Marchant P, Sheppard K, Reddy T, Weckesser W, Abbasi H,

1089 Gohlke C, Oliphant TE. 2020. Array programming with NumPy. *Nature* **585**:357–362.
1090 doi:10.1038/s41586-020-2649-2
1091 Hashimoto M, Ichimura T, Mizoguchi H, Tanaka K, Fujimitsu K, Keyamura K, Ote T, Yamakawa T,
1092 Yamazaki Y, Mori H, Katayama T, Kato J. 2005. Cell size and nucleoid organization of
1093 engineered *Escherichia coli* cells with a reduced genome. *Mol Microbiol* **55**:137–149.
1094 doi:10.1111/j.1365-2958.2004.04386.x
1095 Heinrich K, Leslie DJ, Morlock M, Bertilsson S, Jonas K. 2019. Molecular Basis and Ecological
1096 Relevance of Caulobacter Cell Filamentation in Freshwater Habitats. *mBio* **10**:e01557-19.
1097 doi:10.1128/mBio.01557-19
1098 Hoshino T, Yilmaz LS, Noguera DR, Daims H, Wagner M. 2008. Quantification of Target Molecules
1099 Needed To Detect Microorganisms by Fluorescence In Situ Hybridization (FISH) and Catalyzed
1100 Reporter Deposition-FISH. *Appl Environ Microbiol* **74**:5068–5077. doi:10.1128/AEM.00208-08
1101 Kar P, Tiruvadi-Krishnan S, Männik Jaana, Männik Jaan, Amir A. 2021. Distinguishing different modes
1102 of growth using single-cell data. *eLife* **10**:1–34. doi:10.7554/elife.72565
1103 Kim S, Beltran B, Irnov I, Jacobs-Wagner C. 2019. Long-Distance Cooperative and Antagonistic RNA
1104 Polymerase Dynamics via DNA Supercoiling. *Cell* **179**:106-119.e16.
1105 doi:10.1016/j.cell.2019.08.033
1106 Kim S, Jacobs-Wagner C. 2018. Effects of mRNA Degradation and Site-Specific Transcriptional
1107 Pausing on Protein Expression Noise. *Biophys J* **114**:1718–1729.
1108 doi:10.1016/j.bpj.2018.02.010
1109 Kim S, Vaidya K. 2020. Probing mRNA Kinetics in Space and Time in Escherichia coli using Two-Color
1110 Single-Molecule Fluorescence In Situ Hybridization. *J Vis Exp* 61520. doi:10.3791/61520-v
1111 Klumpp S, Hwa T. 2008. Growth-rate-dependent partitioning of RNA polymerases in bacteria. *Proc*
1112 *Natl Acad Sci* **105**:20245–20250. doi:10.1073/pnas.0804953105
1113 Koch AL. 1988. Why can't a cell grow infinitely fast? *Can J Microbiol* **34**:421–426. doi:10.1139/m88-
1114 074
1115 Kubitschek HE, Baldwin WW, Schroeter SJ, Graetzer R. 1984. Independence of buoyant cell density
1116 and growth rate in Escherichia coli. *J Bacteriol* **158**:296. doi:10.1128/jb.158.1.296-299.1984
1117 Langmead B, Trapnell C, Pop M, Salzberg SL. 2009. Ultrafast and memory-efficient alignment of
1118 short DNA sequences to the human genome. *Genome Biol* **10**:R25. doi:10.1186/gb-2009-10-
1119 3-r25
1120 Lanz MC, Zatulovskiy E, Swaffer MP, Zhang L, Ilerten I, Zhang S, You DS, Marinov G, McAlpine P, Elias
1121 JE, Skotheim JM. 2022. Increasing cell size remodels the proteome and promotes
1122 senescence. *Mol Cell* **82**:3255-3269.e8. doi:10.1016/j.molcel.2022.07.017
1123 Lanz MC, Zhang S, Swaffer MP, Ziv I, Götz LH, McCarty F, Jarosz DF, Elias JE, Skotheim JM. 2023.
1124 Genome dilution by cell growth drives starvation-like proteome remodeling in mammalian
1125 and yeast cells. doi:10.1101/2023.10.16.562558
1126 Lasker K, Mann TH, Shapiro L. 2016. An intracellular compass spatially coordinates cell cycle
1127 modules in *Caulobacter crescentus*. *Curr Opin Microbiol*, Antimicrobials Microbial systems
1128 biology **33**:131–139. doi:10.1016/j.mib.2016.06.007
1129 Li X, Jun Y, Erickstad MJ, Brown SD, Parks A, Court DL, Jun S. 2016. tCRISPRi: tunable and reversible,
1130 one-step control of gene expression. *Sci Rep* **6**:39076. doi:10.1038/srep39076

1131 Lilleorg S, Reier K, Pulk A, Liiv A, Tammsalu T, Peil L, Cate JHD, Remme J. 2019. Bacterial ribosome
1132 heterogeneity: Changes in ribosomal protein composition during transition into stationary
1133 growth phase. *Biochimie* **156**:169–180. doi:10.1016/j.biochi.2018.10.013
1134 Lin J, Amir A. 2018. Homeostasis of protein and mRNA concentrations in growing cells. *Nat Commun*
1135 **9**:4496. doi:10.1038/s41467-018-06714-z
1136 Lin W-H, Jacobs-Wagner C. 2022. Connecting single-cell ATP dynamics to overflow metabolism, cell
1137 growth, and the cell cycle in Escherichia coli. *Curr Biol* **32**:3911-3924.e4.
1138 doi:10.1016/j.cub.2022.07.035
1139 Mäkelä J, Sherratt DJ. 2020. Organization of the Escherichia coli Chromosome by a MukBEF Axial
1140 Core. *Mol Cell* **78**:250-260.e5. doi:10.1016/j.molcel.2020.02.003
1141 Manohar S, Estrada ME, Uliana F, Vuina K, Alvarez PM, de Bruin RAM, Neurohr GE. 2023. Genome
1142 homeostasis defects drive enlarged cells into senescence. *Mol Cell* **83**:4032-4046.e6.
1143 doi:10.1016/j.molcel.2023.10.018
1144 Martens KJA, Bader AN, Baas S, Rieger B, Hohlbein J. 2018. Phasor based single-molecule localization
1145 microscopy in 3D (pSMLM-3D): An algorithm for MHz localization rates using standard CPUs.
1146 *J Chem Phys* **148**:123311. doi:10.1063/1.5005899
1147 Mohapatra S, Weisshaar JC. 2018. Functional mapping of the E. coli translational machinery using
1148 single-molecule tracking. *Mol Microbiol* **110**:262–282. doi:10.1111/mmi.14103
1149 Neidhardt FC, Ingraham JL, Schaechter M. 1990. Physiology of the Bacterial Cell: A Molecular
1150 Approach. Sunderland, Mass: Sinauer Associates Inc.
1151 Neurohr GE, Terry RL, Lengefeld J, Bonney M, Brittingham GP, Moretto F, Miettinen TP, Vaites LP,
1152 Soares LM, Paulo JA, Harper JW, Buratowski S, Manalis S, van Werven FJ, Holt LJ, Amon A.
1153 2019. Excessive Cell Growth Causes Cytoplasm Dilution And Contributes to Senescence. *Cell*
1154 **176**:1083-1097.e18. doi:10.1016/J.CELL.2019.01.018
1155 Nielsen HJ, Ottesen JR, Youngren B, Austin SJ, Hansen FG. 2006. The Escherichia coli chromosome is
1156 organized with the left and right chromosome arms in separate cell halves. *Mol Microbiol*
1157 **62**:331–338. doi:10.1111/j.1365-2958.2006.05346.x
1158 Nordholt N, van Heerden JH, Bruggeman FJ. 2020. Biphasic Cell-Size and Growth-Rate Homeostasis
1159 by Single Bacillus subtilis Cells. *Curr Biol* **30**:2238-2247.e5. doi:10.1016/j.cub.2020.04.030
1160 Otsu N. 1979. A threshold selection method from gray-level histograms. *IEEE Trans Sys Man Cyber*
1161 **9**:62–66. doi:10.1109/TSMC.1979.4310076
1162 Paintdakhi A, Parry B, Campos M, Irnov I, Elf J, Surovtsev I, Jacobs-Wagner C. 2016. Oufti: an
1163 integrated software package for high-accuracy, high-throughput quantitative microscopy
1164 analysis. *Mol Microbiol* **99**:767–777. doi:10.1111/mmi.13264
1165 Paszke A, Gross S, Massa F, Lerer A, Bradbury J, Chanan G, Killeen T, Lin Z, Gimelshein N, Antiga L,
1166 Desmaison A, Köpf A, Yang E, DeVito Z, Raison M, Tejani A, Chilamkurthy S, Steiner B, Fang L,
1167 Bai J, Chintala S. 2019. PyTorch: An Imperative Style, High-Performance Deep Learning
1168 Library. *arXiv*, Advances in Neural Information Processing Systems 32 1912.01703.
1169 doi:10.48550/arXiv.1912.01703
1170 Reshes G, Vanounou S, Fishov I, Feingold M. 2008. Cell Shape Dynamics in Escherichia coli. *Biophys J*
1171 **94**:251–264. doi:10.1529/biophysj.107.104398
1172 Roberts A, Pachter L. 2013. Streaming fragment assignment for real-time analysis of sequencing
1173 experiments. *Nat Methods* **10**:71–73. doi:10.1038/nmeth.2251

1174 Sanamrad A, Persson F, Lundius EG, Fange D, Gynnå AH, Elf J. 2014. Single-particle tracking reveals
1175 that free ribosomal subunits are not excluded from the Escherichia coli nucleoid. *Proc Natl*
1176 *Acad Sci* **111**:11413–11418. doi:10.1073/pnas.1411558111
1177 Sauls JT, Cox SE, Do Q, Castillo V, Ghulam-Jelani Z, Jun S. 2019. Control of Bacillus subtilis Replication
1178 Initiation during Physiological Transitions and Perturbations. *mBio* **10**:e02205-19.
1179 doi:10.1128/mBio.02205-19
1180 Schaechter M, Maaloe O, Kjeldgaard NO. 1958. Dependency on Medium and Temperature of Cell
1181 Size and Chemical Composition during Balanced Growth of Salmonella typhimurium. *J Gen*
1182 *Microbiol* **19**:592–606. doi:10.1099/00221287-19-3-592
1183 Schaechter M, Williamson JP, Hood JR, Koch AL. 1962. Growth, Cell and Nuclear Divisions in some
1184 Bacteria. *Microbiology* **29**:421–434. doi:10.1099/00221287-29-3-421
1185 Scott M, Gunderson CW, Mateescu EM, Zhang Z, Hwa T. 2010. Interdependence of Cell Growth and
1186 Gene Expression: Origins and Consequences. *Science* **330**:1099–1102.
1187 doi:10.1126/science.1192588
1188 Scott M, Klumpp S, Mateescu EM, Hwa T. 2014. Emergence of robust growth laws from optimal
1189 regulation of ribosome synthesis. *Mol Syst Biol* **10**:747. doi:10.15252/msb.20145379
1190 Si F, Le Treut G, Sauls JT, Vadia S, Levin PA, Jun S. 2019. Mechanistic Origin of Cell-Size Control and
1191 Homeostasis in Bacteria. *Curr Biol* **29**:1760-1770.e7. doi:10.1016/j.cub.2019.04.062
1192 Si F, Li D, Cox SE, Sauls JT, Azizi O, Sou C, Schwartz AB, Erickstad MJ, Jun Y, Li X, Jun S. 2017.
1193 Invariance of Initiation Mass and Predictability of Cell Size in Escherichia coli. *Curr Biol*
1194 **27**:1278–1287. doi:10.1016/j.cub.2017.03.022
1195 Siegal-Gaskins D, Crosson S. 2008. Tightly Regulated and Heritable Division Control in Single
1196 Bacterial Cells. *Biophys J* **95**:2063–2072. doi:10.1529/BIOPHYSJ.108.128785
1197 Sliusarenko O, Heinritz J, Emonet T, Jacobs-Wagner C. 2011. High-throughput, subpixel precision
1198 analysis of bacterial morphogenesis and intracellular spatio-temporal dynamics. *Mol*
1199 *Microbiol* **80**:612–627. doi:10.1111/j.1365-2958.2011.07579.x
1200 Swaffer MP, Marinov GK, Zheng H, Fuentes Valenzuela L, Tsui CY, Jones AW, Greenwood J, Kundaje
1201 A, Greenleaf WJ, Reyes-Lamothe R, Skotheim JM. 2023. RNA polymerase II dynamics and
1202 mRNA stability feedback scale mRNA amounts with cell size. *Cell* **186**:5254-5268.e26.
1203 doi:10.1016/j.cell.2023.10.012
1204 Taheri-Araghi S, Bradde S, Sauls JT, Hill NS, Levin PA, Paulsson J, Vergassola M, Jun S. 2015. Cell-Size
1205 Control and Homeostasis in Bacteria. *Curr Biol* **25**:385–391. doi:10.1016/j.cub.2014.12.009
1206 Takacs CN, Kloos ZA, Scott M, Rosa PA, Jacobs-Wagner C. 2018. Fluorescent Proteins, Promoters,
1207 and Selectable Markers for Applications in the Lyme Disease Spirochete Borrelia burgdorferi.
1208 *Appl Environ Microbiol* **84**:e01824-18. doi:10.1128/AEM.01824-18
1209 Takacs CN, Wachter J, Xiang Y, Ren Z, Karaboja X, Scott M, Stoner MR, Irnov I, Jannetty N, Rosa PA,
1210 Wang X, Jacobs-Wagner C. 2022. Polyploidy, regular patterning of genome copies, and
1211 unusual control of DNA partitioning in the Lyme disease spirochete. *Nat Commun* **13**:7173.
1212 doi:10.1038/s41467-022-34876-4
1213 Terrana B, Newton A. 1975. Pattern of unequal cell division and development in Caulobacter
1214 crescentus. *Dev Biol* **44**:380–385. doi:10.1016/0012-1606(75)90409-1
1215 Thanbichler M, Iniesta AA, Shapiro L. 2007. A comprehensive set of plasmids for vanillate- and
1216 xylose-inducible gene expression in Caulobacter crescentus. *Nucleic Acids Res* **35**:e137.
1217 doi:10.1093/nar/gkm818

1218 Thanbichler M, Shapiro L. 2006. MipZ, a Spatial Regulator Coordinating Chromosome Segregation
1219 with Cell Division in Caulobacter. *Cell* **126**:147–162. doi:10.1016/j.cell.2006.05.038
1220 Thomason LC, Costantino N, Court DL. 2007. E. coli Genome Manipulation by P1 Transduction. *Curr*
1221 *Protoc Mol Biol* **79**:1.17.1-1.17.8. doi:10.1002/0471142727.mb0117s79
1222 Tokunaga M, Imamoto N, Sakata-Sogawa K. 2008. Highly inclined thin illumination enables clear
1223 single-molecule imaging in cells. *Nat Methods* **5**:159–161. doi:10.1038/nmeth1171
1224 Turner JJ, Ewald JC, Skotheim JM. 2012. Cell size control in yeast. *Curr Biol* **22**:R350–R359.
1225 doi:10.1016/j.cub.2012.02.041
1226 Van Der Walt S, Schönberger JL, Nunez-Iglesias J, Boulogne F, Warner JD, Yager N, Gouillart E, Yu T.
1227 2014. scikit-image: image processing in Python. *PeerJ* **2**:e453. doi:10.7717/peerj.453
1228 Virtanen P, Gommers R, Oliphant TE, Haberland M, Reddy T, Cournapeau D, Burovski E, Peterson P,
1229 Weckesser W, Bright J, van der Walt SJ, Brett M, Wilson J, Millman KJ, Mayorov N, Nelson
1230 ARJ, Jones E, Kern R, Larson E, Carey CJ, Polat İ, Feng Y, Moore EW, VanderPlas J, Laxalde D,
1231 Perktold J, Cimrman R, Henriksen I, Quintero EA, Harris CR, Archibald AM, Ribeiro AH,
1232 Pedregosa F, van Mulbregt P. 2020. SciPy 1.0: fundamental algorithms for scientific
1233 computing in Python. *Nat Methods* **17**:261–272. doi:10.1038/s41592-019-0686-2
1234 Wang P, Robert L, Pelletier J, Dang WL, Taddei F, Wright A, Jun S. 2010. Robust Growth of
1235 Escherichia coli. *Curr Biol* **20**:1099–1103. doi:10.1016/j.cub.2010.04.045
1236 Wang Y, Jones BD, Brun YV. 2001. A set of ftsZ mutants blocked at different stages of cell division in
1237 Caulobacter. *Mol Microbiol* **40**:347–360. doi:10.1046/j.1365-2958.2001.02395.x
1238 West L, Yang D, Stephens C. 2002. Use of the Caulobacter crescentus Genome Sequence To Develop
1239 a Method for Systematic Genetic Mapping. *J Bacteriol* **184**:2155–2166.
1240 doi:10.1128/JB.184.8.2155-2166.2002
1241 Wiktor J, Gynnå AH, Leroy P, Larsson J, Coceano G, Testa I, Elf J. 2021. RecA finds homologous DNA
1242 by reduced dimensionality search. *Nature* **597**:426–429. doi:10.1038/s41586-021-03877-6
1243 Wilson GA, Vuina K, Sava G, Huard C, Meneguello L, Coulombe-Huntington J, Bertomeu T, Maizels
1244 RJ, Lauring J, Kriston-Vizi J, Tyers M, Ali S, Bertoli C, de Bruin RAM. 2023. Active growth
1245 signaling promotes senescence and cancer cell sensitivity to CDK7 inhibition. *Mol Cell*
1246 **83**:4078-4092.e6. doi:10.1016/j.molcel.2023.10.017
1247 Withers HL, Bernander R. 1998. Characterization of dnaC2 and dnaC28 mutants by flow cytometry. *J*
1248 *Bacteriol* **180**:1624–1631. doi:10.1128/jb.180.7.1624-1631.1998
1249 Witz G, van Nimwegen E, Julou T. 2019. Initiation of chromosome replication controls both division
1250 and replication cycles in E. coli through a double-adder mechanism. *eLife* **8**:e48063.
1251 doi:10.7554/eLife.48063
1252 Wu Y, Liu Y, Lu C, Lei S, Li J, Du G. 2020. Quantitation of RNA by a fluorometric method using the
1253 SYTO RNASelect stain. *Anal Biochem* **606**:113857. doi:10.1016/j.ab.2020.113857
1254 Xiao H, Kalman M, Ikehara K, Zemel S, Glaser G, Cashel M. 1991. Residual guanosine 3‘,5‘-
1255 bispyrophosphate synthetic activity of relA null mutants can be eliminated by spoT null
1256 mutations. *J Biol Chem* **266**:5980–5990. doi:10.1016/S0021-9258(19)67694-5
1257 Yamazaki Y, Niki H, Kato J. 2008. Profiling of Escherichia coli Chromosome Database In: Osterman AL,
1258 Gerdes SY, editors. Microbial Gene Essentiality: Protocols and Bioinformatics, Methods in
1259 Molecular Biology™. Totowa, NJ: Humana Press. pp. 385–389. doi:10.1007/978-1-59745-
1260 321-9_26

1261 Zheng H, Ho P-Y, Jiang M, Tang B, Liu W, Li D, Yu X, Kleckner NE, Amir A, Liu C. 2016. Interrogating
1262 the Escherichia coli cell cycle by cell dimension perturbations. *Proc Natl Acad Sci* **113**:15000–
1263 15005. doi:10.1073/pnas.1617932114
1264 Zhou Z, Siddiquee MMR, Tajbakhsh N, Liang J. 2020. UNet++: Redesigning Skip Connections to
1265 Exploit Multiscale Features in Image Segmentation. *IEEE Trans Med Imaging* **39**:1856–1867.
1266 doi:10.1109/TMI.2019.2959609
1267 Zhurinsky J, Leonhard K, Watt S, Marguerat S, Bähler J, Nurse P. 2010. A Coordinated Global Control
1268 over Cellular Transcription. *Curr Biol* **20**:2010–2015. doi:10.1016/j.cub.2010.10.002
1269

1270

1271 **FIGURE LEGENDS**

1272 **Figure 1. Growth rate and genome copy number in *E. coli* growing in M9glyCAAT.**

1273 (**A**) Illustration of 1N (CRISPRi *oriC*, CJW7457) and multi-N (CRISPRi *ftsZ*, CJW7576) cells with different
1274 numbers of chromosomes along with representative microscopy images at different time points
1275 following CRISPRi induction. Scale bars: 1 µm. (**B**) Plot showing representative single-cell trajectories
1276 of cell area as a function of time for the CRISPRi strains following a block in DNA replication and/or
1277 cell division. (**C**) Plot showing the absolute growth rate as a function of cell area for 1N (32735
1278 datapoints from 1568 cells) and multi-N cells (14006 datapoints from 916 cells) in M9glyCAAT. Lines
1279 and shaded areas denote mean ± SD from three experiments. This also applies to the panels below.
1280 (**D**) Absolute and (**E**) relative growth rate in 1N (32735 datapoints from 1568 cells, CJW7457), multi-N
1281 (14006 datapoints from 916 cells, CJW7576), and *dnaC2* 1N (13933 datapoints from 1043 cells,
1282 CJW7374) cells as a function of cell area in M9glyCAAT. (**F**) Absolute and (**G**) relative growth rate in
1283 1N (13933 datapoints from 1043 cells), 2N (6265 datapoints from 295 cells), and >2N (2116 datapoints
1284 from 95 cells) *dnaC2* (CJW7374) cells as a function of cell area in M9glyCAAT.

1285

1286 **Figure 2. Lower ribosome activity explains the reduced growth rate of 1N cells growing in**
1287 **M9glyCAAT.** (**A**) RpsB-msfGFP fluorescence concentration in 1N (6542 cells, CJW7478) and multi-N
1288 (10537 cells, CJW7564) cells as a function of cell area. Lines and shaded areas denote mean ± SD from
1289 three experiments. (**B**) Relative protein concentration of different ribosomal proteins in 1N
1290 (SJ_XTL676) and multi-N (SJ_XTL229) cells by TMT-MS. 1N-rich cells were collected 0, 120, 180, 240
1291 and 300 min after addition of 0.2% arabinose, while multi-N cells were collected after 0, 60, and 120
1292 min of induction. Blue and cyan represent two independent experiments. Only proteins with at least
1293 four peptide measurements are plotted. (**C**) Apparent diffusion coefficients (D_a) of JF549-labeled
1294 RspB-HaloTag in WT (32,410 tracks from 771 cells, CJW7528), 1N (848,367 tracks from 2478 cells,
1295 CJW7529) and multi-N cells (107,095 tracks from 1139 cells, CJW7530). Only tracks of length ≥9
1296 displacements are included. 1N cells are color-binned according to their cell area while multi-N cells
1297 contain aggregated data for ~2-10 μm^2 cell areas. (**D**) D_a in WT cells fitted by a three-state Gaussian
1298 mixture model (GMM): 77 ± 1%, 20 ± 1%, and 3.2 ± 0.5% (±SEM) of the ribosome population, from
1299 the slowest moving to the fastest moving (32,410 tracks from 771 cells). (**E**) Example WT and 1N cells
1300 where active (red, slow-moving) and inactive (gray, fast-moving) ribosomes are classified according
1301 to the GMM. (**F**) Active (slow-moving) ribosome fraction in individual WT (237 cells) and 1N (2453
1302 cells) cells as a function of cell area. Only cells with ≥50 tracks are included. Lines and shaded areas
1303 denote mean and 95% confidence interval (CI) of the mean from bootstrapping. (**G**) Same as (F) but
1304 for WT (237 cells) and multi-N (683 cells) cells. (**H**) Absolute growth rate of 1N and multi-N cells (Figure
1305 1C) as a function of cell area was overlaid with the total active ribosome amount (calculated from
1306 Figure 2A, F, and G). Lines and shaded areas denote mean and 95% CI of the mean from bootstrapping.
1307 All microscopy data are from three biological replicates.

1308

1309 **Figure 3. RNAP activity is reduced in 1N cells growing in M9glyCAAT.** (**A**) RpoC-YFP fluorescence
1310 concentration in 1N (3580 cells, CJW7477) and multi-N (5554 cells, CJW7563) cells as a function of cell
1311 area. Lines and shaded areas denote mean ± SD from three experiments. (**B**) Relative protein
1312 concentration of core RNAP subunits and σ^{70} in 1N-rich (SJ_XTL676) and multi-N (SJ_XTL229) cells by
1313 TMT-MS. 1N-rich cells were collected 0, 120, 180, 240, and 300 min after addition of 0.2% L-arabinose,
1314 while multi-N cells were collected after 0, 60, and 120 min of induction. (**C**) Apparent diffusion
1315 coefficients of JF549-labeled RpoC-HaloTag in WT (91,280 tracks from 1000 cells, CJW7519), 1N
1316 (175884 tracks from 1219 cells, CJW7520) and multi-N cells (186951 tracks from 1040 cells, CJW7527).
1317 Only tracks of length ≥9 displacements are included. 1N cells are binned according to cell area while
1318 multi-N cells contain aggregated data for ~2-15 μm^2 cell areas. (**D**) D_a in WT cells fitted by a 3-state
1319 GMM: 49 ± 4%, 49 ± 4%, and 2 ± 0.1% (± SEM) of the RNAP population, from the slowest moving to
1320 the fastest moving (91,280 tracks from 1,000 cells). (**E**) Example WT and 1N cells where active (red,
1321 slow-moving) and inactive (gray, fast-moving) RNAPs are classified according to the GMM. (**F**) Active
1322 RNAP fraction in individual WT (854 cells) and 1N (1024 cells) cells as a function of cell area. Only cells
1323 with at least 50 tracks are included. Lines and shaded areas denote mean ± 95% CI of the mean from
1324 bootstrapping (3 experiments). (**G**) Same as (F) but for WT (854 cells) and multi-N (924 cells) cells. (**H**)
1325 Total amount of active RNAP in WT, 1N and multi-N cells as a function of cell area (calculated from
1326 Figure 3A, F, and G). Also, shown is a linear fit to multi-N data ($f(x) = 4.16 \cdot 10^4 \cdot x$, R^2 0.98). Lines
1327 and shaded areas denote mean and 95% CI of the mean from bootstrapping. All microscopy data are
1328 from three biological replicates.

1329

1330 **Figure 4. RNASelect and EUB338 concentration measurements in 1N and multi-N cells.** (**A**) Images
1331 of representative cells from a mixed population of 1N (CRISPRi *oriC*) and multi-N (CRISPRi *ftsZ*) cells.
1332 Strains CJW7457 and CJW7576 carrying HU-mCherry were used for the SYTO RNASelect staining
1333 experiment, whereas DAPI-stained strains SJ_XTL676 and SJ_XTL229 were used for the EUB338 rRNA
1334 FISH experiment. (**B**) Concentration distribution of SYTO RNASelect (3077 cells for each population
1335 from five biological replicates) and EUB338 (1254 cells for each population from three biological
1336 replicates) in 1N and multi-N cells. (**C**) The average 1N/multi-N SYTO RNASelect and EUB338
1337 concentration ratio (gray bar) calculated from five and three biological replicates (white circles),
1338 respectively. (**D**) RNASelect and EUB338 concentration ratios as functions of cell area (mean ± SD from
1339 five and three biological replicates, respectively). Single exponential decay functions were fitted to
1340 the average ratios (R^2 > 97%) for each indicated reporter. All concentration comparisons or ratio
1341 calculations were performed for equal numbers of 1N and multi-N cells and overlapping cell area
1342 distributions (see Materials and Methods and Figure 4 – supplement 1).
1343
1344 **Figure 5. Mathematical modeling of DNA limitation.** (**A-C**) Plots comparing simulation results of
1345 model A (solid lines) with experimental data points (dots) and averages (open squares) in the
1346 M9glyCAAT condition. The multi-N and 1N cells are indicated as blue and yellow, respectively: (**A**) The
1347 relation between the absolute growth rate ($\frac{dA}{dt}$) and cell area (A). (**B**) The relation between the active
1348 RNAP fraction and cell area. (**C**) The relation between the active ribosome fraction and cell area. (**D**)
1349 Diagram showing how the fractions of active RNAPs and ribosomes change with DNA concentration
1350 (colored from yellow to blue). Simulated results (filled dots) are based on model A. Experimental data
1351 (points with 2D error bars) from multi-N and 1N cells were combined and shown in the same plot. (**E**)

1352 Plot showing the effect of DNA limitation (using the ODE model A) on the decay of DNA concentration,
1353 mRNA concentration, and relative growth rate in 1N cells. Each quantity was normalized to their value
1354 at normal cell size (cell area = 2.5 μm^2).
1355
1356 **Figure 6. Scaling of the total active RNAPs, total active ribosomes, and growth rate with cell area**
1357 **during genome dilution in nutrient-poor media. (A)** Plot showing the total amount of active RNAPs
1358 (calculated by multiplying the total amount of RNAPs by the fraction of active RNAPs from Figure 6 –
1359 figure supplement 1A and G) in WT (CJW7339) and 1N (CJW7457) cells grown in M9gly as a function
1360 of cell area. Also shown is a linear fit to WT data ($f(x) = 3.99 \cdot 10^4 \cdot x$, R^2 0.90). Shaded areas denote
1361 95% CI of the mean from bootstrapping. All data are from three biological replicates. (**B**) Same as (A)
1362 but for cells grown in M9ala (calculated from Figure 6 – figure supplement 1B and H). The linear fit for
1363 WT data is $f(x) = 3.21 \cdot 10^4 \cdot x$, R^2 0.95. (**C**) Plot showing the total active ribosome amount of 1N
1364 and multi-N cells grown in M9gly as a function of cell area. The total amount of active ribosomes was
1365 calculated by multiplying the total amount of ribosomes by the fraction of active ribosomes (from
1366 Figure 6 – figure supplement 2A and G). Also shown is a linear fit to WT data ($f(x) = 2.99 \cdot 10^4 \cdot x$,
1367 R^2 0.97). Lines and shaded areas denote mean and 95% CI of the mean from bootstrapping. All data
1368 are from three biological replicates. (**D**) Same as (C) but for cells grown in M9ala (calculated from
1369 Figure 6 – figure supplement 2B and H). Here the linear fit to the WT data is $f(x) = 1.90 \cdot 10^4 \cdot x$, R^2
1370 0.99. (**E**) Absolute growth rate in 1N (50352 datapoints from 973 cells) and WT (80269 datapoints
1371 from 12544 cells) cells in M9gly. The linear fit for WT data is $f(x) = 6.50 \cdot 10^{-3} \cdot x$, R^2 0.99. (**F**)
1372 Absolute growth rate in 1N (71736 datapoints from 909 cells) and WT (63367 datapoints from 6880

1373 cells) cells in M9ala. The linear fit for WT data is $f(x) = 4.05 \cdot 10^{-3} \cdot x$, R^2 0.97. Lines and shaded
1374 areas denote mean ± SD from three biological replicates.
1375
1376 **Figure 7. Proteome and transcriptome remodeling in 1N-rich cells.** (**A**) Schematic explaining the
1377 calculation of the protein slopes, which describes the scaling of the relative protein concentration
1378 (concentration of a given protein relative to the proteome) with cell area. (**B**) Plot showing the protein
1379 scaling (average slopes from two reproducible biological replicates, see Figure 7 – supplement 1A-B)
1380 in 1N (x-axis) and multi-N (y-axis) cells across the detected proteome (2360 proteins). The colormap
1381 corresponds to a Gaussian kernel density estimation (KDE). (**C**) Plot showing the first principal
1382 component (PC1, which explains 69% of the total variance considering both 1N-rich and multi-N cells)
1383 used to reduce the dimensionality of the relative protein concentration during cell growth. The x-axis
1384 corresponds to the log-transformed cell area, whereas the marker size shows the cell area increase in
1385 linear scale. (**D**) Correlation between average protein and RNA slopes across 2324 genes. The
1386 colormap corresponds to a KDE. (**E**) Relation between mRNA abundance (transcripts per million 60min
1387 after CRISPRi induction) and RNA slopes in 1N-rich cells. The colormap indicates a KDE (3446 genes in
1388 total). The binned data are also shown (orange markers: mean ± SEM, ~380 genes per bin). The
1389 Spearman correlation (ρ = -0.04) is considered not significant (NS, p-value > 10^{-10}). (**F**) Correlation
1390 between RNA slopes and mRNA degradation rate from a published dataset (Balakrishnan et al., 2022)
1391 across genes. The colormap indicates a KDE (2570 genes with positive mRNA degradation rates and
1392 quantified slopes). The binned data are also shown (orange markers: mean ± SEM, ~280 genes per
1393 bin). A significant negative Spearman correlation (p-value < 10^{-10}) is shown for mRNAs with a
1394 degradation rate above 0.7 min^{-1}. (**G**) RNA-slope comparison between essential and non-essential

1395 genes in *E. coli*. Three different published sets of essential genes were used (Gerdes et al., 2003;
1396 Goodall et al., 2018; Hashimoto et al., 2005). The horizontal white lines indicate the inter-quartile
1397 range of each distribution. Mann-Whitney non-parametric tests justify the significant difference (p-
1398 value < 10^{-10}) between the two gene groups (essential vs. non-essential genes).
1399
1400 **SUPPLEMENTARY FIGURE LEGENDS**
1401 **Figure 1 – figure supplement 1. The relative growth rate of WT (CJW7339) cells in M9glyCAAT grown**
1402 **after placing them on an agarose pad.** The plot includes 61562 data points from 11907 cells. Lines
1403 and shaded areas denote mean ± SD from three biological replicates.
1404
1405 **Figure 1 – figure supplement 2. Characterization of ploidy in CRISPRi *oriC* cells.** Representative
1406 microscopy images of CRISPRi *oriC* cells expressing HU-CFP and ParB-mCherry with *parS* site at *ori1*
1407 (CJW7517) in M9glyCAAT 210 min after addition of 0.2% L-arabinose. Scale bar: 1 µm.
1408
1409 **Figure 1 – figure supplement 3. Effects of cell area overestimation on the relative growth rate**
1410 **calculation.** The simulated relative growth rate for increasing cell area considering different levels of
1411 cell area over-estimation (0 to 0.2 μm^2) and a constant relative growth rate of 0.0014 1/min. In the
1412 absence of an area overestimation (0 μm^2), the theoretical relative growth rate remains constant as
1413 the cell area increases, consistent with exponential growth. When a constant overestimated area is
1414 added the relative growth rate scales non-linearly with the cell area. This non-linear increase in the
1415 relative growth rate estimation may be confused with super-exponential growth, but it is in fact the
1416 result of cell area overestimation during cell segmentation in the phase contrast channel.

1417

1418 **Figure 1 – figure supplement 4. Relationship between growth rate and cell area in cell types of**
1419 **different ploidy.** (**A**) Absolute and (**B**) relative growth rate in M9glyCAAT in 1N (32735 datapoints from
1420 1568 cells, CJW7457), multi-N (14006 datapoints from 916 cells, CJW7576), and WT (19495 datapoints
1421 from 7440 cells, CJW7339) cells as a function of cell area. Lines and shaded areas denote mean ± SD
1422 from three biological replicates.

1423

1424 **Figure 1 – figure supplement 5. Validation of stable growth under microscope observation and**
1425 **absolute growth rate determination of ppGpp^0 and Δ*recA* cells.** (**A**) Plot showing the absolute growth
1426 rate of 1N (CJW7457) cells grown for 90 min in a liquid M9glyCAAT culture in the presence of 0.2% L-
1427 arabinose and then transferred to an agarose pad and imaged for 2 h (dotted line). The data for 1N
1428 (CJW7457) and multi-N (CJW7576) cells (presented in Figure 1C), which were grown on an agarose
1429 pad for 6 h, are also shown for comparison. Lines and shaded areas denote mean ± SD from two
1430 biological replicates. (**B**) Plot showing the absolute growth rate of ppGpp^0 (CJW7518) and Δ*recA*
1431 (CJW7522) cells. Lines and shaded areas denote mean ± SD from two biological replicates. Also shown
1432 are the data for 1N (CJW7457) and multi-N (CJW7576) cells from Figure 1C.

1433

1434 **Figure 1 – figure supplement 6. Characterization of ploidy in *dnaC2* cells.** (**A**) Representative
1435 microscopy images of WT (top) and *dnaC2* (bottom) cells expressing HU-mCherry growing under
1436 microscope observation in M9glyCAAT. DNA replication in *dnaC2* cells was blocked by growing cells
1437 at 37°C for 145 min. Arrows indicate *dnaC2* cells with one (1N) or two (2N) nucleoids. Scale bars: 1

1438 µm. (**B**) Graph showing the percentage of *dnaC2* cells (CJW7374) with 1, 2 or >2 nucleoids after growth
1439 at 37°C. Shown are aggregated data from three biological replicates.
1440
1441 **Figure 1 – figure supplement 7. Relationships between growth rate and cell volume across cell types**
1442 **of different ploidy in M9glyCAAT.** (**A**) Absolute and (**B**) relative growth rate based on cell volume in
1443 1N (32735 datapoints from 1568 cells, CJW7457), multi-N (14006 datapoints from 916 cells, CJW7576),
1444 and *dnaC2* 1N (13933 datapoints from 1043 cells, CJW7374) cells as a function of cell volume. Lines
1445 and shaded areas denote mean ± SD from three experiments. The growth rates are based on volume
1446 in this figure. (**C**) Absolute and (**D**) relative growth rate in 1N (32735 datapoints from 1568 cells,
1447 CJW7457), multi-N (14006 datapoints from 916 cells, CJW7576), and WT (19495 datapoints from 7440
1448 cells, CJW7339) cells as a function of cell area. (**E**) Absolute growth rate and (**F**) relative growth rate
1449 in 1N (13933 datapoints from 1043 cells), 2N (6265 datapoints from 295 cells), and >2N (2116
1450 datapoints from 95 cells) *dnaC2* (CJW7374) cells as a function of cell area. (**G**) Cell width in WT (59072
1451 datapoints from 7640 cells, CJW7339), 1N (41313 datapoints from 1585 cells, CJW7477), and multi-N
1452 (18489 datapoints from 915 cells, CJW7563) cells as a function of cell area. Lines and shaded areas
1453 denote mean ± SD from 3 biological replicates.
1454
1455 **Figure 1 – figure supplement 8. DNA-dependent growth in *Caulobacter crescentus*.** (**A**) Plot showing
1456 the absolute and (**B**) relative growth rate of 1N (DnaA depletion, strain CJW4823, 87 cells) and multi-
1457 N (FtsZ depletion, strain CJW3673, 181 cells) *C. crescentus* cells as a function of cell area. Lines and
1458 shaded areas denote mean ± SD from three biological replicates. (**C**) Example images of 1N and multi-
1459 N *C. crescentus* cells with ploidy represented by the number of ParB-eCFP foci. Scale bar: 2 µm.

1460

1461 **Figure 2 – figure supplement 1. Diffusive characteristics of labeled ribosomes in rifampicin-treated**
1462 **WT cells.** (**A**) Plot showing the probability density of apparent diffusion coefficients (D_a) of JF549-
1463 labeled RpsB-HaloTag in WT cells (CJW7528) treated with 200 µg/mL rifampicin for 30 min. Only tracks
1464 of length ≥10 are included. Also shown is D_a fitted by three-state Gaussian mixture model (GMM)
1465 (mean ± SEM). Data are from three biological replicates.

1466

1467 **Figure 2 – figure supplement 2. Diffusive characteristics of labeled ribosomes in 1N cells as a**
1468 **function of cell area.** Plots showing the probability density of apparent diffusion coefficients (D_a) of
1469 JF549-labeled RpsB-HaloTag in 1N cells (CJW7529) in M9glyCAAT at different cell areas. Also shown is
1470 D_a fitted by three-state Gaussian mixture model (GMM). Only tracks of length ≥10 are included. Data
1471 are from three biological replicates.

1472

1473 **Figure 3 – figure supplement 1. Diffusive characteristics of labeled RNAPs in rifampicin-treated cells.**
1474 Plot showing the probability density of apparent diffusion coefficients (D_a) of JF549-labeled RpoC-
1475 HaloTag in CJW7519 cells treated with 200 µg/mL rifampicin for 30 min. Also shown is D_a fitted by
1476 three-state Gaussian mixture model (mean ± SEM). Only tracks of length ≥10 are included. Data are
1477 from three biological replicates.

1478

1479 **Figure 3 – figure supplement 2. Determination of the relative Rsd concentration in 1N-rich and**
1480 **multi-N cells as a function of cell area.** Plots showing the relative protein concentration of Rsd in 1N-
1481 rich (SJ_XTL676) and multi-N (SJ_XTL229) cells, as determined by TMT-MS. 1N-rich cells grown in

1482 M9glyCAAT were collected 0, 120, 180, 240 and 300 min, while multi-N cells were collected at 0, 60,
1483 and 120 min after 0.2% L-arabinose induction of CRISPRi. Different shades of gray represent two
1484 independent experiments.
1485
1486 **Figure 4 – figure supplement 1. Cell sampling to match cell size distribution in mixed populations of**
1487 **1N and multi-N cells.** (**A**) Cell area distributions from mixed CJW7457 (CRISPRi *oriC*) and CJW7576
1488 (CRISPRi *ftsZ*) populations stained with SYTO RNASelect (aggregated data from five biological
1489 replicates) before and after cell area sampling (cell area bins with less than 50 cells were removed
1490 from the analysis). (**B**) Cell area distributions from mixed SJ_XTL676 (CRISPRi *oriC*) and SJ_XTL229
1491 (CRISPRi *ftsZ*) populations stained with the EUB338 FISH probe (aggregated data from three biological
1492 replicates) before and after cell area sampling (cell area bins with less than 25 cells were removed
1493 from the analysis).
1494
1495 **Figure 4 – figure supplement 2. Comparison of RpoC-HaloTag-JF549 labelling between 1N and multi-**
1496 **N cells.** (**A**) Phase contrast (left) and RpoC-HaloTag-JF549 fluorescence (right) images of two
1497 representative cells from a mixed population of 1N (CRISPRi *oriC*, CJW7520) and multi-N (CRISPRi *ftsZ*,
1498 CJW7527) cells. (**B**) Cell area distributions from mixed 1N and multi-N cell populations in which RpoC-
1499 HaloTag was stained with the JF549 dye (aggregated data from two biological replicates) before and
1500 after cell area sampling. (**C**) Distributions of RpoC-HaloTag-JF549 signal concentration for 1N and
1501 multi-N cells (748 cells for each population from two biological replicates). (**D**) Average 1N/multi-N
1502 RpoC-HaloTag-JF549 concentration ratio (gray bar), calculated from two biological replicates (white
1503 circles) after sampling the same number of cells per biological replicate and cell area bin for each

1504 population (panel B). (**E**) Plot showing the concentration ratio of fluorescently labeled RpoC
1505 derivatives between 1N and multi-N cells versus the cell area. Squares show mean ± full range of
1506 RpoC-HaloTag-JF549 signal concentration ratios from two biological replicates, whereas grey circles
1507 indicate the mean signal concentration ratio of RpoC-YFP (from data shown in Figure 3A) for
1508 comparison. A linear regression (red dashed line) was fitted to the average RpoC-HaloTag-JF549 ratios.
1509 A cell area of ~2.8 μm^2 corresponds to a 1N/multi-N RpoC-HaloTag-JF549 concentration ratio equal
1510 to 1.
1511
1512 **Figure 4 – figure supplement 3. EUB338 staining comparison between fast (M9glyCAAT) and slow**
1513 **(M9gly) growing populations.** (**A**) Relative cell area and EUB338 concentration distributions from
1514 wildtype MG1655 exponentially growing populations in M9glyCAAT or M9gly. Data from two
1515 biological replicates (rep) are shown (M9glyCAAT rep 1: 5867 cells, M9glyCAAT rep 2: 9728 cells,
1516 M9gly rep 1: 8301 cells, M9gly rep 2: 3766 cells). The iso-contour plots (nine levels above the 25th
1517 density percentile) include data from both biological replicates per nutrient condition. (**B**)
1518 Representative fields of the EUB338 fluorescence in stained fixed cells that were grown in M9glyCAAT
1519 (top) or M9gly (bottom). For comparison, the two fields of view have the same dimensions, and the
1520 fluorescence is scaled the same.
1521
1522 **Figure 5 – figure supplement 1. Comparison between experimental results from the M9glyCAAT**
1523 **condition and simulation results using model B.** (**A-C**) Plots comparing simulation results of model B
1524 (solid lines) with experimental data (dots) and averages (open squares). The multi-N and 1N cells are
1525 indicated as blue and yellow, respectively: (**A**) The relation between the absolute growth rate ($\frac{dA}{dt}$) and

1526 cell area (A). (**B**) The relation between the active RNAP fraction and cell area. (**C**) The relation between
1527 the active ribosome fraction and cell area. (**D**) A two-dimensional diagram showing how the fractions
1528 of active RNAPs and ribosomes change with DNA concentration (colored from yellow to blue).
1529 Experimental data (with 2D error bars) from multi-N and 1N cells were combined and shown in the
1530 same plot.
1531
1532 **Figure 5 – figure supplement 2. Model A-based simulations examining the effects of varying the**
1533 **rates in either mRNA synthesis or mRNA degradation on the relative growth rate of 1N cells as a**
1534 **function of cell area.** (**A**) Plot showing the decay of DNA concentration (black) and of the relative
1535 growth rate (blue) in 1N cells when the rate of bulk mRNA synthesis (r_1) increases or decreases by
1536 ten-fold. Each quantity was normalized to its value at normal cell size (cell area = 2.5 μm^2). (**B**) Same
1537 as (A) except mRNA degradation rate δ increasing or decreasing by ten-fold.
1538
1539 **Figure 6 – figure supplement 1. Characterization of RNAP diffusion and active fraction in poor media**
1540 **conditions.** (**A**) Plot showing the RpoC-YFP fluorescence concentration in 1N (CJW7477) cells grown
1541 in M9gly (three experiments) as a function of cell area. Lines and shaded areas denote mean ± SD
1542 between biological replicates. (**B**) Same as (A) but for 1N cells grown in M9ala (three experiments). (**C**)
1543 Plot showing the probability densities of apparent diffusion coefficients (D_a) of JF549-labeled RpoC-
1544 HaloTag in WT (CJW7519) and 1N (CJW7520) cells grown in M9gly. Only tracks of length ≥10 are
1545 included. 1N cells were binned according to cell area. (**D**) Same as (C) but for cells grown in M9ala. (**E**)
1546 Plot showing the probability density of D_a of JF549-labeled RpoC-HaloTag in WT cells (CJW7519) grown
1547 in M9gly. Also shown is D_a fitted by three-state Gaussian mixture model (GMM) (mean ± SEM). (**F**)

1548 Same as (E) but for cells grown in M9ala. (**G**) Plots showing the fraction of active RNAPs in individual
1549 WT (CJW7519) and 1N (CJW7520) cells (dots) grown in M9gly as a function of cell area. Only cells with
1550 ≥50 tracks are included. (**H**) Same as (G) but for cells grown in M9ala.
1551
1552 **Figure 6 – figure supplement 2. Characterization of ribosomal diffusion and active fraction in poor**
1553 **media conditions.** (**A**) Plot showing the RpsB-msfGFP fluorescence concentration in 1N (CJW7478)
1554 cells grown in M9gly (from three experiments) as a function of cell area. Lines and shaded areas
1555 denote mean ± SD between the biological replicates. (**B**) Same as (A) but for 1N cells grown in M9ala
1556 (from two experiments). (**C**) Plot showing the probability density of apparent diffusion coefficients (D_a)
1557 of JF549-labeled RpsB-HaloTag across cell areas for WT (CJW7528) and 1N (CJW7529) cells grown in
1558 M9gly. Only tracks of length ≥10 are included. 1N cells were binned according to cell area. (**D**) Same
1559 as (C) for cells grown in M9ala. (**E**) Plot showing probability density of D_a of JF549-labeled RpsB-
1560 HaloTag in WT cells (CJW7528) grown in M9gly. Only tracks of length ≥10 are included. Also shown is
1561 D_a fitted by three-state GMM (mean ± SEM). (**F**) Same as (E) but for cells grown in M9ala. (**G**) Plot
1562 showing the fraction of active ribosomes as a function of cell area for individual WT (CJW7528) and
1563 1N (CJW7529) cells (dots) grown in M9gly. Only cells with ≥50 tracks are included. Shaded areas
1564 denote 95% confidence interval (CI) of the mean from bootstrapping. (**H**) same as (G) but for cells
1565 grown in M9ala.
1566
1567 **Figure 7 – figure supplement 1. Comparison of protein and mRNA scaling between biological**
1568 **replicates.** (**A**) Correlation of protein slopes across the proteome (2360 proteins) between two
1569 biological replicates for 1N cells. (**B**) Same as (A) but for multi-N cells. (**C**) Correlation of RNA slopes

1570 across the genome (3446 mRNAs) of 1N cells between two biological replicates. The indicated
1571 Spearman correlation shown (ρ) is significant (p-value < 10^{-10}).
1572
1573 **Figure 7 – figure supplement 2. Comparison of our data with reference datasets.** (**A**) Comparison
1574 between the concentrations of 3446 RNAs present in both our dataset and that of Balakrishnan et al
1575 (2022). The first time point (60 min) after CRISPRi induction was used to determine the RNA
1576 abundance in our experiments. The RNA concentration was expressed as transcripts per million reads.
1577 The indicated Spearman correlations (ρ) are significant (p-value < 10^{-10}). Each marker represents a
1578 single gene or protein and the colormap shows the KDE. (**B**) Correlations between RNA slopes (from
1579 2577 genes, ~280 genes per bin) in 1N cells and the rate of transcription initiation in wildtype cells
1580 (Balakrishnan et al., 2022). The binned data are also shown (orange markers: mean ± SEM). The p-
1581 value of ρ is not significant (p-value > 10^{-10}). (**C**) Same as (B) but for protein slopes instead of RNA
1582 slopes (2084 genes, ~230 genes per bin). (**D**) Correlation between protein slopes in 1N cells and mRNA
1583 degradation rate in wildtype cells (Balakrishnan et al., 2022). The colormap corresponds to KDE (for
1584 2078 genes with positive mRNA degradation rates). The binned data are also shown (orange markers:
1585 mean ± SEM, ~230 genes per bin). A significant negative Spearman correlation (p-value < 10^{-10}) is
1586 shown for genes with a degradation rate above 0.7 min^{-1}. (**E**) Comparison of the mRNA degradation
1587 rates (Balakrishnan et al., 2022) between essential and non-essential genes in *E. coli*. Three different
1588 published sets of essential genes were used (Gerdes et al., 2003; Goodall et al., 2018; Hashimoto et
1589 al., 2005). The horizontal white lines indicate the inter-quartile range of each distribution. Mann-
1590 Whitney non-parametric tests justify the non-significant difference (p-value > 10^{-2}) between the two
1591 gene groups (essential vs non-essential genes).

1592

1593 **Figure 7 – figure supplement 3. Protein slopes relative to the chromosome position of their gene in**
1594 **1N-rich and multi-N cells.** (**A**) Relationship between the absolute distance of a gene from *oriC* and the
1595 slope of the protein it encodes. Data from 2268 proteins are shown (colormap: Gaussian kernel
1596 density estimation), as well as binned data in six gene distance bins (open circles, average ± SEM, ~370
1597 proteins per bin). For the multi-N cells, the Spearman correlation was not significant (ρ = NS, p-value >
1598 0.01), whereas for the 1N-rich cells, there was a significant Spearman correlation ($\rho = 0.23$, p-value <
1599 10^{-10}) for genes within 1.35 Mbps of *oriC* (below the mid-point of the 4th gene distance bin). (**B**)
1600 Relationship between the absolute distance of a gene from *oriC* and its mRNA slope. Data from 2200
1601 RNAs are shown (colormap: Gaussian kernel density estimation), as well as binned data in six gene
1602 distance bins (open circles, average ± SEM, ~360 proteins per bin). The Spearman correlation is not
1603 significant ($\rho = -0.02$, p-value > 0.1).

1604

1605 **Figure 7 – figure supplement 4. Protein slopes relative to protein ion intensity for 1N-rich cells.** The
1606 summed ion intensity of each protein was divided by the protein sequence length and the quotient
1607 was log-transformed. The locations of selected proteins are annotated.

1608

1609

1610

1611

1612

1613

1614 **Table 1: Model parameter description**

1615

Para-meter	Biological meaning	Unit	Description
r_1	$\frac{\text{bulk transcription rate}}{\text{total protein number}}$	10^{-3}/min	This parameter was estimated as $r_1 = \theta_{RNAP}\beta_{mRNA} / T_{RNAP}$, where θ_{RNAP} is the number of RNAPs normalized by the number of proteins; β_{mRNA} is the fraction of RNAPs engaged in transcription, and T_{RNAP} is the mean mRNA synthesis time.
r_2	$\frac{\text{bulk translation rate}}{\text{total protein number}}$	10^{-3}/min	This parameter was estimated by $r_2 = \theta_{ribo} / T_{ribo}$, where θ_{ribo} is the number of ribosomes normalized by the number of proteins, and T_{ribo} is the mean protein synthesis time.
K_1	Saturation level of DNA with respect to RNAP binding	$1/\mu m^3$	This parameter was estimates from $\alpha_{RNAP} = \frac{[Z]}{K_1+[Z]}$, where α_{RNAP} is measured in this work and $[Z]_{avg}$, the mean genome copy.
K_2	Saturation level of mRNA with respect to ribosome binding	$1/\mu m^3$	This parameter was estimated as $\alpha_{ribo} = \frac{[X]}{K_2+[X]}$, where α_{ribo} is measured in this work and $[X]$, the mRNA concentration.
δ	mRNA degradation rate	1/min	$\delta = 1/\tau_L$, where τ_L is the mRNA lifetime
c	$\frac{\text{cell volume}}{\text{protein number}}$	$10^{-6}\mu m^3$	Cell volumes of different culture conditions were measured in this work.
c'	$\frac{\text{cell area}}{\text{protein number}}$	$10^{-6}\mu m^2$	Cell area of different culture conditions was measured in this work.
$[Z]_{avg}$	Average genome concentration of normal-growing cells	genome/ μm^3	Estimated by averaging the genome concentration over the cell cycle, see Appendix 1 for details.

1616

1617

1618

1619 **Table 2: Initial and optimized model parameters**

1620

Parameter	Unit	Initial estimation	Optimized parameters	
			M9glyCAA (model A)	M9glyCAA (model B)
r_1	10^{-3}/min	1.99	1.22	1.76
r_2	10^{-3}/min	20.0	22.4	22.5
K_1	$1/\mu m^3$	1.40	1.17	1.55
K_2	$1/\mu m^3$	622	797	532

δ	1/min	0.96	1.27	1.31
c	$10^{-6}\mu m^3$	0.28	0.28	0.18
c'	$10^{-6}\mu m^2$	0.47	-	-
X_{ini}	10^2/cell	20.2	-	-
Y_{ini}	10^6/cell	3.82	-	-
$[Z]_{avg}$	genome /cell	1.40	-	-

1621

1622 **Table 3. Strains used in this study**. The abbreviations *kan*, *cat*, and *spec* refer to gene cassette
1623 insertions conferring resistance to kanamycin, chloramphenicol, and spectinomycin, respectively.
1624 These insertions are flanked by Flp site-specific recombination sites (*frt*) that allow the removal of the
1625 insertion using Flp recombinase from plasmid pCP20 (Cherepanov and Wackernagel, 1995).

1626

Identifier	**Genotype**	**Source**
CJW2591	CB15N Δ*bla6 ftsZ*::pBGent-pXyl-ftsZ	BamHI/HindIII fragment was cut from YF1585 and cloned into pBGent. The resulting plasmid was integrated into LS107 (Wang et al., 2001).
CJW3673	CB15N *ftsZ*::pBGentpXyl-ftsZ *parB*::*ecfp-parB*	UV-inactivated ϕCr30 phage lysate was prepared from CJW2591 and transduced into MT190.
CJW4823	CB15N *parB*::*ecfp-parB dnaA*::Ω xylX::pGM2195	UV-inactivated ϕCr30 phage lysate was prepared from GM2471. First, pGM2195 was transduced into MT190, followed by a second transduction of Ω into the resulting strain to disrupt the endogenous *dnaA* gene.
CJW6737	DH5α/pKFSS1_parS^{pMT1}	parS^{pMT1} was amplified from FH3518 (Nielsen et al., 2006) using oligonucleotides NT157 and NT158, digested with BamHI and KpnI, and cloned into the BamHI/KpnI sites of pKFSS1_2 (Takacs et al., 2018).
CJW7019	MG1655 *rpsB*::*rpsB-msfgfp-kan*	(Gray et al., 2019)
CJW7079	CB15N *rplA(L1)*::*rplA(L1)-mCherry*	CJW7080 was subjected to counterselection on 0.3% xylose.

CJW7080	CB15N *rplA(L1)*::pNPTS138-rplA(L1)-mCherry-rplA(L1)DOWN	The vector pNPTS138 (M. R. Alley, unpublished) was PCR-amplified using oligomers JSG_018 and JSG_019. A ~500-bp fragment of the 3' end of the *rplA(L1)* gene, and a ~500 bp fragment immediately downstream of the *rplA* gene (rplA(L1)DOWN), were amplified from a CB15N genome template using oligomers JSG_024 and JSG_025, and JSG_020 and JSG_021, respectively. *mCherry* was amplified from MTLS4218 (Thanbichler et al., 2007) and a linker was introduced using JSG_022 and JSG_023. All products were assembled into a plasmid via Gibson assembly. The resulting plasmid, which was verified by sequencing junctions, was transformed into S17-1 and introduced into CB15N by conjugation with selection for kanamycin and nalidixic acid resistance.
CJW7339	MG1655 *hupA*::*hupA-mCherry-kan*	*hupA*::*hupA-mCherry-kan* from CJW5556 (Paintdakhi et al., 2016) was moved into MG1655 by P1 transduction.
CJW7374	MG1655 *hupA*::*hupA-mCherry dnaC*::*dnaC2(ts) mdoB*::*kan*	The kanamycin resistance cassette was excised from CJW7339 by expressing the Flp site-specific recombinase from pCP20 (Cherepanov and Wackernagel, 1995). *dnaC*::*dnaC2(ts) mdoB*::*kan* from FW1957 (Wu et al. 2010) was subsequently moved into this strain by P1 transduction.
CJW7411	MG1655 *glmS1868*::*parS(pMT1)-frt-kanR-frt*	Plasmid backbone was amplified from CJW6919 (Kim et al., 2019) using oligonucleotides AP0039 and AP0040, pMT1 *parS* was amplified from CJW6737 using AP0041 and AP0042, and the fragments were ligated by Gibson assembly. *parS(pMT1)-frt-*

		kanR-frt was amplified from the resulting plasmid with AP0078 and AP0079. The amplicon was inserted between *glmS* and *pstS* by λ-red mediated recombination (Datsenko and Wanner, 2000).
CJW7457	MG1655 *lacY(A177C) araFGH*::*spec ΔlacI ΔaraE araBAD*::*dCas9 galM<PBBa-J23119-sgRNA(oriC)-(S. pyogenes terminator)-(rrnB terminator)>gmpA hupA*::*hupA-mCherry-kan*	*hupA*::*hupA-mCherry-kan* from CJW5556 (Paintdakhi et al., 2016) was moved into SJ_XTL676 by P1 transduction.
CJW7473	CB15N *rplA(L1)*::*rplA(L1)-mCherry ftsZ*::pBGentpXyl-ftsZ	UV-inactivated ϕCr30 phage lysate was prepared from CJW7080 and used for transduction into CJW3673. Tranductants were selected on kanamycin, and then counterselected on 0.3 % xylose.
CJW7477	MG1655 *lacY(A177C) araFGH*::*spec ΔlacI ΔaraE araBAD*::*dCas9 galM<PBBa-J23119-sgRNA(oriC)-(S. pyogenes terminator)-(rrnB terminator)>gmpA hupA*::*hupA-mCherry rpoC*::*rpoC-ygfp-kan*	The kanamycin resistance cassette was excised from CJW7457 by expressing the Flp site-specific recombinase from pCP20 (Cherepanov and Wackernagel, 1995). *rpoC*::*rpoC-ygfp-kan* from RLG7470 was subsequently moved into this strain by P1 transduction.
CJW7478	MG1655 *lacY(A177C) araFGH*::*spec ΔlacI ΔaraE araBAD*::*dCas9 galM<PBBa-J23119-sgRNA(oriC)-(S. pyogenes terminator)-(rrnB terminator)>gmpA hupA*::*hupA-mCherry rpsB*::*rpsB-msfgfp-kan*	The kanamycin resistance cassette was excised from CJW7457 by expressing the Flp site-specific recombinase from pCP20 (Cherepanov and Wackernagel, 1995). *rpsB*::*rpsB-msfgfp-kan* from CJW7019 was subsequently moved into this strain by P1 transduction.
CJW7500	CB15N *rplA(L1)*::*rplA(L1)-mCherry dnaA*::Ω xylX::pGM2195	UV-inactivated ϕCr30 phage lysate was prepared from GM2471. A double transduction was performed into CJW7079.
CJW7517	MG1655 *lacY(A177C) araFGH*::*spec ΔlacI ΔaraE araBAD*::*dCas9 galM<PBBa-J23119-sgRNA(oriC)-(S. pyogenes*	The strain was generated by first moving *gtrA*::*P58-mCherry-parB(pMT1)-cat* (Wiktor et al., 2021) into SJ_XTL676 by P1 transduction.

	terminator)-(rrnB terminator)>gmpA gtrA::*P58-mCherry-parB(pMT1) parS(pMT1) at ori1 hupB*::*hupB-cfp-kan*	Next, *parS(pMT1)-kan* at *ori1* from CJW7411 was moved into the strain by P1 transduction. The resistance genes were excised by expressing the Flp site-specific recombinase from pCP20 (Cherepanov and Wackernagel, 1995). Finally, *hupB*::*hupB-cfp-kan* from CJW4656 (Gray et al., 2019) was moved into the strain by P1 transduction.
CJW7518	MG1655 *lacY(A177C) araFGH*::*spec ΔlacI ΔaraE araBAD*::*dCas9 galM<PBBa-J23119-sgRNA(oriC)-(S. pyogenes terminator)-(rrnB terminator)>gmpA hupA*::*hupA-mcherry ΔrelA251*::*kan ΔspoT207*::*cat*	The kanamycin resistance cassette was excised from CJW7457 by expressing the Flp site-specific recombinase from pCP20 (Cherepanov and Wackernagel, 1995). *ΔrelA251*::*kan* and *ΔspoT207*::*cat* were subsequently moved into this strain by two P1 transductions from strain CF1693 (Xiao et al., 1991).
CJW7519	MG1655 *rpoC*::*rpoC-HaloTag-kan*	The strain was generated by first creating *rpoC-HaloTag-kan* amplicon with oligonucleotides JSG_148 and JSG_149 from strain JM41 (Mäkelä and Sherratt, 2020). This amplicon was used to replace the endogenous *rpoC* by λ-red mediated recombination (Datsenko and Wanner, 2000). Finally, *rpoC*::*rpoC-HaloTag-kan* was moved into MG1655 by P1 transduction.
CJW7520	MG1655 *lacY(A177C) araFGH*::*spec ΔlacI ΔaraE araBAD*::*dCas9 galM<PBBa-J23119-sgRNA(oriC)-(S. pyogenes terminator)-(rrnB terminator)>gmpA rpoC*::*rpoC-HaloTag-kan*	*rpoC*::*rpoC-HaloTag-kan* from CJW7519 was moved into SJ_XTL676 by P1 transduction.
CJW7522	MG1655 *lacY(A177C) araFGH*::*spec ΔlacI ΔaraE araBAD*::*dCas9 galM<PBBa-J23119-sgRNA(oriC)-(S. pyogenes terminator)-(rrnB*	*recA* was replaced by *kan* using oligonucleotides JSG_173 and JSG_174 in MG1655 by λ-red mediated recombination (Datsenko and Wanner, 2000). The kanamycin resistance cassette was excised from

	terminator)>gmpA hupA::*hupA-mCherry ΔrecA*::*kan*	CJW7457 by expressing the Flp site-specific recombinase from pCP20 (Cherepanov and Wackernagel, 1995) and *ΔrecA*::*kan* was subsequently moved into the strain by P1 transduction.
CJW7527	MG1655 *lacY(A177C) araFGH*::*spec ΔlacI ΔaraE araBAD*::*dCas9 galM<PBBa-J23119-sgRNA(ftsZ)-(S. pyogenes terminator)-(rrnB terminator)>gmpA rpoC*::*rpoC-HaloTag-kan*	*rpoC*::*rpoC-HaloTag-kan* from CJW7519 was moved into SJ_XTL229 by P1 transduction.
CJW7528	MG1655 *rpsB*::*rpsB-HaloTag-kan*	The strain was generated by first creating *rpsB-HaloTag-kan* amplicon with oligonucleotides JSG_157 and JSG_158 from strain JM41 (Mäkelä and Sherratt, 2020). This amplicon was used to replace the endogenous *rpsB* by λ-red mediated recombination (Datsenko and Wanner, 2000). Finally, *rpsB*::*rpsB-HaloTag-kan* was moved into MG1655 by P1 transduction.
CJW7529	MG1655 *lacY(A177C) araFGH*::*spec ΔlacI ΔaraE araBAD*::*dCas9 galM<PBBa-J23119-sgRNA(oriC)-(S. pyogenes terminator)-(rrnB terminator)>gmpA rpsB*::*rpsB-HaloTag-kan*	*rpsB*::*rpsB-HaloTag-kan* from CJW7528 was moved into SJ_XTL676 by P1 transduction.
CJW7530	MG1655 *lacY(A177C) araFGH*::*spec ΔlacI ΔaraE araBAD*::*dCas9 galM<PBBa-J23119-sgRNA(ftsZ)-(S. pyogenes terminator)-(rrnB terminator)>gmpA rpsB*::*rpsB-HaloTag-kan*	*rpsB*::*rpsB-HaloTag-kan* from CJW7528 was moved into SJ_XTL229 by P1 transduction.
CJW7531	CB15N *rpoC*::*mCherry-rpoC*	Two DNA segments of vector pNPTS138 (M. R. Alley, unpublished) were PCR-amplified using oligomers JSG_134 and JSG_137, and JSG_135 and JSG_136. A ~900 bp fragment

		upstream of the *rpoC* gene and ~900 bp of the 5' end of *rpoC* were amplified from a CB15N genome template using oligomers JSG_128 and JSG_129, and JSG_132 and JSG_133, respectively. *mCherry* was amplified from MTLS#4218 (Thanbichler et al., 2007) and a linker was introduced using oligomers JSG_130 and JSG_131. All products were assembled into a plasmid via Gibson assembly. Proper plasmid assembly was verified by sequencing junctions. Plasmid was transformed into S17-1 and introduced into CB15N by conjugation with selection for kanamycin and nalidixic acid resistance. Second homologous recombination was achieved by counterselection on 0.3 % xylose.
CJW7535	CB15N *rpoC*::*mCherry-rpoC dnaA*::Ω xylX::pGM2195	UV-inactivated ϕCr30 phage lysate was prepared from GM2471. First, pGM2195 was transduced into CJW7531, followed by a second transduction of Ω into the resulting strain to disrupt the endogenous *dnaA* gene.
CJW7563	MG1655 *lacY(A177C) araFGH*::*spec ΔlacI ΔaraE araBAD*::*dCas9 galM<PBBa-J23119-sgRNA(ftsZ)-(S. pyogenes terminator)-(rrnB terminator)>gmpA rpoC*::*rpoC-ygfp-kan*	*rpoC*::*rpoC-ygfp-kan* from RLG7470 was moved into SJ_XTL229 by P1 transduction.
CJW7564	MG1655 *lacY(A177C) araFGH*::*spec ΔlacI ΔaraE araBAD*::*dCas9 galM<PBBa-J23119-sgRNA(ftsZ)-(S. pyogenes terminator)-(rrnB terminator)>gmpA rpsB*::*rpsB-msfgfp-kan*	*rpsB*::*rpsB-msfgfp-kan* from CJW7019 was moved into SJ_XTL229 by P1 transduction.
CJW7569	CB15N *rpoC*::*mCherry-rpoC ftsZ*::pBGentpXyl-ftsZ	UV-inactivated ϕCr30 phage lysate was prepared from CJW2591 and transduced into CJW7531.

CJW7576	MG1655 *lacY(A177C) araFGH*::*spec ΔlacI ΔaraE araBAD*::*dCas9 galM<PBBa-J23119-sgRNA(ftsZ)-(S. pyogenes terminator)-(rrnB terminator)>gmpA hupA*::*hupA-mCherry-kan*	*hupA*::*hupA-mCherry-kan* from CJW5556 (Paintdakhi et al., 2016) was moved into SJ_XTL229 by P1 transduction.
GM2471	CB15N *dnaA*::Ω xylX::pGM2195	(Gorbatyuk and Marczynski, 2001)
LS107	CB15N Δ*bla6*	(West et al., 2002)
MG1655	*F- lambda- ilvG- rfb-50 rph-1*	(Guyer et al., 1981)
MT190	CB15N *parB*::*ecfp-parB*	(Thanbichler and Shapiro, 2006)
RLG7470	*rpoC*::*rpoC-ygfp-kan*	(Bakshi et al., 2012)
SJ_XTL229	*lacY(A177C) araFGH*::*spec ΔlacI ΔaraE araBAD*::*dCas9 galM<PBBa-J23119-sgRNA(ftsZ)-(S. pyogenes terminator)-(rrnB terminator)>gmpA*	(Li et al., 2016)
SJ_XTL676	*lacY(A177C) araFGH*::*spec ΔlacI ΔaraE araBAD*::*dCas9 galM<PBBa-J23119-sgRNA(oriC)-(S. pyogenes terminator)-(rrnB terminator)>gmpA*	(Si et al., 2017)
YB1585	CB15N *ftsZ*::pBGST18-pXyl-ftsZ	(Wang et al., 2001)

Table 4. Oligonucleotides used in this study.

Name	Sequence
AP0039	ACCCAACTTAATCGCTGTAGGCTGGAGCTGCTTCG
AP0040	ATTAATTGCGTTGCGCAGTTCCCTACTCTCGCATGGG
AP0041	GAGAGTAGGGAACTGCGCAACGCAATTAATGTGAGTTAGC
AP0042	CAGCTCCAGCCTACAGCGATTAAGTTGGGTAACGCCA
AP0078	ATCAAACATCCTGCCAACTCCATGTGACAAACCGTCATCTTCGGCTACTTGCAACGCAATTAATGTGAGTTAGC
AP0079	ACAAACATTAATAACGAAGAGATGACAGAAAAATTTTCATTCTGTGACAGCCCTGATTCCGTGAGGATGC
JSG_018	GCCCGAGGGCACGTGACGCGTCTCCGGATG
JSG_019	ACCTCGGCGATCGCGAACGCCGAAGCTAGCGAATTCGTGGATC
JSG_020	GAATTCGCTAGCTTCGGCGTTCGCGATCGCCGAGGTG

JSG_021	GGCATGGACGAGCTGTACAAGTAAGCCACCCAAGTTTTAGTAAGCG
JSG_022	CGCTTTACTGGGTACGCTTACTAAAACTTGGGTGGCTTACTTGTACAGCTCGTCCATGCC
JSG_023	AACGTTACGCGTCACCGGTCGGCCACCATGGTGAGCAAGGGCGAG
JSG_024	GGCCGACCGGTGACGCGTAACGTTCGAATTGGCGCCGATCGAGCTGATG
JSG_025	CGGAGACGCGTCACGTGCCCTCGGGCACCGGCC
JSG_128	TCCGTAATACGACTCACTTAAGGCCTTGACGATGGTCAAGGTCTTCGTGG
JSG_129	GCCATGTTATCCTCCTCGCCCTTGCTCACCATCTTGGTTCCTTCTGCGGG
JSG_130	TTTTCGCGGGAAACCCCGCAGAAGGAACCAAGATGGTGAGCAAGGGCGAG
JSG_131	TTCAGGACTTCCTGGTTCATGCTGCCGCTGCCGCTGCCCTTGTACAGCTCGTCCATGC
JSG_132	AGCTGTACAAGGGCAGCGGCAGCGGCAGCATGAACCAGGAAGTCCTGAAC
JSG_133	ATGTACAGGCATGCGTCGACCCTCTAAGCATCCGCTTTTCGTTG
JSG_134	CGCAACGAAAAGCGGATGCTTAGAGGGTCGACGCATGC
JSG_135	CACGAAGACCTTGACCATCGTCAAGGCCTTAAGTGAGTCG
JSG_136	TTATCCGTACTCCTGATGATGC
JSG_137	GGGATCGCAGTGGTGAGTAAC
JSG_148	GCCTGGCAGAACTGCTGAACGCAGGTCTGGGCGGTTCTGATAACGAGTAATCGGCTGGCTCCGCTGCT
JSG_149	CATAAAAAAACCCGCCGAAGCGGGTTTTTACGTTATTTGCGGATTAACGAGGATCCCATATGAATATCCTCCTT
JSG_157	GTTCTCAGGATCTGGCTTCCCAGGCGGAAGAAAGCTTCGTAGAAGCTGAGTCGGCTGGCTCCGCTGCT
JSG_158	TTGCCGCCTTTCTGCAACTCGAACTATTTTGGGGGAGTTATCAAGCCTTAGGATCCCATATGAATATCCTCCTT
JSG_173	AAAAAAGCAAAAGGGCCGCAGATGCGACCCTTGTGTATCAAACAAGACGAGTGTAGGCTGGAGCTGCTTC
JSG_174	CAACAGAACATATTGACTATCCGGTATTACCCGGCATGACAGGAGTAAAATGTACAAGAAAGCTGGGTACG
NT157	TATGGATCCTGTTTTTCACCACGCCAATTTCATGG
NT158	TATGGTACCGAGGTTGAAAAGCGTGGTG

1630

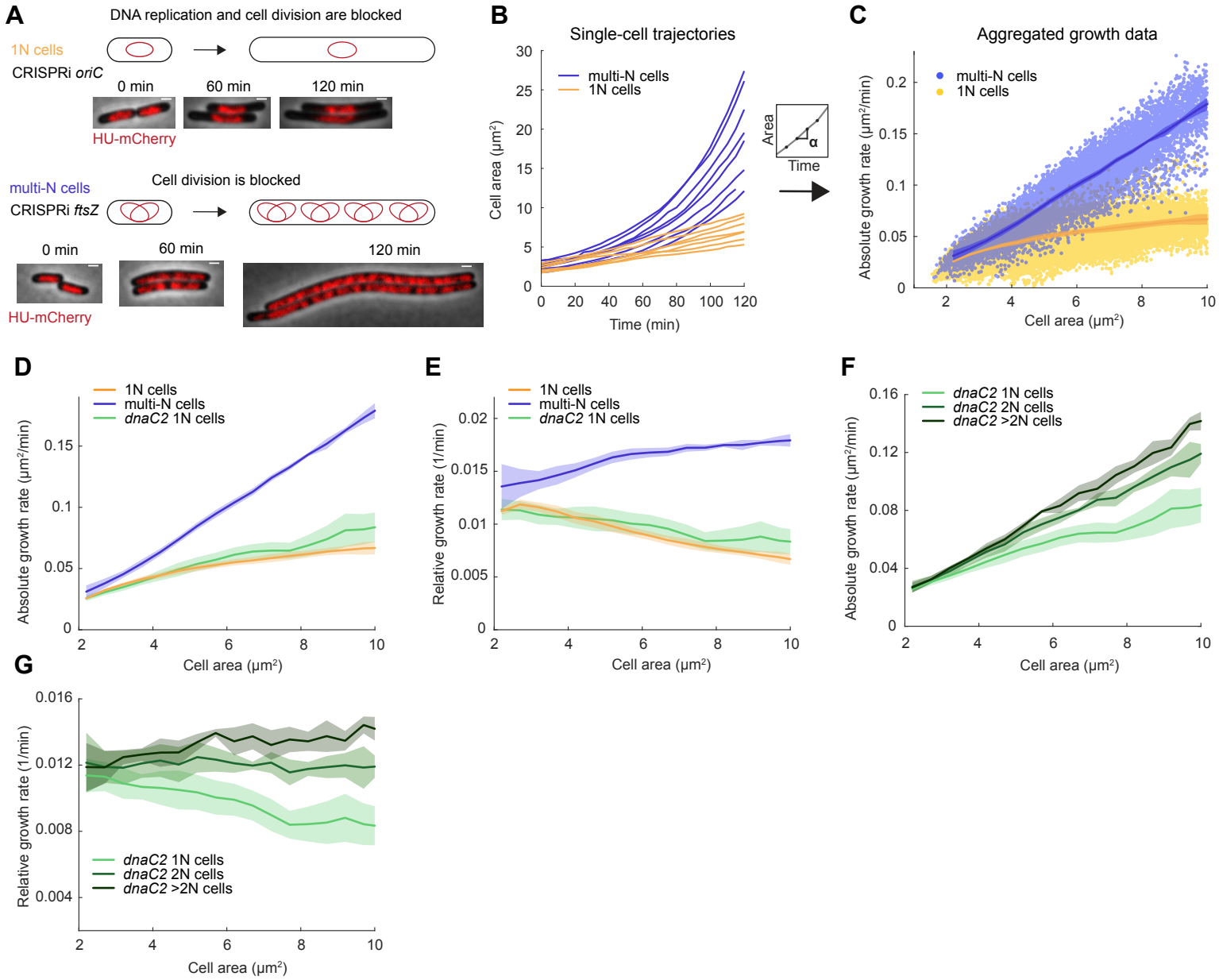
A
DNA replication and cell division are blocked
1N cells
CRISPRi oriC
0 min
60 min
120 min
HU-mCherry
multi-N cells
Cell division is blocked
CRISPRi ftsZ
0 min
60 min
120 min
HU-mCherry
B
Single-cell trajectories
multi-N cells
1N cells
Cell area (μm²)
Time (min)
Area
Time
α
C
Aggregated growth data
multi-N cells
1N cells
Absolute growth rate (μm²/min)
Cell area (μm²)
D
1N cells
multi-N cells
dnaC2 1N cells
Absolute growth rate (μm²/min)
Cell area (μm²)
E
1N cells
multi-N cells
dnaC2 1N cells
Relative growth rate (1/min)
Cell area (μm²)
F
dnaC2 1N cells
dnaC2 2N cells
dnaC2 >2N cells
Absolute growth rate (μm²/min)
Cell area (μm²)
G
dnaC2 1N cells
dnaC2 2N cells
dnaC2 >2N cells
Relative growth rate (1/min)
Cell area (μm²)

Figure 1

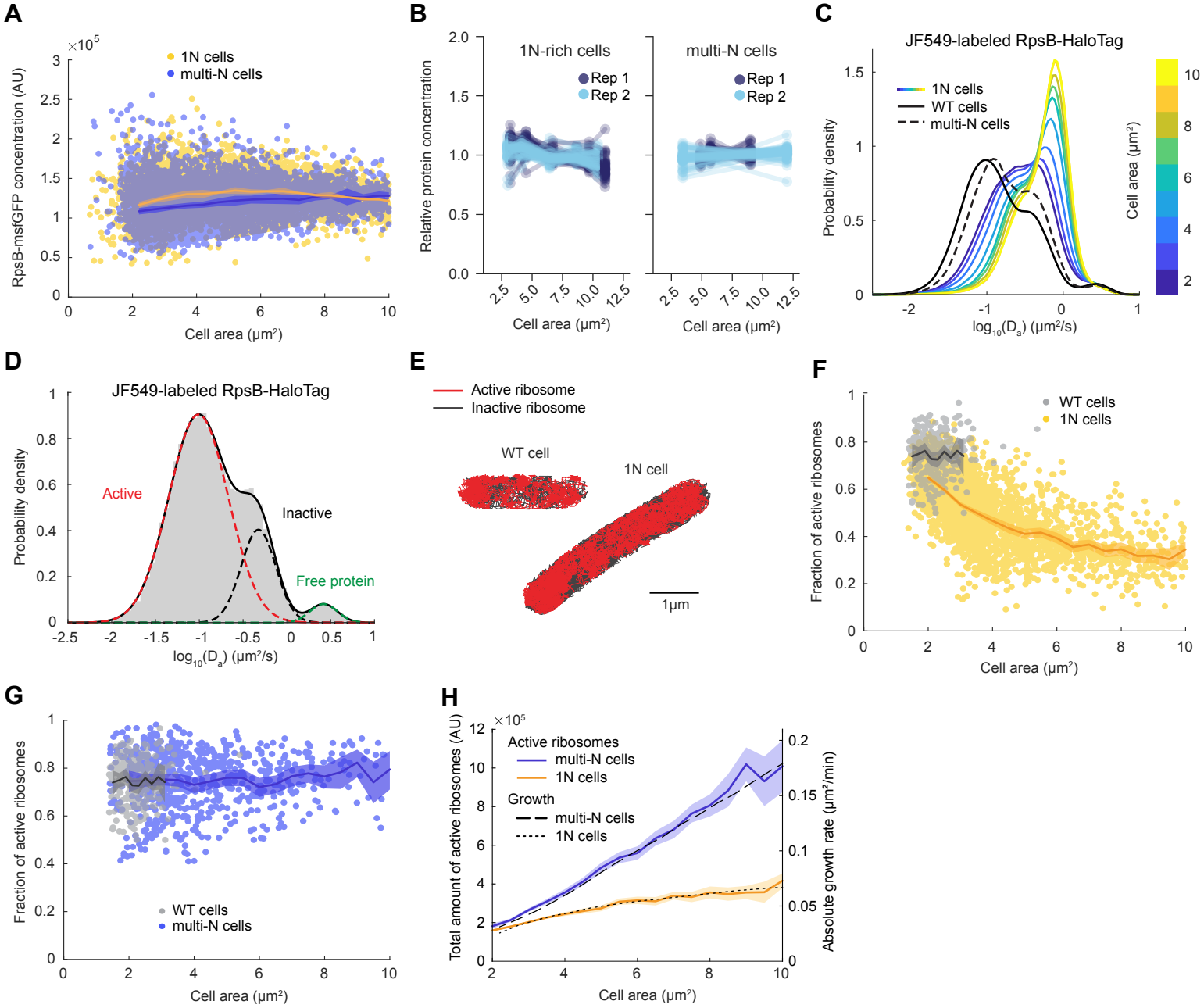
A
×10^5
1N cells
multi-N cells
RpsB-msfGFP concentration (AU)
Cell area (μm²)
B
1N-rich cells
multi-N cells
Rep 1
Rep 2
Relative protein concentration
Cell area (μm²)
C
JF549-labeled RpsB-HaloTag
1N cells
WT cells
multi-N cells
Probability density
log10(Da) (μm²/s)
Cell area (μm²)
D
JF549-labeled RpsB-HaloTag
Active
Inactive
Free protein
Probability density
log10(Da) (μm²/s)
E
Active ribosome
Inactive ribosome
WT cell
1N cell
1μm
F
WT cells
1N cells
Fraction of active ribosomes
Cell area (μm²)
G
WT cells
multi-N cells
Fraction of active ribosomes
Cell area (μm²)
H
×10^5
Active ribosomes
multi-N cells
1N cells
Growth
multi-N cells
1N cells
Total amount of active ribosomes (AU)
Absolute growth rate (μm²/min)
Cell area (μm²)

Figure 2

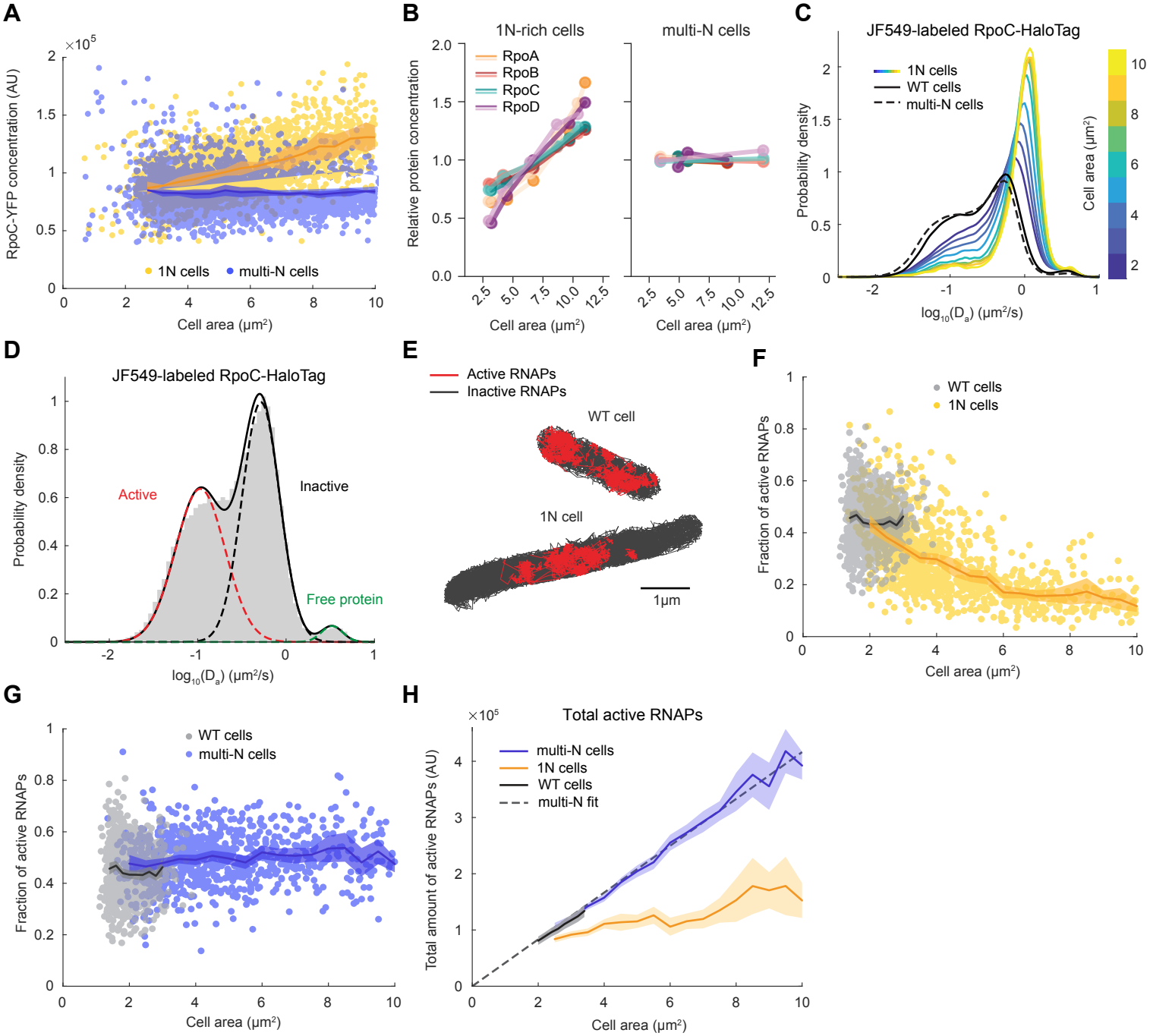
A
RpoC-YFP concentration (AU)
×10^5
1N cells
multi-N cells
Cell area (μm²)
B
1N-rich cells
multi-N cells
RpoA
RpoB
RpoC
RpoD
Relative protein concentration
Cell area (μm²)
C
JF549-labeled RpoC-HaloTag
1N cells
WT cells
multi-N cells
Probability density
Cell area (μm²)
log10(Da) (μm²/s)
D
JF549-labeled RpoC-HaloTag
Active
Inactive
Free protein
Probability density
log10(Da) (μm²/s)
E
Active RNAPs
Inactive RNAPs
WT cell
1N cell
1μm
F
WT cells
1N cells
Fraction of active RNAPs
Cell area (μm²)
G
WT cells
multi-N cells
Fraction of active RNAPs
Cell area (μm²)
H
Total active RNAPs
×10^5
multi-N cells
1N cells
WT cells
multi-N fit
Total amount of active RNAPs (AU)
Cell area (μm²)

Figure 3

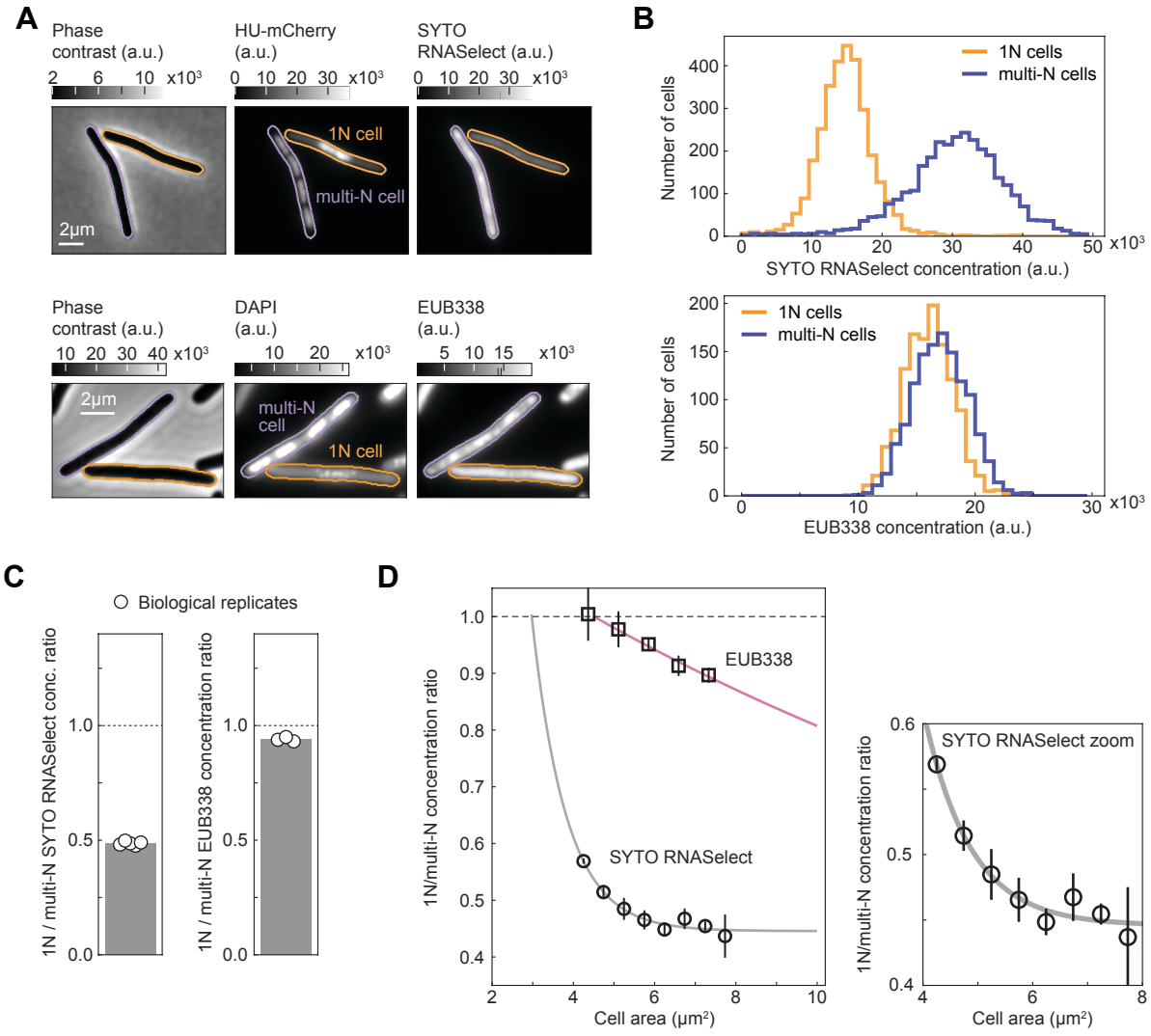
A
Phase contrast (a.u.)
2 6 10 x10³
HU-mCherry (a.u.)
0 10 20 30 x10³
SYTO RNASelect (a.u.)
0 10 20 30 x10³
1N cell
multi-N cell
2µm
Phase contrast (a.u.)
10 20 30 40 x10³
DAPI (a.u.)
10 20 x10³
EUB338 (a.u.)
5 10 15 x10³
2µm
multi-N cell
1N cell
B
1N cells
multi-N cells
Number of cells
SYTO RNASelect concentration (a.u.)
EUB338 concentration (a.u.)
C
Biological replicates
1N / multi-N SYTO RNASelect conc. ratio
1N / multi-N EUB338 concentration ratio
D
EUB338
SYTO RNASelect
1N/multi-N concentration ratio
Cell area (µm²)
SYTO RNASelect zoom

Figure 4

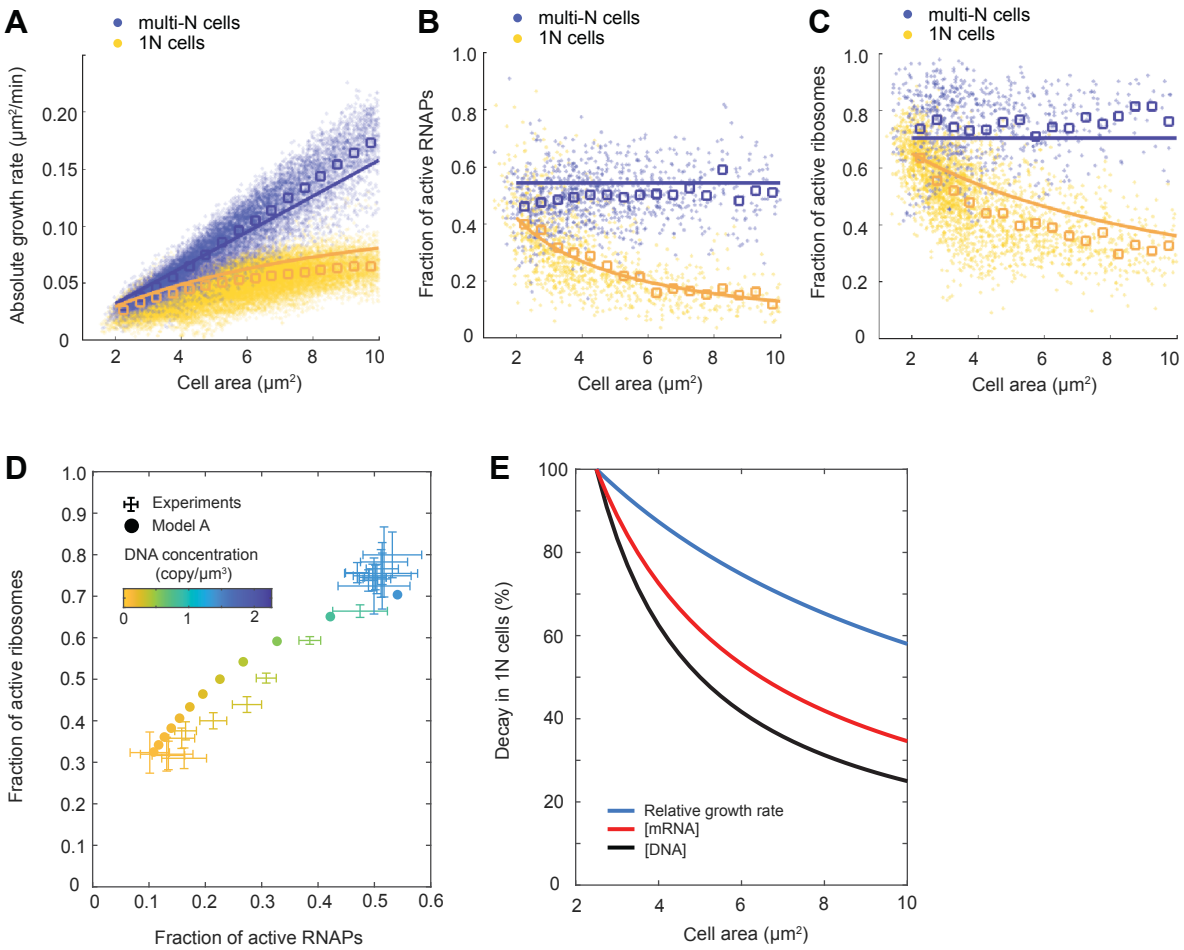
A
multi-N cells
1N cells
Absolute growth rate (μm²/min)
Cell area (μm²)
B
multi-N cells
1N cells
Fraction of active RNAPs
Cell area (μm²)
C
multi-N cells
1N cells
Fraction of active ribosomes
Cell area (μm²)
D
Experiments
Model A
DNA concentration (copy/μm³)
Fraction of active ribosomes
Fraction of active RNAPs
E
Decay in 1N cells (%)
Relative growth rate
[mRNA]
[DNA]
Cell area (μm²)

Figure 5

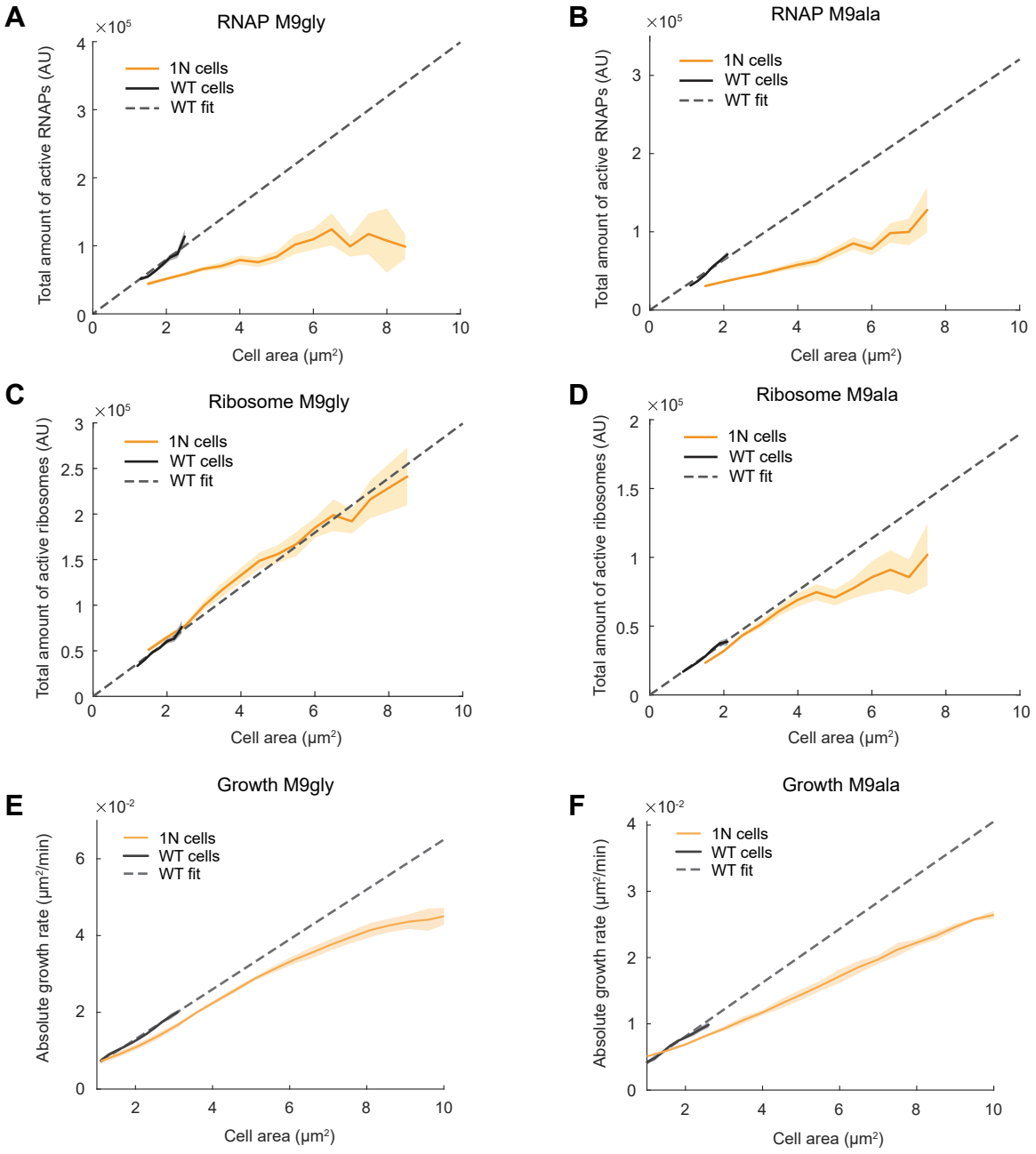
A
RNAP M9gly
×10^5
Total amount of active RNAPs (AU)
1N cells
WT cells
WT fit
Cell area (μm²)
B
RNAP M9ala
×10^5
Total amount of active RNAPs (AU)
1N cells
WT cells
WT fit
Cell area (μm²)
C
Ribosome M9gly
×10^5
Total amount of active ribosomes (AU)
1N cells
WT cells
WT fit
Cell area (μm²)
D
Ribosome M9ala
×10^5
Total amount of active ribosomes (AU)
1N cells
WT cells
WT fit
Cell area (μm²)
E
Growth M9gly
×10^-2
Absolute growth rate (μm²/min)
1N cells
WT cells
WT fit
Cell area (μm²)
F
Growth M9ala
×10^-2
Absolute growth rate (μm²/min)
1N cells
WT cells
WT fit
Cell area (μm²)

Figure 6

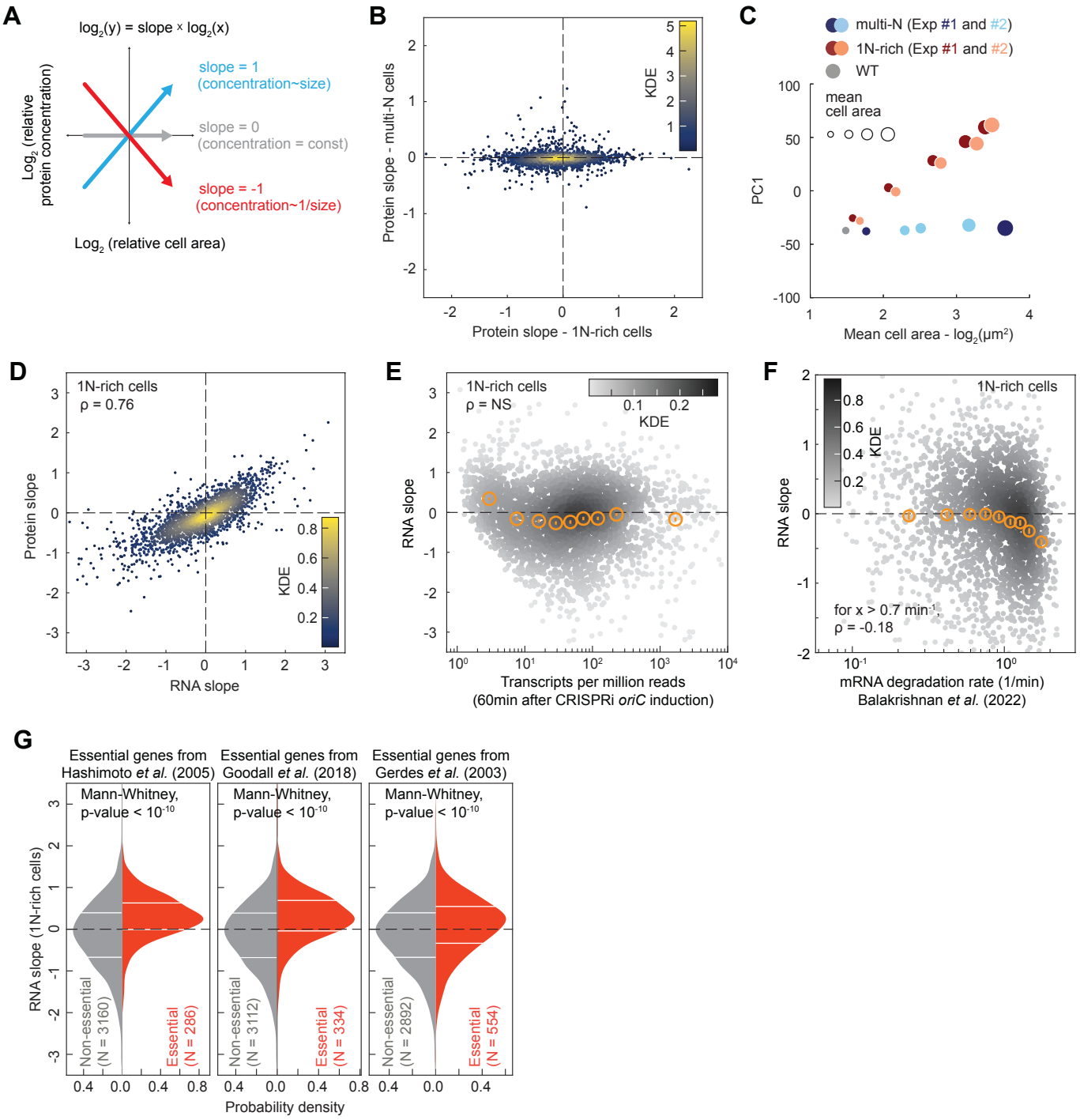
A
log2(y) = slope × log2(x)
slope = 1
(concentration~size)
slope = 0
(concentration = const)
slope = -1
(concentration~1/size)
Log2 (relative protein concentration)
Log2 (relative cell area)
B
Protein slope - multi-N cells
Protein slope - 1N-rich cells
KDE
C
multi-N (Exp #1 and #2)
1N-rich (Exp #1 and #2)
WT
mean cell area
PC1
Mean cell area - log2(μm²)
D
1N-rich cells
ρ = 0.76
Protein slope
RNA slope
KDE
E
1N-rich cells
ρ = NS
KDE
RNA slope
Transcripts per million reads
(60min after CRISPRi oriC induction)
F
1N-rich cells
KDE
RNA slope
for x > 0.7 min-1
ρ = -0.18
mRNA degradation rate (1/min)
Balakrishnan et al. (2022)
G
Essential genes from Hashimoto et al. (2005)
Essential genes from Goodall et al. (2018)
Essential genes from Gerdes et al. (2003)
Mann-Whitney, p-value < 10-10
RNA slope (1N-rich cells)
Non-essential (N = 3160)
Essential (N = 286)
Non-essential (N = 3112)
Essential (N = 334)
Non-essential (N = 2892)
Essential (N = 554)
Probability density

Figure 7

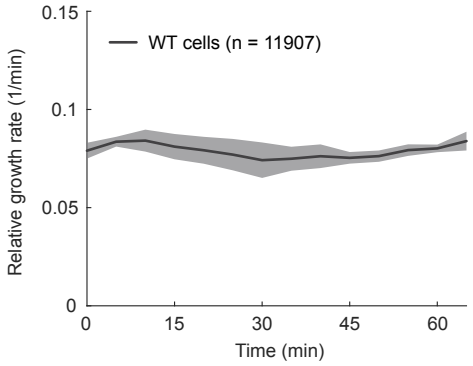

Figure 1 Figure supplement 1

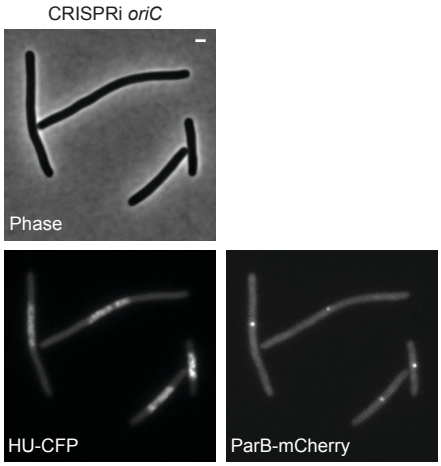

Figure 1 Figure supplement 2

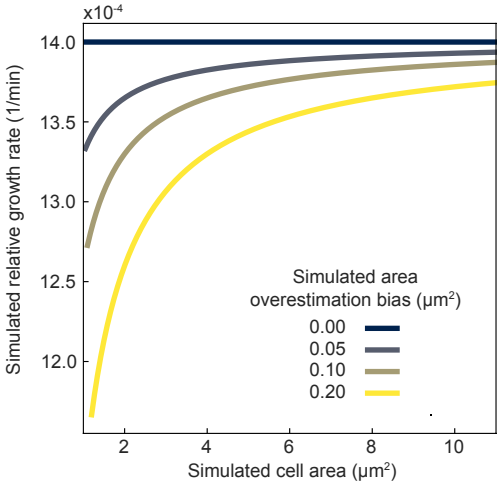

Figure 1 Figure supplement 3

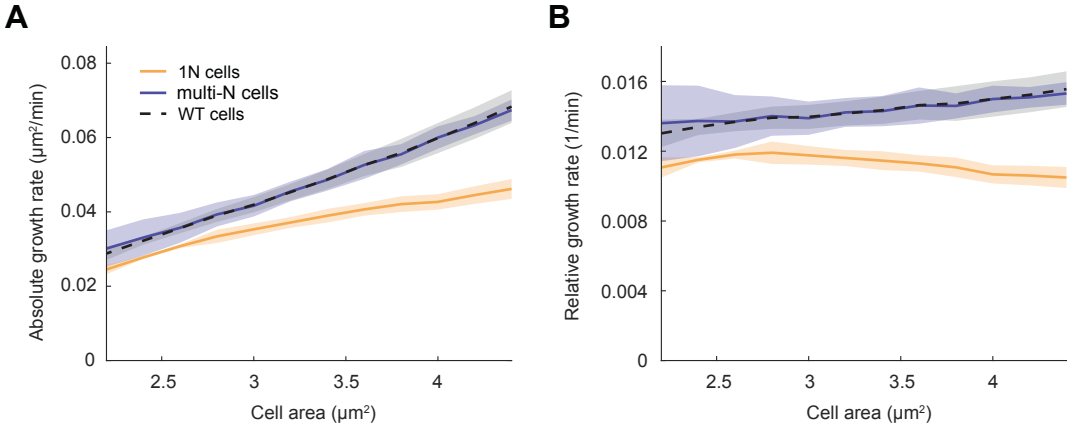

Figure 1 Figure supplement 4

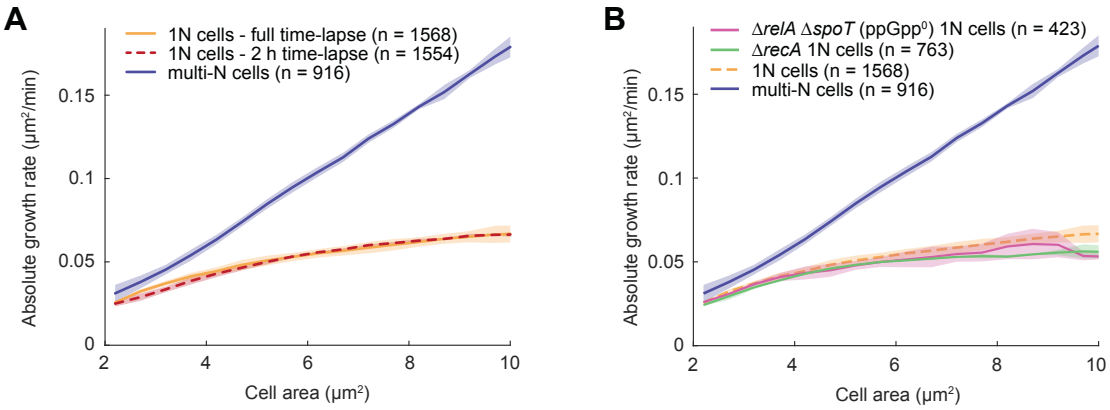

Figure 1 Figure supplement 5

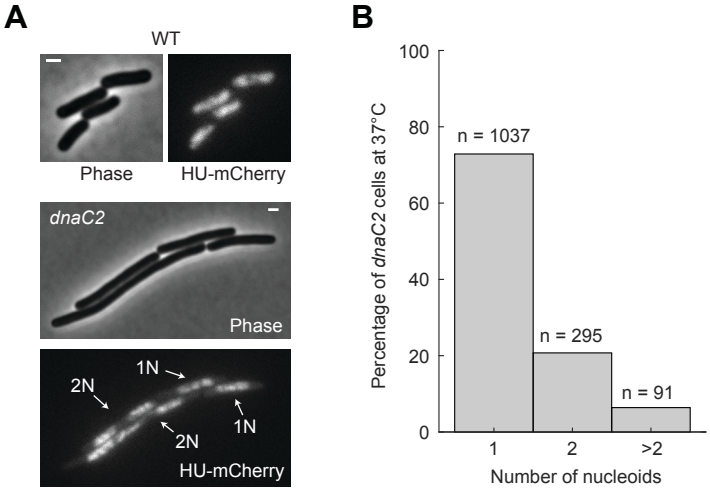

Figure 1 Figure supplement 6

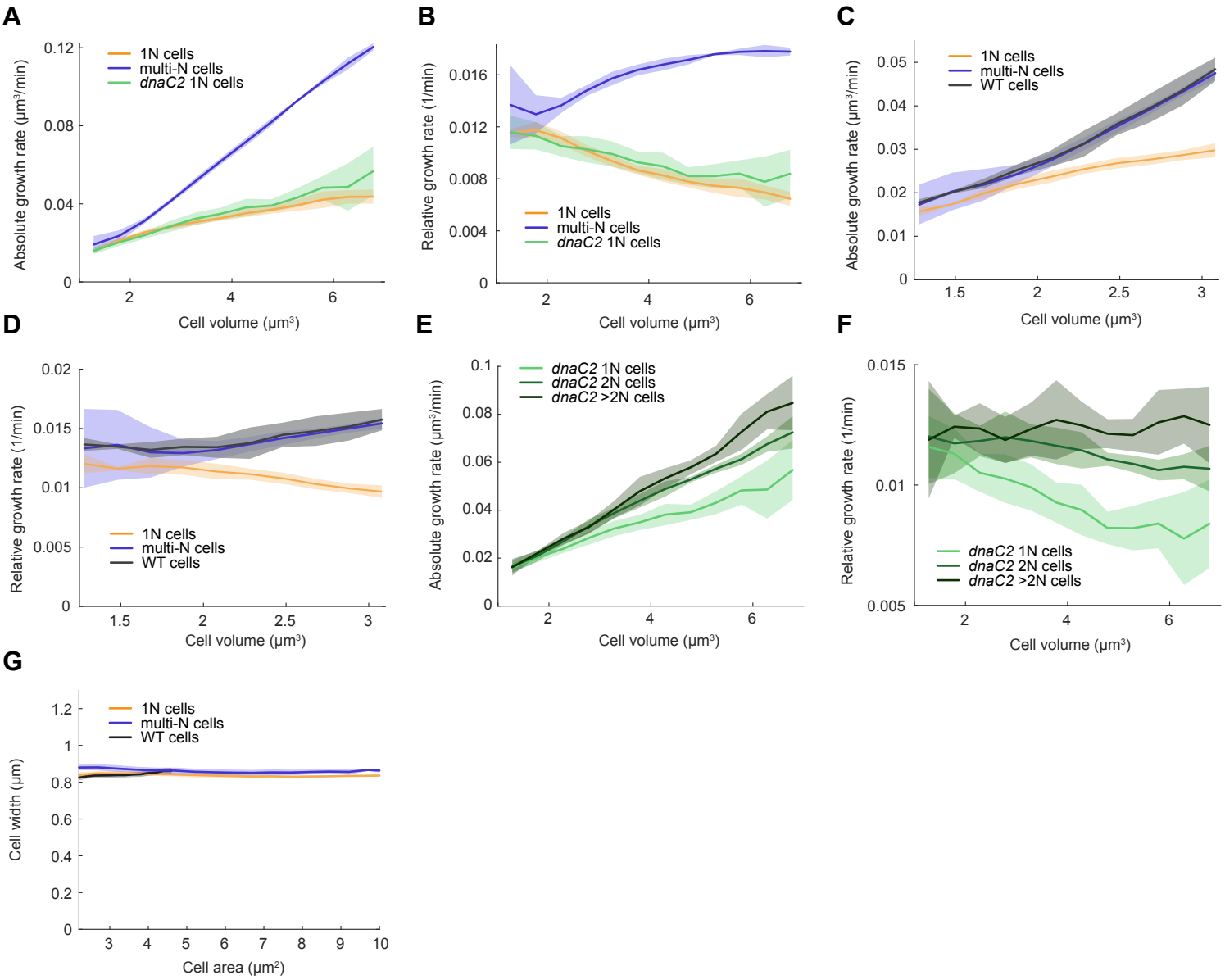

Figure 1 Figure supplement 7

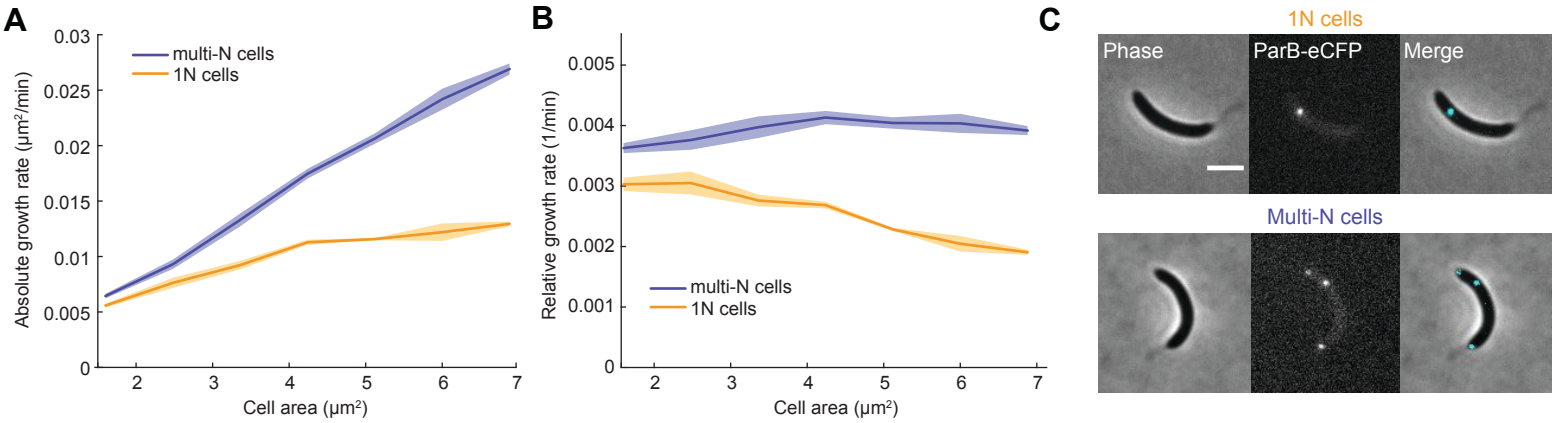

Figure 1 Figure supplement 8

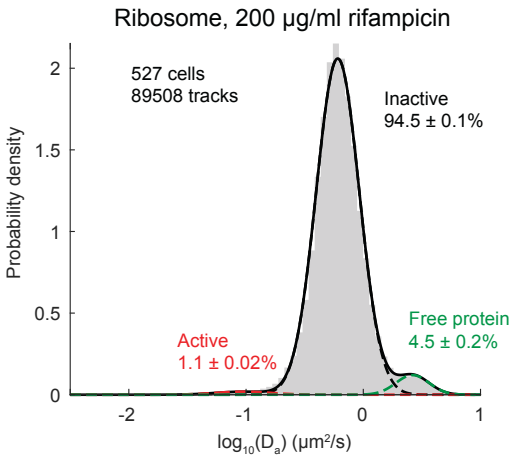

Figure 2 Figure supplement 1

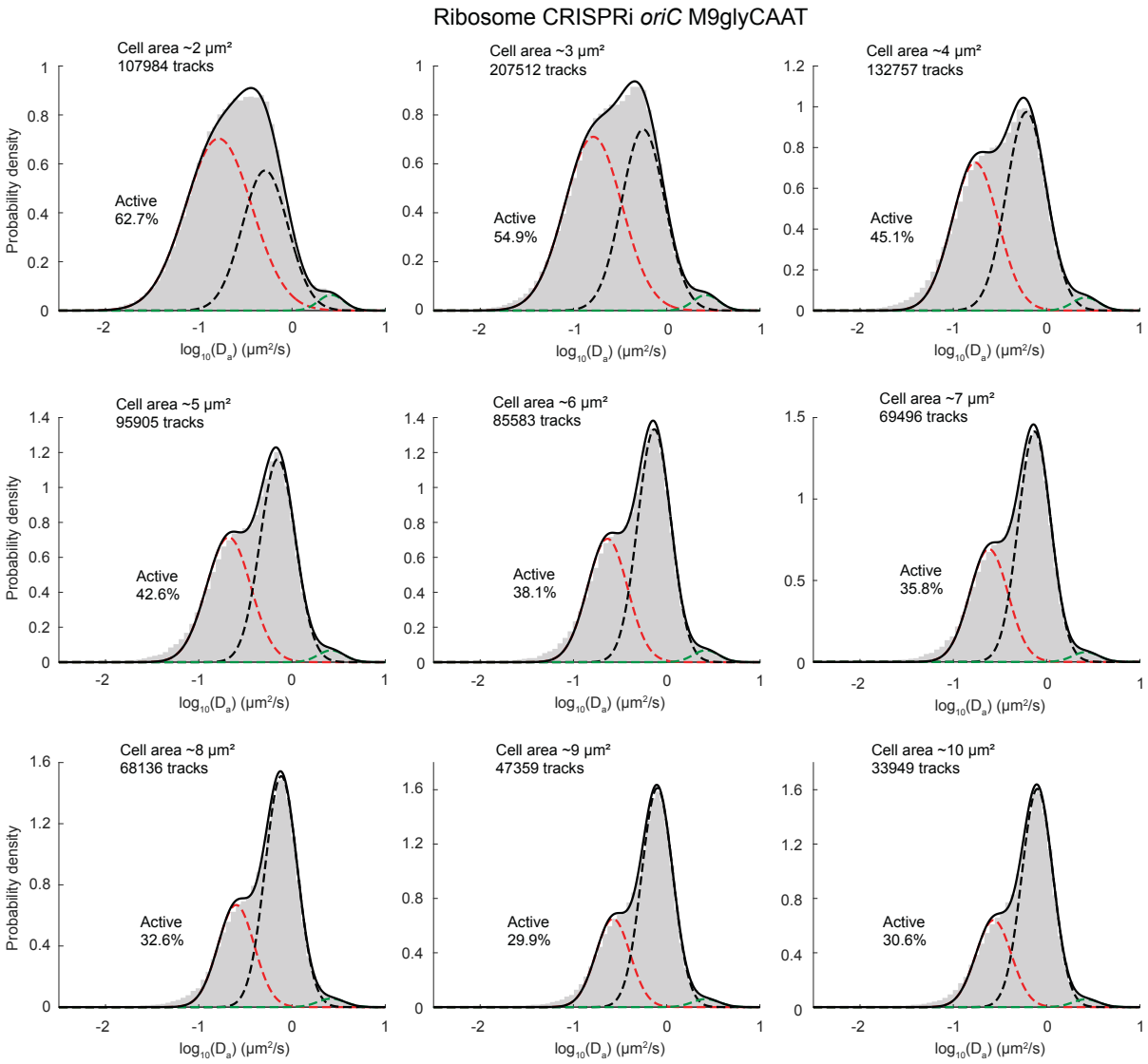

Figure 2 Figure supplement 2

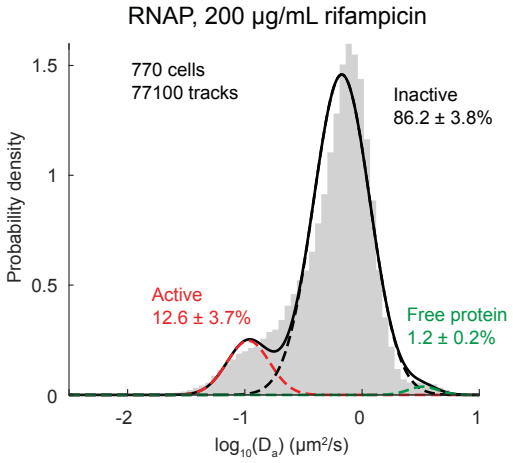

Figure 3 Figure supplement 1

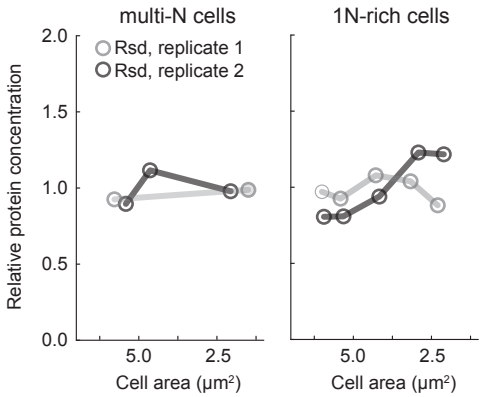

Figure 3 Figure supplement 2

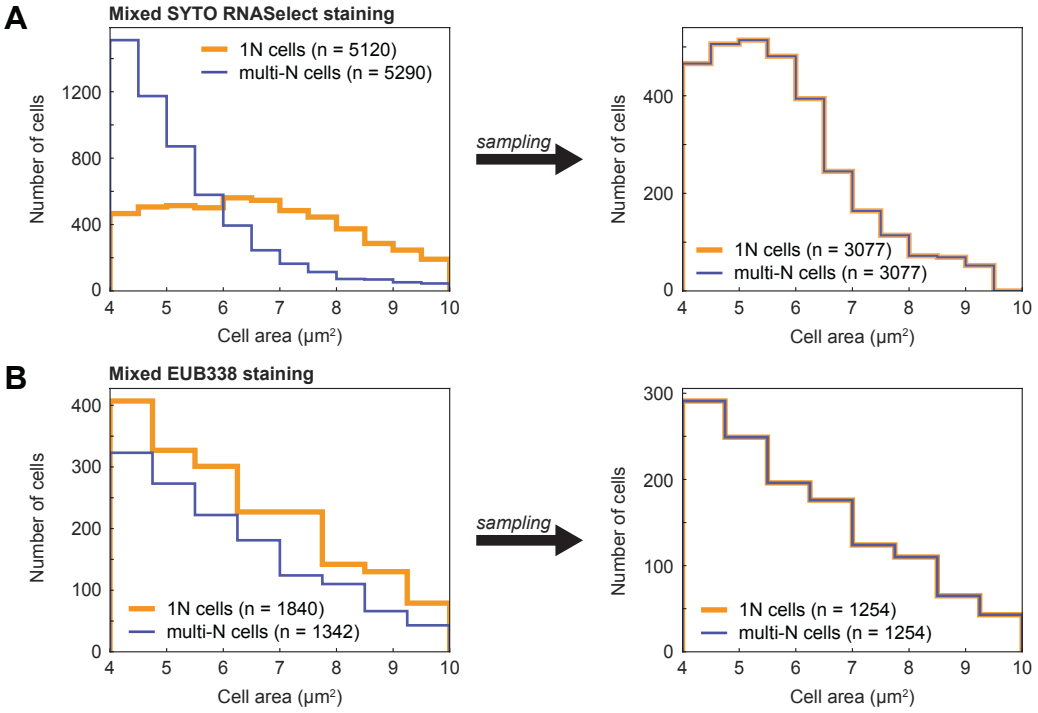

Figure 4 Figure supplement 1

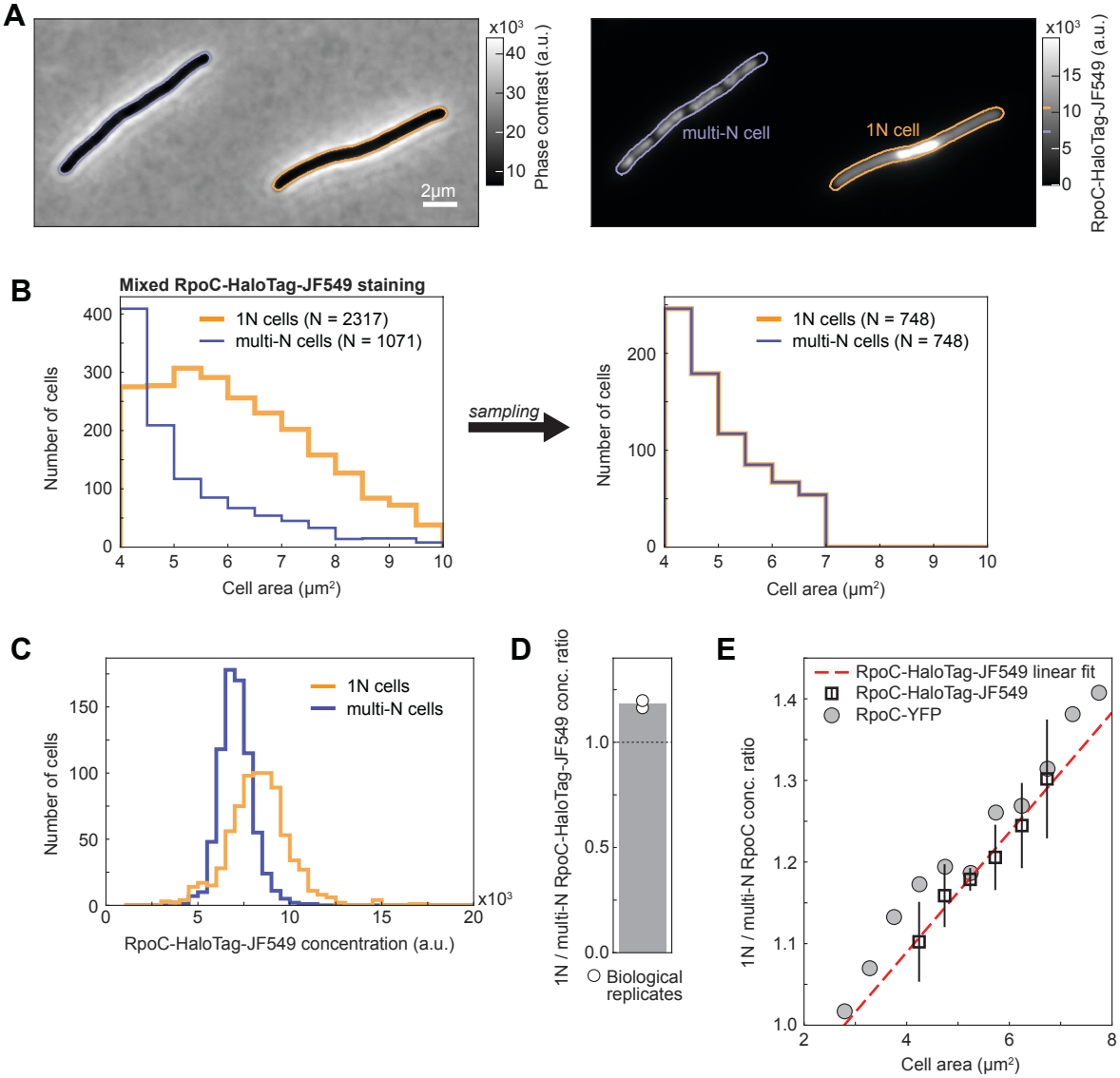

Figure 4 Figure supplement 2

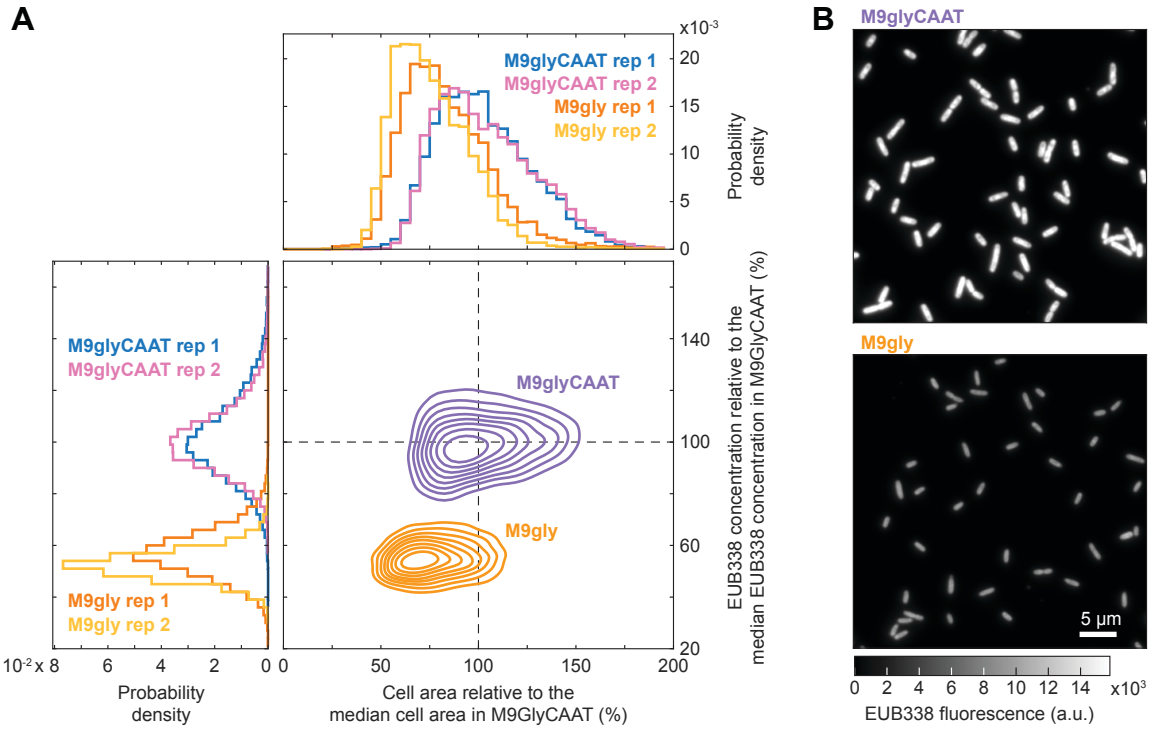

Figure 4 Figure supplement 3

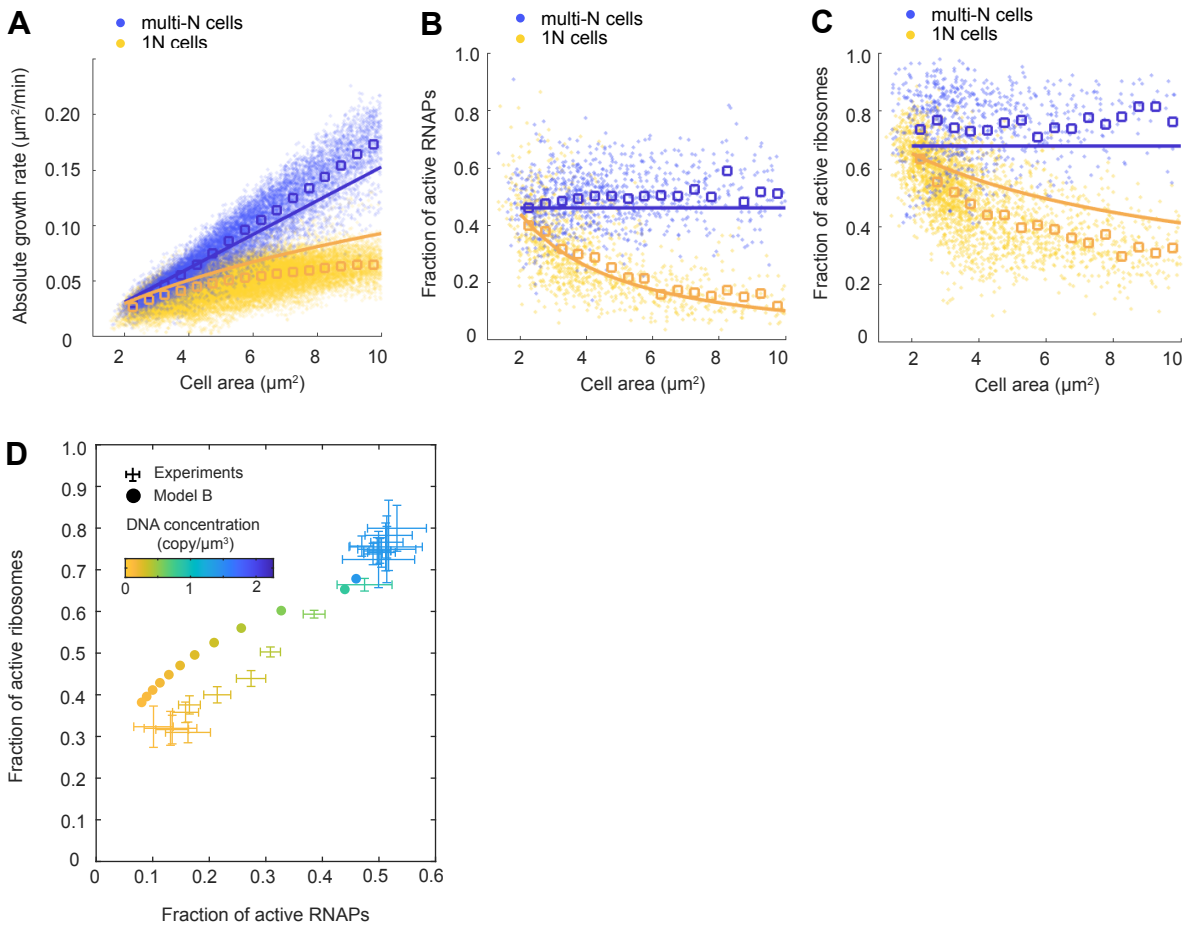

Figure 5 Figure supplement 1

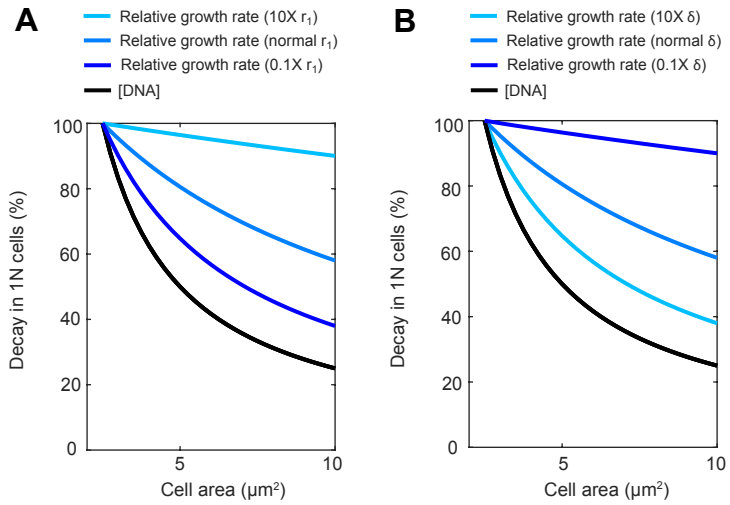

Figure 5 Figure supplement 2

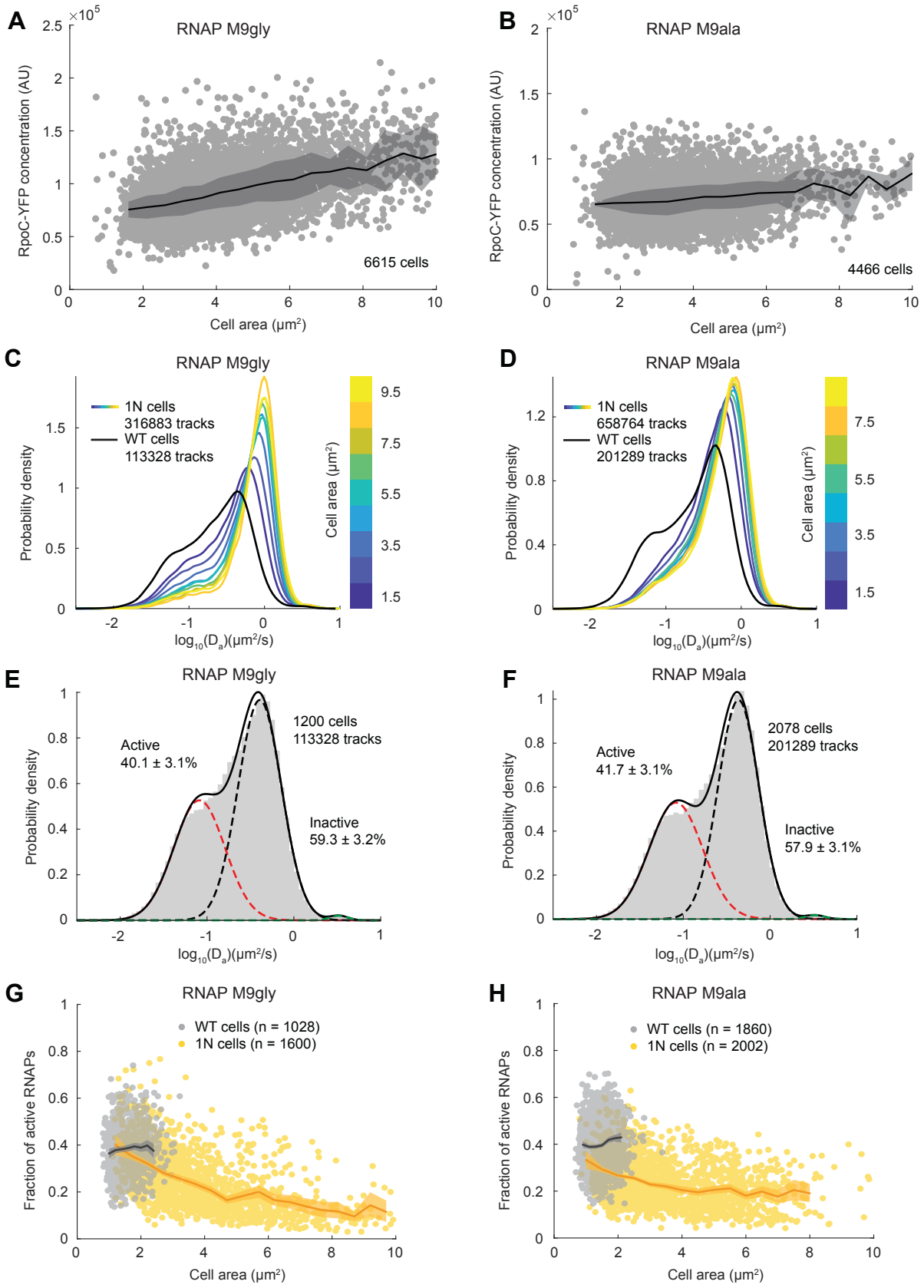

Figure 6 Figure supplement 1

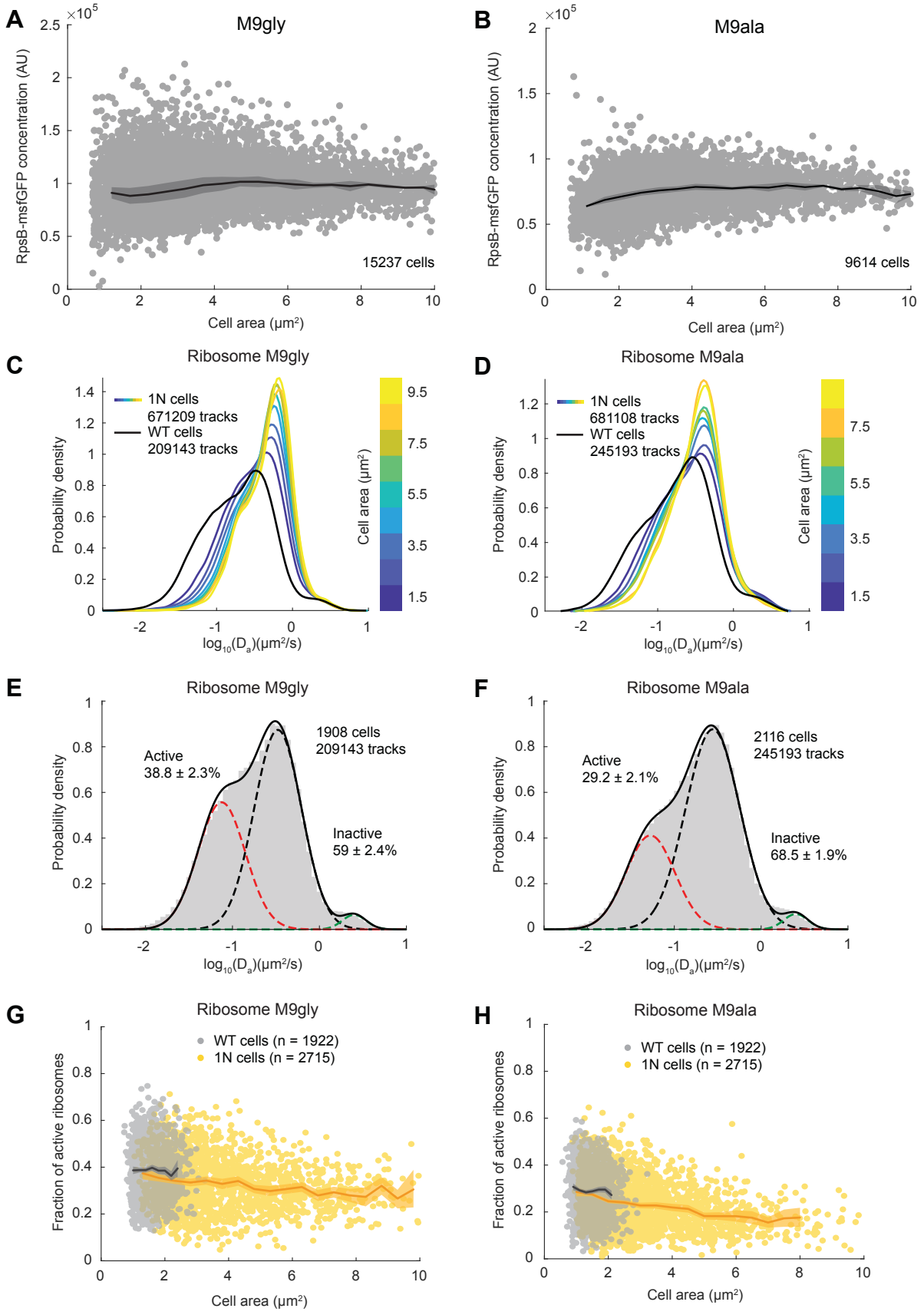

Figure 6 Figure supplement 2

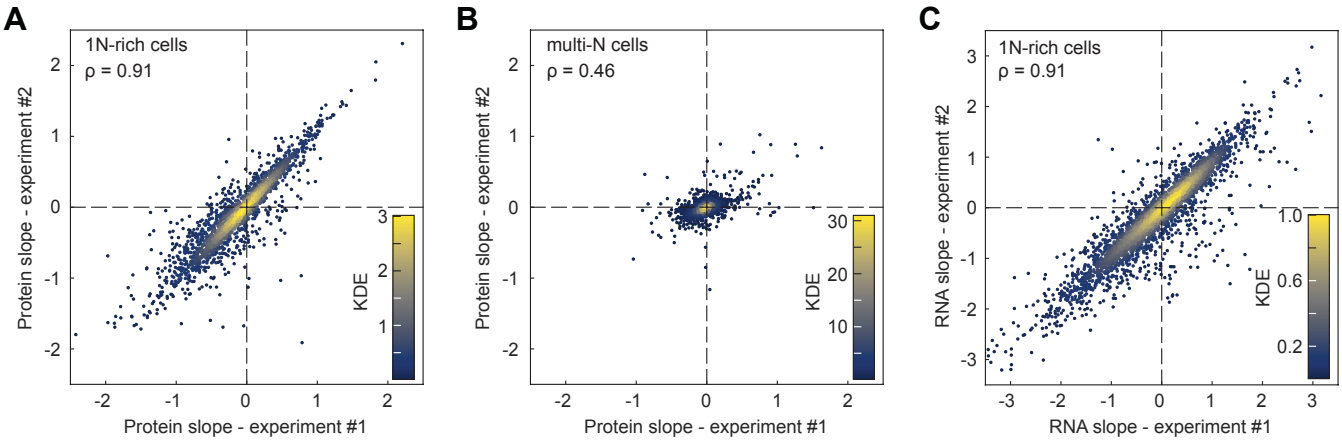

Figure 7 Figure supplement 1

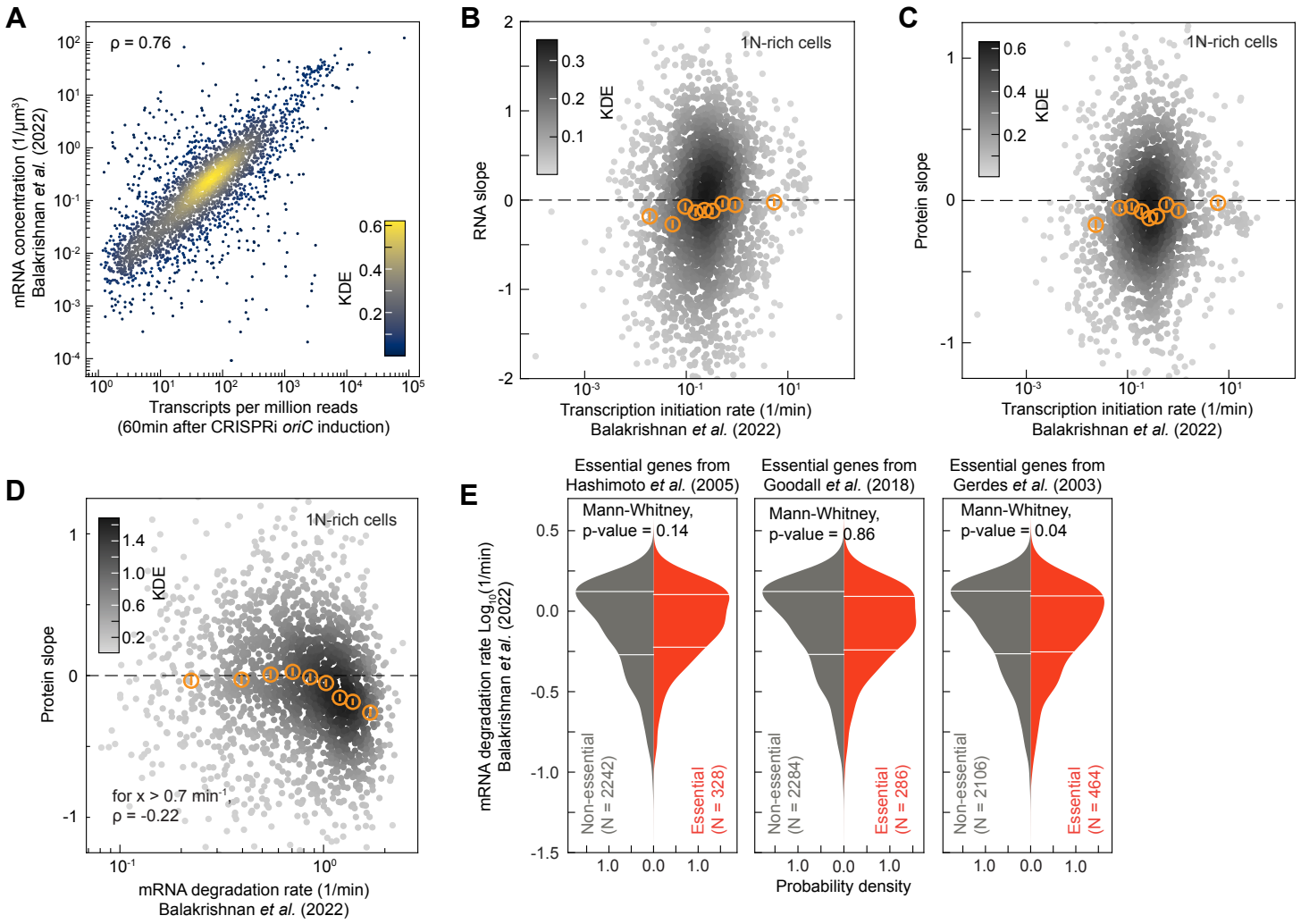

Figure 7 Figure supplement 2

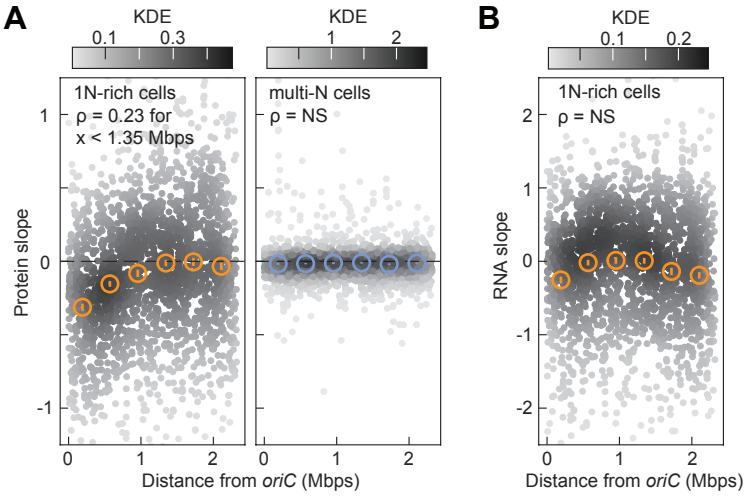

Figure 7 Figure supplement 3

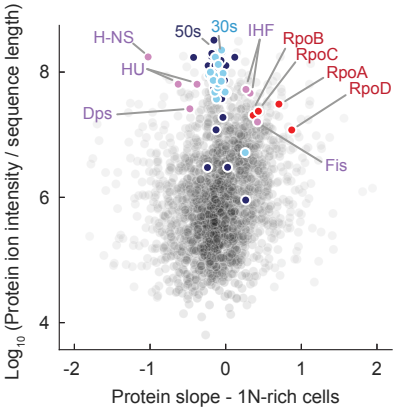

Figure 7 Figure supplement 4